Spatial organization of sensorimotor representations in cerebellar molecular layer interneurons

Maria-Miruna Costreie

Sorbonne Université

Ecole doctorale : Brain, Cognition and Behaviour

Laboratoire : Gene, Synapses and Cognition, CNRS UMR-3571

Equipe : Synapse and Circuit Dynamics, Institut Pasteur

Spatial organization of sensorimotor representations in cerebellar molecular layer interneurons

Maria-Miruna COSTREIE

Thèse de doctorat de Neurosciences

Dirigée par David DIGREGORIO

Présentée et soutenue publiquement le 05 December 2023

Devant un jury composé de :

Dr. Philippe ISOPE (INCI, Université de Strasbourg)	Rapporteur
Dr. Indira RAMAN (Northwestern University)	Rapporteuse
Dr. Fekrije SELIMI (CIRB, Collège de France)	Présidente du jury
Dr. Jason CHRISTIE (University of Colorado School of Medicine)	Examinateur
Dr. Michael GRAUPNER (Université Paris Cité)	Examinateur
Dr. David DIGREGORIO (Institut Pasteur)	Directeur de thèse

"What then is time? If no one asks me, I know what it is. If I wish to explain it to him who asks, I do not know."

- Saint Augustine, Book XI of the Confessions (397)

Acknowledgements

The thesis is the tangible result of the adventurous and complex journey called a PhD. Underneath the surface, this journey comprises of joy and sadness, laughter and anger, knowledge and confusion, but most importantly, amazing people that shape it and oneself throughout all the ups and downs.

I would like to thank my jury members: **Indira Raman, Philippe Isope, Fekrije Selimi, Michael Graupner** and **Jason Christie**, you have given me the honour of evaluating this thesis in which I put four years of work.

Importantly, I would like to thank everyone in the lab of Synapse and Circuit Dynamics for all your support, knowledge sharing and patience at the canteen: to **David** for welcoming me in this team and shaping the project to make the most out of this experience; to **Franziska** and **Zuzanna** for always taking the time to help or teach me the wonders of in vivo experiments; to **Gaël** and **Florian** for introducing me to the vast and amazing world of microscopy and optics; to **Maureen**, **Semih** and **Stefano** for adding so much laughter to the science; to **Giovanni** for making analysis fun (at least in a statistically significant amount of time); to **Alessandro** for being the greatest master of Dungeons and Dragons; à **Cécile** pour avoir fait disparaître tous mes problèmes de souris; to **Francisco** for making IGOR look simple and backing up my tea drinking.

To my PhD comrades **Camille, Maria** and **Enzo**, you have walked this journey with me, all the way and beyond. *Piplettes* was a truly amazing experience that would not have been so without you. Also thank you to the **Susanna, Nathalie** and **Deshmukh** for their support and troubles for making our student project alive and welcoming me in the PPU.

Mulțumesc **familiei mele** pentru că a creat mediul și inspirația care au făcut posibil acest final (...sau început) și pentru că acasă a fost mereu o oază în deșertul acestei experiențe. **Prietenilor mei**, Pic vă mulțumește pentru că ați fost mereu la cel puțin un telefon distanță și m-ați ajutat să presar cu momente frumoase toți acești ani, sunt cu adevărat norocoasă să vă am alături.

Also, a big thank you to **my Manchester family**, my PhD years also mark earning a second family that I am so glad to call as such.

And of course, I thank you **Michael**. I would like to leave aside any grand words of gratitude and simply thank you for your presence, a true presence in my life and throughout it all from before its start and beyond the end of the years marking my PhD thesis work.

Abstract

Fine-tuning of temporally precise behaviours by the cerebellum requires diverse cell types and specific connectivity to generate the neural activity underlying sensory-motor transformations. Molecular layer interneurons (MLIs) are well-positioned to influence cerebellar cortical output activity by Purkinje cells and gate synaptic plasticity underlying motor adaptation. However, how the diversity of MLI anatomy, intrinsic properties and connectivity influence cerebellar cortical circuit computations is not understood. We hypothesize that specific lamina-dependent properties of MLI circuits are a critical mechanism of functional MLI diversity. To address this question, we monitored MLI activity using high-speed two-photon calcium imaging in awake mice, in response to air stimuli of the face and whiskers. Brief puff stimuli to the face evoked Ca^{2+} responses in deep MLIs displayed gradually smaller amplitudes and on average 10 ms faster response onsets as compared with those in the outer molecular layer. We identified a transcriptional cluster of MLIs (*Penk1*) that marked putative basket cells to examine if MLI classes could account for laminar dependence of MLI responses. We did not observe a difference in activity response kinetics in Penk1+ MLIs. In contrast, we did observe a laminar difference of onset delays of granule cell axonal responses, suggesting an input-inherited spatial dependence of MLIs responses. In apparent contrast to previous studies, the peak amplitude of all MLI responses did not correlate with the peak whisker deflection angle. However, for a subset of MLIs in which their Ca^{2+} response onset occurred after the initiation of whisking, response amplitudes correlated with the whisker deflection. These slow-onset MLIs were located preferentially in the outer molecular layer. Longer stimulation induced prolonged Ca^{2+} activity in over half of the cells in the inner, middle and outer molecular layers, suggesting a robust somatosensory representation throughout the molecular layer. During spontaneous whisking, Ca^{2+} response amplitudes correlated with the whisker deflection angle, suggesting that somatosensory response occludes motor-related responses during air puff stimuli. Thus, our results are consistent with a layer-specific sensorimotor representation in MLIs that is, at least in part, dictated by the intrinsic GC input properties and/or a spatial segregation of whisk-related information across GC inputs.

Key words: cerebellum, interneurons, sensorimotor system, 2-photon imaging

Résumé

L’affinement par le cervelet des comportements temporellement précis nécessite divers types de cellules et une connectivité spécifique pour générer l'activité neuronale sous-jacente aux transformations sensori-motrices. Les interneurones de la couche moléculaire (MLI) sont bien positionnés pour influencer l'activité sortante du cortex cérébelleux par les cellules de Purkinje et réguler la plasticité synaptique sous-jacente à l'adaptation motrice. Cependant, la manière dont la diversité de l'anatomie, les propriétés intrinsèques et la connectivité des MLI influencent les calculs du circuit cortical cérébelleux n’a pas encore été élucidée. Nous émettons l'hypothèse que l’importance computationnelle de la diversité fonctionnelle des MLIs repose sur des propriétés propres aux différentes couches du cortex cérébelleux. Pour répondre à cette question, nous avons observé l'activité des MLI en utilisant l'imagerie calcique à deux photons à haute vitesse chez des souris éveillées, en réponse à des stimuli d'air sur le visage et les vibrisses. De brefs jets d’air au visage ont provoqué des réponses calciques dans les MLI profonds affichant des amplitudes progressivement plus petites et des phases d’amorce en moyenne 10 ms plus rapides par rapport à celles dans la couche moléculaire externe. Nous avons identifié un groupe transcriptionnel de MLI (Penk1) qui marquait des cellules panier potentielles afin de déterminer si les différences de classe de MLI pouvaient expliquer la dépendance laminaire des réponses. Nous n'avons pas observé de différence de cinétique de réponse particulière aux MLI Penk1+. En revanche, nous avons observé une différence laminaire dans les délais de phase d’amorce des réponses axonales des cellules granulaires, ce qui suggère que les différences laminaires des réponses des MLI sont héritées des différences laminaires des entrées aux MLI. Contrairement à des études antérieures, l'amplitude maximale de toutes les réponses des MLI n’était pas corrélée à l'angle de déviation maximale des vibrisses. Cependant, pour un sous-ensemble de MLI dont la phase d’amorce de la réponse calcique se produisit après le début du mouvement des vibrisses, les amplitudes de réponses étaient corrélées avec la déviation des vibrisses. Ces MLI à amorce lente étaient situées majoritairement dans la couche moléculaire externe. Une stimulation plus longue prolongea l’activité calcique dans plus de la moitié des cellules des couches moléculaires interne, moyenne et externe, suggérant une représentation robuste de l’activité somatosensorielle dans toute la couche moléculaire. Pendant les mouvements de vibrisses spontanés, l’amplitude des réponses calciques corrélaient avec l'angle de déviation des vibrisses, suggérant que la réponse somatosensorielle occulte les réponses liées au mouvement pendant les stimuli d'air. Ainsi, nos résultats sont cohérents avec un encodage sensorimoteur des MLI qui est spécifique à la couche moléculaire dans laquelle ils sont situés, et dictée d’entrée, au moins en partie, par les propriétés intrinsèques des cellules granulaires et/ou par une ségrégation spatiale des informations liées aux vibrisses à travers les cellules granulaires.

Mots clés: cervelet, interneurones, système sensorimoteur, imagerie à 2-photons

Table of Contents

List of abbreviations

AAV	Adeno-associated virus
AMPA	α-amino-3-hydroxy-5-methyl-4-isoxazolepropionic acid
AP	Action potential
BC	Basket cell
Ca^{2+}	Calcium ion
CC	Candelabrum cell
CF	Climbing fibre
CS	Conditioned stimulus
DCN	Deep cerebellar nuclei
EAAT4	Excitatory amino acid transporter 4
EPSC	Excitatory postsynaptic current
FFI	Feed-forward inhibition
FOV	Field of view
FWHM	Full width at half maximum
GABA	Gamma-aminobutyric acid
Gjd2	Gap Junction Protein Delta 2
GoC	Golgi cell
GC	Granule cell
IO	Inferior olive
ISH	*In situ* hybridization
IQR	Interquartile range
MF	Mossy fibre
MLI	Molecular layer interneuron
NMDA	N-methyl-D-aspartate
LTD	Long term depression
LTP	Long term potentiation
mGlu1	Metabotropic glutamate receptor 1
PC	Purkinje cell
Penk	Proenkephalin
PF	Parallel fibre
PLI	Purkinje layer interneuron

PV	Parvalbumin
Pvalb	Parvalbumin (gene)
ROI	Region of interest
SC	Stellate cell
SST	Somatostatin
STP	Short term plasticity
UBC	Unipolar brush cell
US	Unconditioned stimulus
VGLUT	Vesicular glutamate transporter
VIP	Vasointestinal peptide
VOR	Vestibulo-ocular reflex

Table of figures

INTRODUCTION

RESULTS

RESULTS SUPPLEMENTARY

Overview

The cerebellum is a brain structure important for various motor and cognitive behaviours. The cerebellar cortex integrates and processes sensory and motor variables with high temporal precision, important for generating accurate behaviour. Molecular layer interneurons are a key component within the circuitry of the cerebellar cortex. My thesis project is centred around exploring how molecular layer interneurons represent sensorimotor variables and understanding to what extent they exhibit a diversity in neural signatures that might be important for how they encode and further relay information.

The first part aims to provide a general introduction of the organisation, role and mechanisms of functions of the cerebellum, with a focus on the circuitry of the cerebellar cortex. With particular consideration to the molecular layer interneuron population, I will address possible input and intrinsic factors underlying heterogeneities in their population which may underlie a diversity in function.

The second part will present my findings about the laminar diversity of molecular layer interneurons representing sensorimotor variables, within the behavioural context of whisking.

The discussion will further address the possible relevance of this observed diversity for the cerebellar circuit dynamics, and for behavioural outcomes. I will lastly propose further experimental trajectories that could deepen our understanding about the implications of the molecular layer interneurons functional diversity.

Ultimately, the functional mechanism of molecular layer interneurons might provide a more generalizable framework for neural circuitry functionality, with insight into key elements disrupted in disease.

I. Introduction

II1. The cerebellum: role and function

The cerebellum or as the translation from Latin implies, “the little brain” is one of the evolutionary oldest brain structures conserved across jawed vertebrate species. It is a posterior brain region located underneath the evolutionary more recent neocortex. The cerebellum represents only 10% of the brain mass, but is estimated to incorporate around 80% of the total number of neurons in humans. This is mostly due to its granule cell layer composed of densely packed neurons, hence giving this “granular” aspect (Herculano-Houzel, 2010; Van Essen et al., 2018). Throughout evolution, the human cerebellum has also expanded to a greater extent than the neocortex, incorporating in its tightly folded structure an equivalent of 78% of the total surface area of the neocortex (Sereno et al., 2020). By comparison, the surface area of the macaque cerebellum is equal to only 33% of the neocortex’s. This uneven cerebellar expansion suggests its important role in human behaviour and cognition and its precise role and mechanisms of function are being actively researched.

I1.1 Landmarks in the study of the cerebellum

I1.1.1 A short historical overview

Historically, the cerebellum’s main role and function have been linked to movement control and coordination. This originated from early-on lesion studies through animal experimentations in the 19th century (Glickstein et al., 2009) and from clinical observations of War veterans with cerebellar gunshot injuries that developed what Gordon Holmes conceptualized as ataxia, a neurological disease characterized by body tremors, instable gait and impaired balance (**Figure I1.A**; Holmes, 1917). The advancement of microscopy and staining techniques such as the Golgi method at the end of the 19th century, allowed laying the groundwork of the cerebellar cortex cellular anatomy, primarily through the pioneering drawings of Santiago Ramón y Cajal (**Figure I1.B**; Sotelo, 2003).

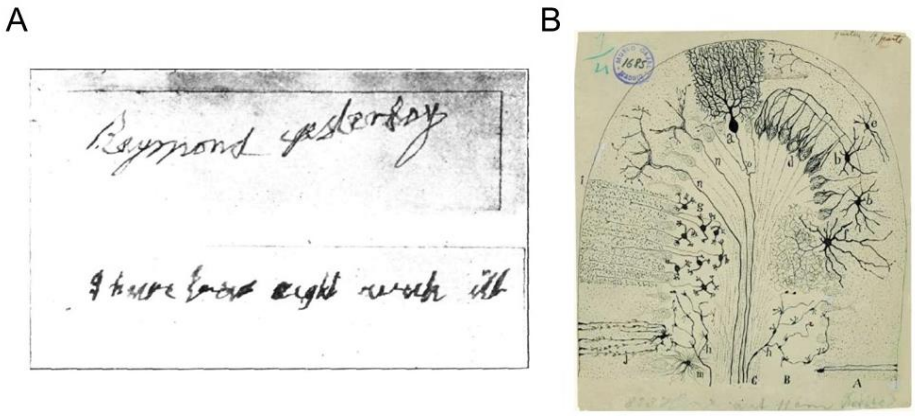

Figure I1. Early assessments of the cerebellum anatomy and function
(A) Example writing samples of two patients with right-sided cerebellar injuries: (*upper*) "Raymond, yesterday", (*lower*) "I have been eight weeks ill". From Holmes, 1917.
(B) Drawing of a parasagittal view of the cerebellar cortex cellular organization made by Ramón y Cajal in 1894: A, molecular layer; B, granule cell layer; a, Purkinje cell; b, basket cell; c, axonal projections forming the white matter; d, pericellular projections of basket cells; e, stellate cells; f, Golgi cells; g, granule cells; h, mossy fibre; i, granule cells axons ending forming coronal parallel fibres (depicted by dots); j, Bergmann glia; m astrocytes; n, climbing fibres; o, Purkinje cell collateral. From Sotelo, 2003.

I1.1.2 Overview of the cerebellar circuit and information flow

The emergence of electrophysiology in the 20th century, refined modern frameworks of thinking in neuroscience linking fine cytoarchitecture to functionality and information flow (Eccles et al., 1967; Palay & Chan-Palay, 1974). Mossy fibres (MFs) originating from various brainstem regions transmit sensory and motor information to the granule cells (GCs), which further form long ascending axons known as parallel fibres (PFs) that target the sole output neurons of the cerebellar cortex, the Purkinje cells (PCs). This forms an excitatory feed-forward flow of information through glutamatergic synapses (MFs → GCs → PCs). The PCs further form inhibitory GABAergic connections onto deep cerebellar nuclei (DCN), while other MFs also directly project to the DCN. The second source of sensorimotor excitatory inputs integrated in the cerebellar cortex arrives via climbing fibres (CFs). They originate exclusively from the inferior olive (IO) in the medulla oblongata region of the brainstem and target PCs (CF → PC). A PC is contacted by a single CF through a thousand of glutamatergic synapses making its input powerful and effective. Within this arrangement two types of feedforward inhibition arise: 1) through Golgi cells (GoCs) which are contacted by MFs - but also from PFs as a feedback inhibition- and in turn inhibit GCs and 2) through molecular layer interneurons (MLIs) composed of two morphological subtypes, namely stellate cells (SCs) and basket cells (BCs)

that receive their input from the PFs and exert their inhibitory effect on the Purkinje cell (PC) dendrites and soma, respectively (**Figure I2**).

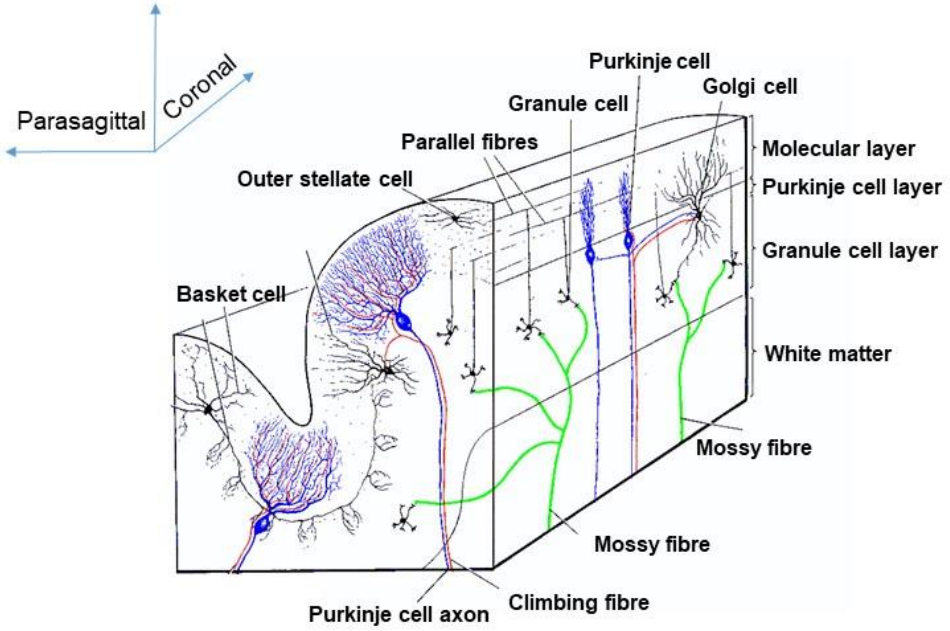

Figure I2. Three-dimensional scheme of the cerebellar cortex neuronal architecture (*upper-black*) Outer-stellate and deeper-basket cells, ascending axons from granule cells forming parallel fibres and Purkinje cells dendritic trees, composing the Molecular layer; (*blue*) Purkinje cells with somas residing in the Purkinje cell layer; (*lower-black*) Granule cells and Golgi cells residing in the Granule cell layer; (*red*) Climbing fibres; (*green*) mossy fibres. Adapted from Carpenter, 1991.

I1.1.3 Emerging theories of cerebellar learning and pattern separation

Given this configuration, computational models of cerebellar learning were conceptualized for the first time by David Marr (Marr, 1969), Masao Ito (Ito, 1970) and James Albus (Albus, 1971). Their interpretation was rooted in this observed "*regularity*" and "*relative simplicity*", as both James Albus (1971) and David Marr (1969) described the cerebellar cortex neural connectivity, comprising of a few neuronal types. They each concluded that a central mechanism for learning would be based on the transformation of PF to PC synapses as conditioned by CFs. However, their theories differed in the interpretation of the mechanisms governing those transformations. David Marr postulated that through repeated pairing, the CF would act as a teaching signal to strengthen PF to PC synapses through long term potentiation (LTP) and thus induce learning. Meanwhile, the inhibition provided by GoCs and MLIs would adjust the threshold of GCs and PCs, respectively.

On the other hand, James Albus and Masao Ito viewed the CF input as an error signal that weakens the PF to PC synapse, thus inducing long term depression (LTD) of the co-activated synapses. This would induce a learned and lasting change in the PF activity configuration. Future afferent MF signalling therefore induces through the PF pathway the appropriate PC response even in the absence of the "teacher" CF. James Albus also assigned a differential role to BCs and SCs, through which BCs targeting directly the PC soma provide a fast inhibition, while SCs targeting the PC dendrites help speed up its membrane repolarization following activity induced by the PFs (Albus, 1971; Marr, 1969).

Furthermore, GCs have an average of four short dendrites and receive a confined range between 2 and 7 MF inputs each (Eccles et al., 1967). Packed within a highly dense layer, GCs outnumber MF boutons at a ratio of 2.9 to 1 in mice (Billings et al., 2014). This suggests that the incoming information from MFs is broadened in the larger number of receiving GCs, while individual GCs are active only when given a specific combination of MF inputs. Those observations to two key elements of the Marr-Albus theory, namely expansion recording and sparseness coding. Together, they have the role to minimize the overlap between spatial and temporal patterns of GC population activity, creating diverse pattern of PF input that PCs can appropriately learn through CF error signalling: "*The notion fundamental to this is that the mossy fibre-granule cell articulation is essentially a pattern separator*" (Marr, 1969). David Marr estimated that less than 5% of the GCs should be co-activated at any given time, for avoidance of PF input saturation and efficient PC learning (Marr, 1969, reviewed in Cayco-Gajic & Silver, 2019).

Following 50 years from the proposed Marr-Albus-Ito theory, ideas about cerebellar learning mechanisms evolved (Cayco-Gajic & Silver, 2019). Firstly, Marr's hypothesis of LTP induction during CF signalling was mostly falsified in the favour of the LTD (Ito, 2001; Ito & Kano, 1982).

Secondly, evidence that single GCs can integrate a rich, mixed representation of information from multiple modalities (Chabrol et al., 2015; Huang et al., 2013; Ishikawa et al., 2015; Proville et al., 2014) reinforces expansion recording. Moreover, specifically silencing the output of three thirds of the cerebellar GCs by eliminating P-type calcium channels, has been shown to impair the acquisition of motor learning without affecting the overall motor performance (Galliano et al., 2013).

Thirdly, the notion of sparsity was particularly challenged. Experimental recordings of temporally dense activity in murine GCs have recently been shown (Chen et al., 2017;

Giovannucci et al., 2017). Given that GCs can fire at spontaneous rates of over 100 Hz during locomotion and sensory stimulation (Powell et al., 2015; Van Beugen et al., 2013), highlights the importance of defining the time window of signal integration of a given sparse pattern. However, ultrafast population coding in the cerebellar cortex seems unlikely at those activity rates (Cayco-Gajic & Silver, 2019). As the cerebellum is required to encode large amounts of multisensory and motor information in short timeframes to generate temporally precise behaviour, lower level of activity sparseness could improve the generalizing capacity of the network and information (Billings et al., 2014; Spanne & Jörntell, 2015). Moreover, sparsity of population coding might not necessarily be a prerequisite of pattern separation, as it was achieved when modelling both sparse and dense GCs activity (Cayco-Gajic et al., 2017). In turn, the study highlights synaptic sparsity instead and proposes that sparsity of the connectivity at the level of MF to GCs synapses is the required component for pattern separation and decorrelation. This sparse connectivity is highly conserved across vertebrate species (S. S.-H. Wang et al., 2016), suggesting a functional importance. Also, mechanisms of short-term dynamics between MF – GC synapses can further enrich temporally precise sensory representation through GCs specific neural signatures and, thus, promote pattern separation (Barri et al., 2022; Chabrol et al., 2015).

Ever-improving techniques of optic (such as optogenetics; Deisseroth, 2011; Mahn et al., 2018) and imaging tools (multi-photon microscopy and functional dyes; Liu et al., 2022; Salomé et al., 2006; Sun & Schaffer, 2018; Yang & Yuste, 2017; Zhang et al., 2023) combined with electrophysiology multiple site recordings (such as Neuropixels; Jun et al., 2017) provide neuroscience research with means to measure and manipulate large amounts of cellular activity with milliseconds precision. Ongoing studies continue to probe computational theories and shape our understanding of the link between neural circuit dynamics and behaviour through empirical evidence. A growing amount of studies use cerebellar dependent behaviours to examine its functionality and information processing (De Zeeuw, 2021; Z. Gao et al., 2012; Houck & Person, 2014; Raymond & Medina, 2018), while others have revealed new roles of the cerebellum in cognition and reward signalling (Kostadinov & Häusser, 2022; Wagner et al., 2019).

In return, computational models are constantly being refined to perform within biological parameters and produce realistic outcomes (Barri et al., 2022; Cayco-Gajic et al., 2017; Chalk et al., 2018). This process leads to perfecting our understanding of brain functionality in healthy and diseased states (D'Angelo & Casali, 2013) and has applicability as

far as the realm of robotics. Acknowledging the efficiency of cerebellar mechanisms in compensating for variabilities in sensorimotor delays, a recent study incorporated a cerebellar network-inspired computation controller to overcome transmission-variable time delays and optimize motor learning and adaptation in human-robot interactions (Abadía et al., 2021).

It is an exciting time to explore the mechanisms underlying cerebellar functions. With this in mind, I will further expand on the neuronal architecture of the cerebellar cortex and sensorimotor processing, with a focus on MLIs.

I1.2 Organization of the cerebellum

Recently, a study used single-nucleus RNA sequencing and an analysis that enables to determine the spatial context of the expression pattern known as spatially resolved transcript amplicon readout mapping analysis, to assess evolutionary patterns in the brain (Kebschull et al., 2020). They found that the cerebellar nuclei evolved across species by repeatedly duplicating a unitary module of conserved cell types, with varying transcriptomic divergence and projection targets of the excitatory neurons. Based on this comparison of mice, chicken and humans, they argue an evolutionary model of "*duplication and divergence*". Indeed, a modular organization has been observed within the cerebellar cortex with repeated unitary motifs of confined cell types, called microzones, as well as a lobular organization with specific input and output patterns. This 1) medio-lateral axis of parasagittal modules (Apps et al., 2018) together with a 2) rostro-caudal axis defining lobules and a further 3) depth axis of laminar cellular expression type and subtype diversity (Arlt & Häusser, 2020; Bao et al., 2010; Hoehne et al., 2020; Kozareva et al., 2021; Straub et al., 2020), create three main axes of heterogeneity in the cerebellar cortex functionality. The cerebellum shows specific lobular organisation (unilateral or bilateral) for different cognitive or motor tasks (**Figure I3**; Schmahmann, 2019). Deviating from the classic feed-forward models, the cerebellar circuitry is more recurrent than previously thought and rich in diverse cellular populations and subpopulations, suitable for different learning modalities (reviewed in De Zeeuw, 2021). The following section will address this anatomo-functional arrangement of the cerebellum and discuss the layers of complexity added to its functionality by a diversity of cellular types and subtypes that go beyond what was originally thought.

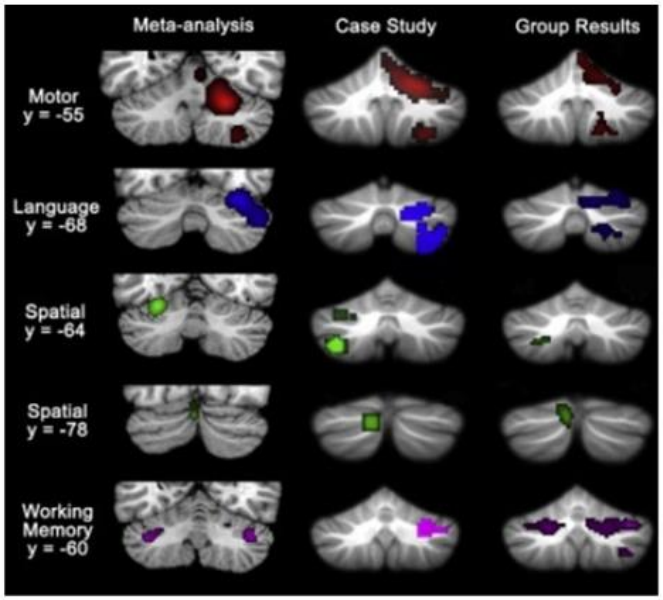

Figure I3. Functional topography of the human cerebellum during different tasks

Cerebellar areas engaged by motor (*red*), language (*blue*), spatial (*green*) and working memory (*purple*) tasks recorded using a functional magnetic resonant imaging (fMRI) scanner. From Schmahmann, 2019.

I1.2.1 Gross anatomy and cerebellar lobules

The cerebellum, a hindbrain structure located in the posterior cranial fossa of the skull, underneath the cerebrum (in humans), enclosed by the tentorium cerebelli, a protective sheath of dura matter. It is connected with other brain structures and the spinal cord through bundles of nerve fibres forming the three cerebellar peduncles: the superior, middle and inferior peduncle. The surface of the cerebellum is formed by a highly convoluted structure, the cerebellar cortex, underneath which lies a ramified white matter and three pairs of deep cerebellar nuclei (DCN) in mammals: medial (fastigial in humans), interposed (emboliform and globose in humans), and lateral (dentate in humans) nucleus. The DCN together with the vestibular nuclei constitute the output of the cerebellum, forming large ipsilateral and contralateral projections throughout the central nervous system (Apps & Hawkes, 2009; Kebschull et al., 2020).

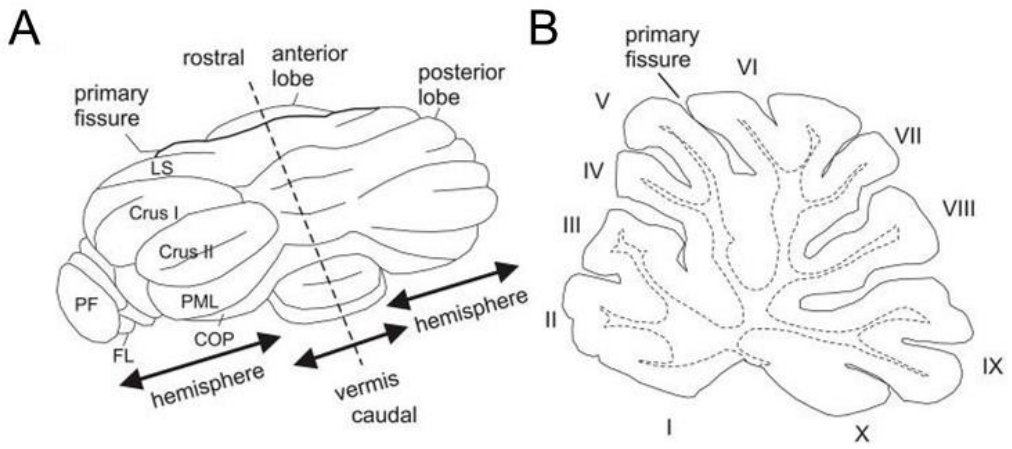

Figure I4. Gross anatomy of the cerebellum

(A) Dorso-posterior view of the rodent cerebellum and its anatomical subdivisions into the middle vermis, the two lateral hemispheres further subdivided into lobule simplex (LS), Crus I, Crus II, paramedian lobule (PML) and the copula pyramidis (COP) – the flocculus (FL) and paraflocculus (PF). Dashed line marks the midline plane of the section in panel B.
(B) Midsaggital cross section drawing of the lobular organization, I – X. Dashec line marks demarcates the cerebellar cortex from the white matter. From Cerminara et al., 2015.

The cerebellum is organized rostro-caudally into three lobes and 10 highly interspecies-conserved lobules, segmented as such by deep and superficial parallel folds called fissures and folia, respectively (**Figure I4**). The two deep folds form the primary and posterolateral fissures dividing the cerebellum into: 1) the anterior lobe comprising lobules I-V (with IVth and Vth lobes being fused in mice, while distinct in rats and humans), 2) the posterior lobe comprising lobules VI-IX and 2) the flocculonodular lobe or the vestibulocerebellum consisting of lobule X. The medio-lateral axis further divides the cerebellum into 3 orthogonal areas from the midline outwards, the medial vermis and bilaterally the paravermis and hemispheres. Functionally, the vermis and paravermis compose the spinocerebellum, while the hemispheres form the cerebrocerebellum (Apps & Hawkes, 2009).

The vestibulocerebellum represents the most phylogenetically primitive part of the cerebellum and is involved in balance and adaptive eye movements, receiving and projecting back to a high extent to the vestibular nuclei (Meng et al., 2014; Ono et al., 2000). Also, the spinocerebellum processes extensive inputs carrying proprioceptive and tactile information from different body parts via the ventral and dorsal spinocerebellar tracts and also the dorsal column nuclei in the brainstem (Matsushita & Hosoya, 1979; Yaginuma & Matsushita, 1989). It projects to the medial and anterior interposed nuclei to further relay information via the vestibular nuclei, reticular formation, red nucleus and the ventrolateral thalamus to various parts of the cortex and spinal cord (Fujita et al., 2020).

The phylogenetically most recent part of the cerebellum is the cerebrocerebellum (Van Essen et al., 2018). As the name implies, it has extensive reciprocal connectivity with various parts of the cerebral cortex (Kelly & Strick, 2003), important for fine-tuning temporally-precise movements, generating skilful behaviour and even affective processes (Chabrol et al., 2019; D'Angelo & Casali, 2013; J.-Z. Guo et al., 2021). Reinforcing the existence of a cerebellar-cerebral loop, strikingly similar cellular dynamics were recently observed between layer 5 neurons in the premotor cerebral cortex and lobule VI, Simplex and Crus I-II GCs in the cerebellum during a motor learning task (Wagner et al., 2019). Information arriving at the cerebellum extensively via the pontine nuclei (Nagao, 2004) is processed and projected via the lateral nucleus and the posterior interposed nucleus to several thalamic nuclei and further to the cerebral cortex (Amino et al., 2001). Interestingly, the cerebellar lobules Crus I and II preferentially connect with the prefrontal cortex and occupy a significantly larger proportion of the cerebellar volume in humans compared to other closely related primates such as chimpanzees and capuchins (Balsters et al., 2010). This indicates that Crus I-II cerebellar lobules could play a particularly important role in higher order human cognition.

I1.2.2 Neuronal architecture diversity and connectivity in the cerebellar cortex

The cerebellar cortex is composed of 3 layers named by the main type of neuronal cell bodies found within: 1) the deepest is the GC layer where the somas of the GCs reside and synapse with MFs, but also GoC and unipolar brush cells (UBCs) somas, 2) the PC layer where the PC somas are but also other type of Purkinje layer interneurons (PLIs) and 3) the most outer molecular layer where MLIs are found, as well as numerous dendrites from PCs, GoCs, PLIs and the long axons of GCs, the PFs (**Figure I5**).

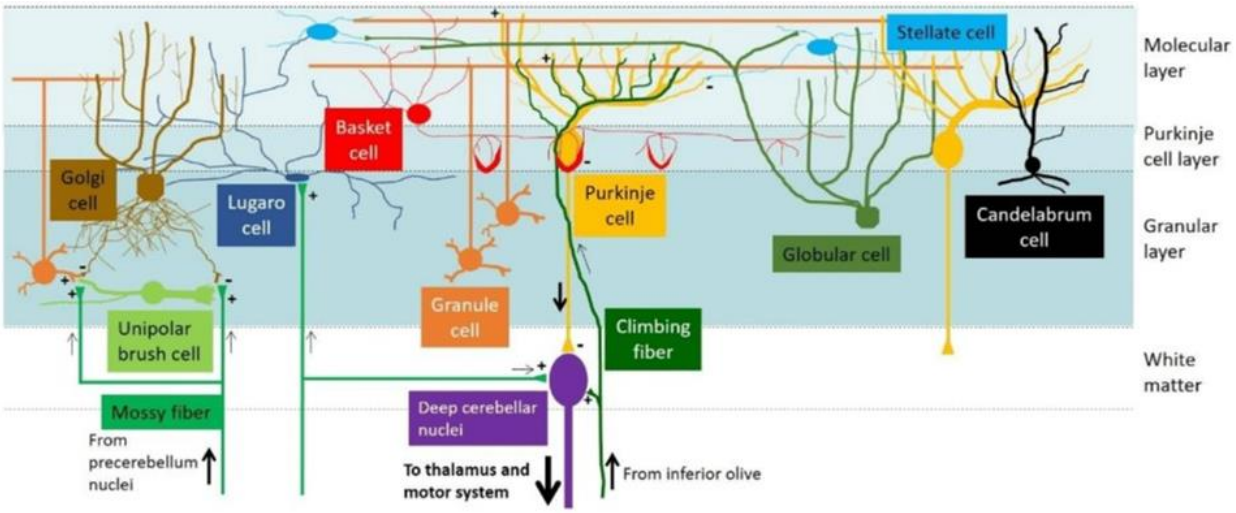

Figure I5. Extended neuronal architecture and connectivity of the cerebellar cortex
Purkinje cells (*yellow*) receive excitatory synaptic input from the parallel fibres of granule cells (*orange*) and inhibitory input from molecular layer interneurons formed by stellate cells (*light blue*) and basket cells (*red*) in the molecular layer. Purkinje cells integrate those signals and relay the final output to the deep cerebellar nuclei (*purple*). Mossy fibres and climbing fibres are the major afferents entering the cerebellum (in different shades of *green*). The granule cell layer also contains the excitatory interneuron unipolar brush cell (*light green*) and the inhibitory golgi cell (*brown*). Close or residing in the Purkinje cell layer are the Purkinje cell interneurons the candelabrum cell (*black*), globular cell (*dark green*) and Lugaro cell (*dark blue*) forming inhibitory connections with other interneurons and/or Purkinje cells. From Tam et al., 2021.

I1.2.2.1 Input into the cerebellar cortex: the mossy fibre and climbing fibre pathways

The cerebellar cortex integrates sensory, motor and cognitive information via the two main excitatory inputs, the MFs and CFs. Both MFs and CFs also send collaterals directly to the DCN, acting in synergy with the strong inhibitory input provided by the PCs to modulate its outcome to various regions outside the cerebellum (**Figure I5**; Najac & Raman, 2017; Shinoda et al., 2000; Zeeuw & Berrebi, 1995**)**.

MFs ascend towards the GC layer to contact primarily GCs (Palay & Chan-Palay, 1974), but also GoCs (Kanichay & Silver, 2008), UBCs (Mugnaini et al., 2011) and a type of PLI known as the candelabrum cell (CCs, Osorno et al., 2021). MFs arise from numerous sources in the brainstem (Huang et al., 2013), conveying direct sensory and motor information from peripheral nerves through various precerebellar nuclei, or pre-processed in the brain and relayed through cortico-cerebellar loops mostly via the pontine nuclei (Amino et al., 2001; Kelly & Strick, 2003; Nagao, 2004). As such, the lateral reticular nucleus and red nucleus integrate information regarding movement coordination from the spinal cord, cerebral cortex and trigeminal nuclei and relay it throughout the cerebellar cortex. Trigeminal nuclei relay information involved in facial sensorimotor information to the hemispheres and the vermis via

the inferior peduncle (Ikeda & Matsushita, 1992). The vestibular nuclei send MFs carrying information regarding balance, posture and control of eye movements (Voogd et al., 1996). The pontine and tegmental pontine reticular nuclei are a major source of MFs to the lateral cerebellar hemispheres, but also to the vermis and vestibulo-cerebellum to a smaller degree (Serapide et al., 2001). They relay somatosensory, visual and auditory information, as well as information important for planning and fine movement execution, from multiple areas in the cerebrum. The DCN also input back into the cerebellar cortex to provide feedback efferent copies of the movement important for associative learning (Gao et al., 2016; Houck & Person, 2014).

CFs originate in the inferior olive nucleus of the ventral medulla. The inferior olive is subdivided into the principal dorsal, medial accessory and principal olives. Those nuclei receive inputs from brainstem (reticular formation, trigeminal nuclei, dorsal column nuclei, mesodiencephalic junction, red nucleus and periaqueductal grey in the midbrain) spinal and cerebral regions with diverse functional roles (Berkley & Worden, 1978), some of which also form MFs. In the cerebellar cortex, the CFs terminate in the molecular layer, where they make extensive excitatory contacts with the primary and secondary dendrites of multiple PCs. Meanwhile, each PC is contacted by only one CF through thousands of glutamatergic synapses, which generate strong excitation onto the PCs known as complex spikes (Palay & Chan-Palay, 1974). Indirectly, the CF input can sometimes have the opposite effect, through a "*spillover*" of glutamate onto the inhibitory MLIs (Arlt & Häusser, 2020; Coddington et al., 2013; Szapiro & Barbour, 2007). Interestingly, this spillover can also affect GoCs, ultimately influencing the GC to PC activity (Nietz et al., 2017).

I1.2.2.2 The granule cell layer

The GC is the most abundant and densely packed neuron type in the nervous system, with a density of 1.77 x 10^4 cells / mm^2 in the rat cerebellum (Harvey & Napper, 1991). Morphologically, they have a small soma of 5-6 µm in diameter compared to other brain neurons, and an average of 4 small thin dendrites ending in claws (Eccles et al., 1967; Palay & Chan-Palay, 1974). MF boutons contact up to 1000 GCs though their claws within a specialized structure created by glial ensheathing, called glomeruli. Thus, the MF-GC connectivity forms a main pathway of information flow to the cerebellar cortex. As discussed in the previous chapter (see section I1.1.3), this arrangement might be ideally suited for integrating incoming information from multiple modalities and expanding sensory patterns relayed further to PCs.

The axons of the GCs emerge from their somas and ascend towards the molecular layer where they bifurcate in the "T-shaped" PF that run bilaterally in parallel to each other on the coronal plane up to 2 mm in length in mice (Huang et al., 2006; **Figure I5**). On its way, the PF makes numerous excitatory synapses with PCs and also with MLIs, GoCs and CCs (Osorno et al., 2021; Palay & Chan-Palay, 1974). PFs are estimated to form 9 times more contacts with PCs than with inhibitory interneurons (Pichitpornchai et al., 1994). GCs in turn receive inhibition from GoCs (**Figure I5**). PCs also send collaterals to directly inhibit GCs in regions specialized in regulating eye movement and processing vestibular information within lobules VI, IX and X (Guo et al., 2016).

A growing consensus suggests that GCs are not a homogenous population (Consalez et al., 2021; Markwalter et al., 2019; Straub et al., 2020). Initial morphological observations suggested that generally larger GCs are found in the vermis compared to the hemispheres (Palay & Chan-Palay, 1974), while new transcriptomic analysis reveal three molecularly distinct subtypes with nonuniform distributions across cerebellar regions (Cerminara et al., 2015; Consalez et al., 2021; Kozareva et al., 2021). Even within a region they show functional diversity (Straub et al., 2020). Although, usually considered as a uniform assembly, it is not surprising that GCs subpopulations would have specialized properties adapted to the regional input (relationship with modular organization discussed in next section I1.2.3). For example, a recent study suggest that GCs encode sensory modalities such as locomotion, somato-sensory visual and auditory to different degrees (Markwalter et al., 2019). As such, about a half of vermal GCs respond to locomotion and air puff stimulation and to a lesser extend to visual and auditory stimuli, with a diversity kept consistent across early and late born GCs. In addition, local diversity might aid decorrelation of MF input (Barri et al., 2022; Chabrol et al., 2015), however the exact role of this heterogeneity in information processing remains an open question.

GCs are inhibited to a great extent by GoCs, releasing GABA and sometimes glycine, onto thousands of GCs. They have an important role in modulating the fast and powerful transmission between MFs and GCs. If under low inhibition, a single action potential (AP) can induce postsynaptic spikes in GCs (Chadderton et al., 2004) , the presence of GoCs can institute the requirement of activity of multiple MF or bursts of single MFs, to translate into GCs responses (Jörntell & Ekerot, 2006; Rancz et al., 2007). Spontaneously firing at ~5Hz, GoCs provide constant tonic inhibition, but also, phasic inhibition, with variability between the two (Crowley et al., 2009). Many reasons might account for this diversity in inhibitory effect such

as the number of GCs dendrites or claws within a glomerulus (Palay & Chan-Palay, 1974), the GABA receptor expression (Crowley et al., 2009) or intrinsic differences of GoCs subtypes and synaptic modulation (Fore et al., 2020; Kozareva et al., 2021). Their rich processing flexibility is enhanced by GoC to GoC connectivity (Vervaeke et al., 2012). They share PF input through electrical coupling and can also inhibit one another (Hull & Regehr, 2012). Molecularly they show two distinct subclasses, of which only one expresses *Gjd2* gene encoding for the gap junction receptor expressed in GoCs, connexion 36 (Kozareva et al., 2021). Those subclasses separated by electrical coupling might be involved in providing the multidimensional activity seen in relationship to whisking and locomotion *in vivo* (Gurnani & Silver, 2021).

The UBC is an excitatory interneuron, located within the GC layer with high regional variability (Mugnaini et al., 2011). They are targeted by MFs and can transform their brief input into sustained responses of several hundred GCs (**Figure I5**). They also target other UBCs. Traditionally viewed as ON or OFF based on their response to MF inputs, it is more recently suggested that in fact MF bursts evoke continuously varying responses across the UBC population (C. Guo et al., 2021; Kozareva et al., 2021), that might enhance temporal scales of learning (Hull & Regehr, 2022). Studies in electric fish reveal that UBCs are important in distinguishing self-generated from sensory input, which might have an important equivalent role in mammals (Sawtell, 2017).

I1.2.2.3 The Purkinje cell layer

The large ~20 µm soma of the PCs, which is almost four times bigger than the GC soma, delimitates the PC layer. As mentioned before, the PC is the sole output of the cerebellar cortex and unlike most projecting neurons which are excitatory, the PCs release the inhibitory neurotransmitter gamma-aminobutyric acid (GABA). The PC has a vast dendritic arborisation confined on the parasagittal plane, that extends into the molecular layer, covering on average 8000 μm^2 and containing a high density of spines at ~17 spines/µm in rats (Harvey & Napper, 1988; Nedelescu et al., 2018). The dendrites of PCs can integrate excitatory signals from thousands of PFs perpendicularly crossing on the coronal plane (Palay & Chan-Palay, 1974), which is central to information processing in the cerebellum (Apps & Garwicz, 2005). PF-PC synapses undergo LTD through CF input during learning (Ito, 2001). Over 70% of those dendrites are estimated to be silent (Ho et al., 2021; Isope & Barbour, 2002) and Aps can be induced by the co-activation of an order of 50 GCs (Barbour, 1993). Moreover, the spike

frequency has been linearly correlated to the number of active GCs inputs to the target PC (Walter And & Khodakhah, 2009). With increase intensity, this input could however shift to a burst of simple spike and subsequent firing pauses (Zang & De Schutter, 2021) .

The PC axons are myelinated and provide strong high frequency (∼20–100 Hz) inhibition, projecting to their main target the DCN (Zeeuw & Berrebi, 1995). The PC input converges in the DCN at a ratio of ∼40:1, but only a small fraction of this synchronized input is required to influence the DCN network (Person & Raman, 2012). PC axons also form collaterals that target other PCs, MLIs, GoCs and PLIs of which CCs and Lugaro cells, as well as GCs in some cerebellar regions and UBCs to some extent (C. Guo et al., 2016, 2021; Hirono et al., 2012; Orduz & Llano, 2007; Osorno et al., 2021; Witter et al., 2016). This provides regulatory feedback inhibition on the parasagittal plane and help maintain synchronized oscillatory activity within PC networks (De Solages et al., 2008; Witter et al., 2016).

PCs are also a heterogeneous population, with a specific organization into functional parasagittal modules (discussed in length in the next section I1.2.3) and regional differences in morphological aspects such as dendritic density, arborisation overalap and spatial occupancy (Nedelescu et al., 2018).

The Purkinje cell layer also contains, within or in close proximity, the somas of inhibitory PLIs namely the globular interneurons, Lugaro cells and CCs (Hull & Regehr, 2022; Lainé & Axelrad, 1994, 2002; Miyazaki et al., 2021; Osorno et al., 2021; Palay & Chan-Palay, 1974; **Figure I5**), that might extend throughout all regions of the cerebellar cortex (Kozareva et al., 2021). PLIs are not included into the classical cerebellar circuit and are usually left out from functional models, perhaps because they have not been well characterised so far. Lugaro cells are GABAerging/glycinergic with a characteristic fusiform soma (Palay & Chan-Palay, 1974). Similar to CCs, GABAergic/glycinergic Lugaro cells and glycinergic globular cells are inhibited by PCs (Hirono et al., 2012; Lainé & Axelrad, 2002). Lugaro cells inhibit locally other interneurons, namely the GoCs and MLIs, but can also have long-ranging axon projections within the cerebellar cortex (Miyazaki et al., 2021), although further research needs to be done to characterize their connectivity.

However, a recent study shows a vast network connectivity of CCs, suggesting a complex role in modulating cerebellar information flow (Osorno et al., 2021). Their dendrites extend into the molecular layer where they are excited by GCs, but also by MFs at their basal dendrites. CCs are also inhibited by PCs collaterals. In turn they provide GABAerging (and possibly

glycinergic) inhibition primarily to MLIs, but also PCs and to some extent to GoCs. The inhibition to MLIs suggests that their effect might be overall a disinhibition of PCs, but further investigation into their function is needed.

I1.2.2.4 The molecular layer

The molecular layer is an area of extensive information processing (most of which is mentioned in the above subsections of I.1.2.2), where GC axons ascend following initial integration of MF input, as well as CFs and multiple neural dendrites of PCs, PLIs and GoCs (**Figure I5**). The most abundant type of inhibitory interneurons in the cerebellar cortex, the MLIs, reside in this layer and participate to this connectivity network. Considering all neurites and somas, the molecular layer is estimated to incorporate 41% of the total cerebellar volume (Harvey & Napper, 1991). Mostly confined within the molecular layer, MLIs have a similar orientation to PCs, extending their neurites in the parasagittal plane and receiving orthogonal excitatory input from PFs (Palay & Chan-Palay, 1974). As mentioned previously, they can also receive an indirect glutamatergic spillover from CFs synapsing onto PCs (Arlt & Häusser, 2020; Szapiro & Barbour, 2007). In turn, MLIs send feed forward inhibition to PCs and, to some degree, receive inhibition back from PCs (Mittmann et al., 2005; Witter et al., 2016). About 20% of MLIs can also inhibit other MLIs, as well as themselves through autapses (Kondo & Marty, 1998b; Pouzat & Marty, 1998). Interestingly, the synaptic density of MLIs can vary based on depth, with deeper MLIs receiving a high amount of PCs collaterals to their somas, and decreasingly towards the outer layer, less MLI inhibition and increasing PF input (Lemkey-Johnston & Larramendi, 1968b).

MLIs are sometimes considered as a homogenous computational unit of threshold adjusters (Barri et al., 2022; Marr, 1969), or as an overall coherent population in response to behaviour (Chen et al., 2017; Gaffield & Christie, 2017; Ma et al., 2020). Nevertheless, increasing evidence suggests high heterogeneity in their functional roles (Albus, 1971; Arlt & Häusser, 2020; Astorga et al., 2017; A. M. Brown et al., 2019; Chu et al., 2012; Hoehne et al., 2020). Based on position within the molecular layer and their morphological differences, an initial classification dates back to Ramón y Cajal, who observed two typologies of MLI: 1) one residing primarily in the outer two-thirds of the molecular layer that has multiple dendrites in a star-like radial arrangement, thus named Stellate cells (SCs), and 2) the other type residing in the inner third, has few dendrites and a characteristic axon surrounding the PC soma and its

proximal axon like a basket, hence the name Basket cells (BCs, Palay & Chan-Palay, 1974; Sotelo, 2003). Indeed, morphological differences can underlie distinct functional properties. The basket-like shape formed by BCs is known as a pinceau, and it is a specialized structure for extremely rapid ephaptic signals that induce sub-millisecond PC inhibition (Blot & Barbour, 2014).

This morphological classification was used to assess functionality for over a century. As postulated by James Albus (1971), BCs target directly the PC soma to provide a fast inhibition, while SCs targeting the PC dendrites help speed up its membrane repolarization following activity induced by the PFs. Indeed, BCs can powerfully modulate PC activity (Arlt & Häusser, 2020; Blot et al., 2016; A. M. Brown et al., 2019), while SCs perform dendritic integration which might act as a temporal filter (Abrahamsson et al., 2012).

Unlike SCs, BCs also show a high degree of electrical coupling through gap junctions (Hoehne et al., 2020) on their dendritic tree, that extends on the parasagittal plane (Alcami & Marty, 2013; J. Kim et al., 2014; Rieubland et al., 2014). Gap junction coupling might, therefore, promote PCs synchrony by narrowing their time window of activity. However, manipulation of SCs and BCs population activity to question their differential role has been limited by a lack of specific markers. A recent study took advantage of gene expression at specific developmental time points to conditionally target subsets of BCs and SCs, respectively (A. M. Brown et al., 2019). Based on this differentiation, they show that supressing outer MLIs increase PC simple spike regularity, while suppressing inner MLIs increases PC simple spike frequency.

Moreover, new approaches to classify MLIs reveal two molecularly distinct classes MLI1 and MLI2 (**Figure I6.A**), that are expressed throughout the molecular layer and do not correlate with the previously morphologically defined MLI types (Kozareva et al., 2021). They have different physiological properties, with MLI1 showing higher rates of spontaneous activity and less sensitivity to depolarisation compared to MLI2. Also, of the two classes, only MLI1 form electrical connections. However, it is not fully clear if MLI1 represents a distinct functional population with continuously varying properties or it can be further subdivided into two discrete subtypes (MLI1_1 and MLI1_2). Although there are depth gradients in some genes expressed (such as for *Grm8* encoding for a type of glutamate receptor), it seems that the classification into SCs and BCs is incomplete. Moreover, MLIs show a continuum of dendritic and axonal morphological variation across depth with intermediate morphological types present in the middle part of the molecular layer (**Figure I6.B**; Sultan & Bower, 1998; W. X. Wang &

Lefebvre, 2022). This could further translate into a gradual change in properties and functionality. However, whether there is a segregation into functional subtypes and their influence on postsynaptic target and behaviour remains to be investigated.

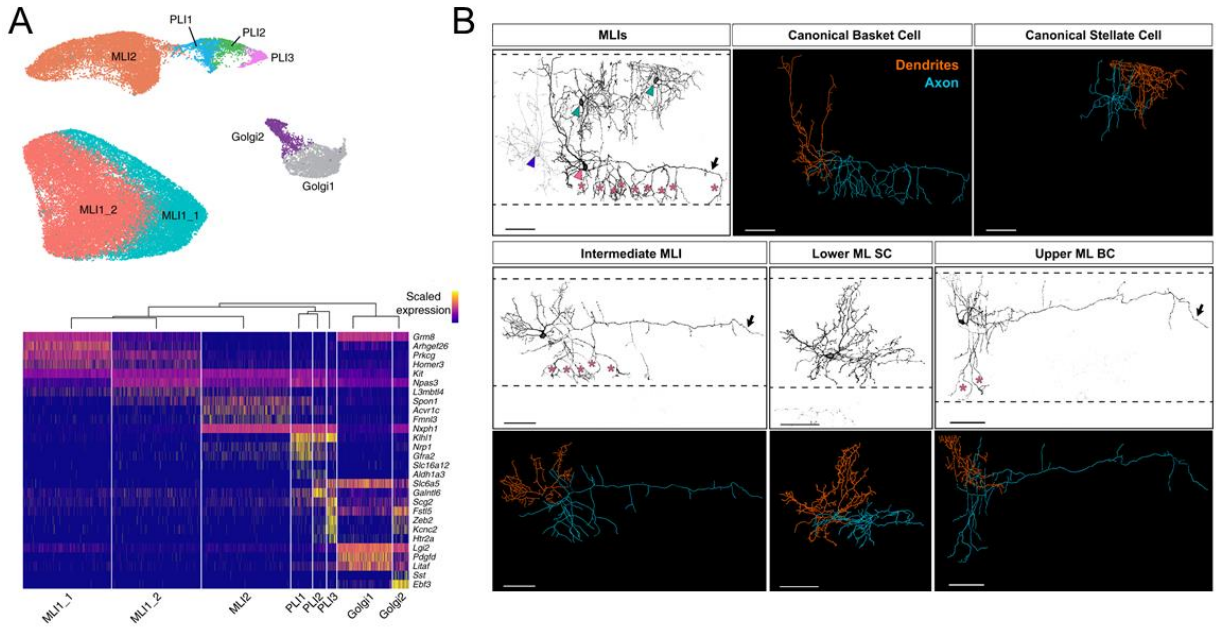

Figure I6. Molecular characterisation and continuum of morphological MLI subtypes

(A) Expression pattern of cerebellar inhibitory interneurons characterized using snRNAseq: (*upper*) uniform manifold approximation and projection plot of their expression profile and (*lower*) scaled RNA expression of key differentially expressed genes in the subclasses cerebellar inhibitory interneurons. From Osorno et al., 2021.
(B) Morphological continuum of MLIs: Example of inverted fluorescence image of canonical BC (pink arrowhead) and SC morphology upper ML (teal arrowheads) and lower ML (purple arrowhead) (*upper-left*). The BC targets the initial segment of the PCs somas and axonal initial segment (pink asterix). The reconstructions of the neurites of the MLIs depicted on the left with their dendrites (orange) and axon (blue) (*upper-middle and right*). Representative images (*middle*) and neurite reconstructions (*bottom*) of MLIs showing a mixture of BC and SC characteristics. Scale bars are 50 µm. From W. X. Wang & Lefebvre, 2022.

I1.2.3 Modular organization

Besides the lobular structure, the cerebellar cortex exhibits a medio-lateral organization into parasagittal strips. Those segregated neuronal microcircuits are called microzones and are believed to represent the functional units of the cerebellar cortex (Apps et al., 2018; Oscarsson, 1979; Voogd, 2011). This parasagittal topography is dictated by distinct functional connectivity and protein distribution, suggesting a segregated processing of motor and cognitive information (Apps & Garwicz, 2005; De Zeeuw, 2021; Oscarsson, 1979).

Functionally, compartmentalization of PC activity was reported based on their complex spike responses to topographically connected CF inputs (Garwicz et al., 1998; Hesslow, 1994). PCs from a given microzone further project to a specific set of vestibular or DCN neurons, establishing a microcomplex (Apps & Garwicz, 2005; De Zeeuw et al., 1994; Zhou et al., 2014). The corresponding CF synchronized activity originates from electrically coupled olivary neurons (Llinas & Sasaki, 1989). They, in turn, receive inhibitory feedback from region-specific vestibular and DCN neurons, together creating segregated functional loops called micromodules (**Figure I7**; Apps et al., 2018; De Zeeuw, 2021; Voogd & Ruigrok, 2004).

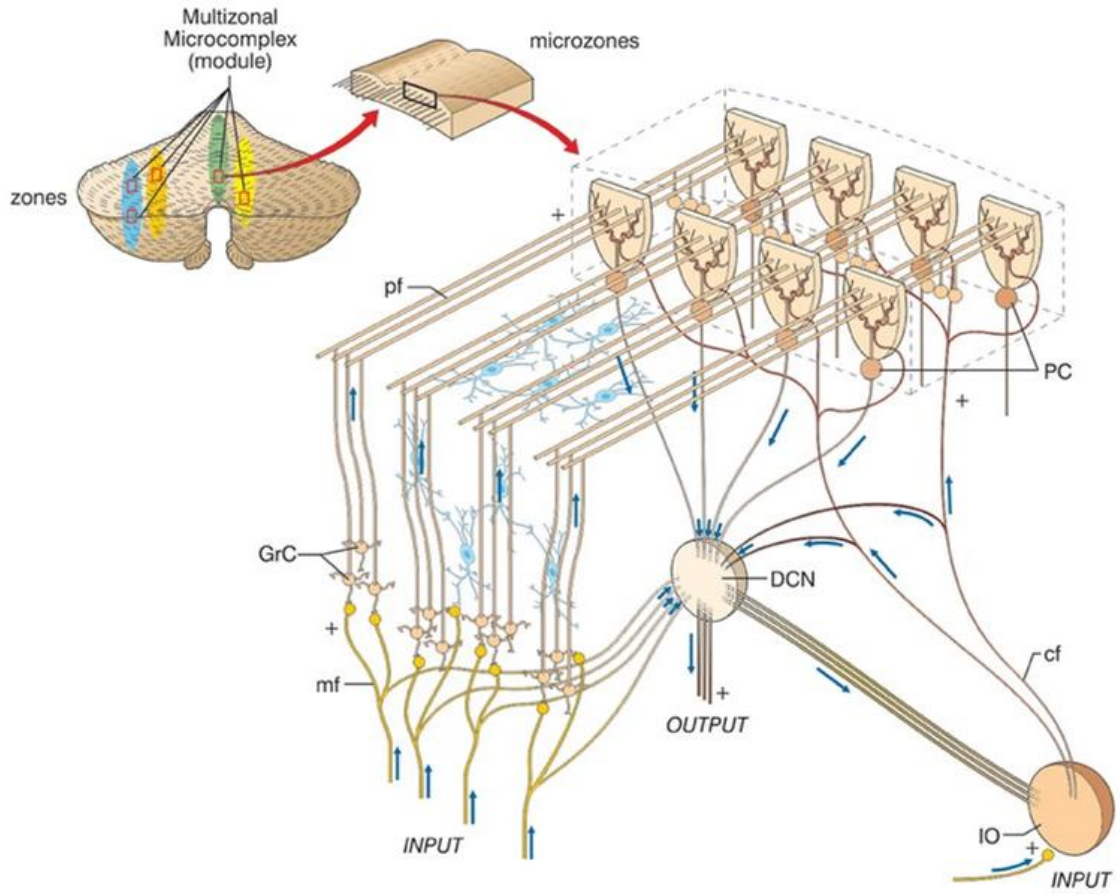

Figure I7. The modular organization of the cerebellum

The schematic depicts a flatten view of the cerebellum with four ideal coloured *zones*, each containing *multizonal microcomplexes* or *modules,* further divided in functional units called *microzones*. The microzone structure is formed by narrow sagittal stripes of about 1000 PCs sharing the same receptive field, orientated perpendicular to the cortical folds and the crossing PFs. Axons of BCs run preferentially in the direction of the PC dendritic trees restricted to a large extend to a microzone. CFs from electrically coupled neurons in the inferior olive usually innervate PCs within a given microzone, enhancing synchronization of firing. PCs belonging to a microzone send their axons to the same cluster of the DCN. From D'Angelo & Casali, 2013.

Anatomically, parasagittal bands in the cerebellar cortex were observed over 60 years ago, by staining the 5'-nucleotidase enzyme (Scott, 1965). The Zebrin (I and II) neurochemical markers, were further reported to stain alternating positive and negative parasagittal bands (reminiscent of a zebra) of expressing and non-expressing PCs, respectively (Gravel et al., 1987; Hawkes et al., 1985). The identity of Zebrin II was confirmed to be the Aldolase C enzyme (Ahn et al., 1994), important for glucose metabolism and synthesis. Since then, a transgenic mouse line targeting Aldolase C has been engineered to allow brain wide fluorescent tagging and functional mapping (Fujita et al., 2014).

Interestingly, zebrin defined compartments were matched to the modular input of CFs (Apps & Hawkes, 2009; Sugihara & Shinoda, 2004), hence to the microzone organization to a wide extent (De Zeeuw, 2021). Other markers have been associated with PCs expression of *PLCB4*, which complements that of Aldolase C (Apps et al., 2018; Cerminara et al., 2015; Rodriques et al., 2020). About a 5^{th} of the genes spatially associated with PCs (from a total of 669 genes) can be significantly correlated or anti-correlated with Aldolase C or *PLCB4* expression (Rodriques et al., 2020). PCs also show different intrinsic excitability properties between zebrin positive and negative bands, with firing frequencies (both complex and simple spikes) and regularity (simple spikes) being significantly higher in the latter (Viet et al., 2022; Xiao et al., 2014; Zhou et al., 2014). This difference was associated with the expression of the *PLCB4* activated non-selective cation channel TRPC3 (Zhou et al., 2014) and the SK channel which is a calcium dependent potassium channel (Viet et al., 2022). *In vivo*, the functional loss of TRPC3 can impair cerebellar dependent learning (Wu et al., 2019).

Moreover, PCs induce different plasticity properties at the GC-PC synapse, due to differential expression of the glutamate transporter EAAT4, which is higher in zebrin positive bands (Wadiche & Jahr, 2005). The activation of EAAT4 clears the glutamate, preventing the activation of the metabotropic receptor mGluR1 at the GC-PC synapse and the PC inhibitory feedback. This in turn limits LTD at the GC-PC synapse during concomitant activity of CFs and PFs, which may lead to the microzone-specific cerebellar learning. Modular-dependent differences have also been reported at the level of CFs, which show increased release of glutamate at CF-PC synapses and induce prolonged complex spikes in PCs (Paukert et al., 2010). This is believed to be independent of EAAT4 mediated synaptic properties in PCs, as those modular differences persist in EAAT4 knock-out mice. As a result, synaptic plasticity and strength of inhibition to the DCN could also be depend on CF modular differences.

Therefore, functional differences between zebrin positive and negative bands can provide an indirect link between heterogeneous protein expression and physiological diversity (Cerminara et al., 2015; De Zeeuw, 2021; Z. Gao et al., 2012; Rodriques et al., 2020). Also, both GoC and MLI activity seem compartmentalized into microzones reinforcing this functional organization through parasagittal inhibition to GCs and PCs, respectively (W. Gao et al., 2006; Valera et al., 2016).

As described so far, differences between microzones are related to protein expression and functionality within a highly repetitive neuronal architecture. A more drastic segregation is provided by UBCs, which reside to a high extent in zebrin positive bands (Chung et al., 2009; Consalez & Hawkes, 2013). This reflects a further specificity of information processing between microzones.

Unlike CFs, MFs originate from various brainstem regions. However, they might share patterns with CFs inputs into microzones and send congruent projections between those microzones and DCN (Apps & Hawkes, 2009; I. E. Brown & Bower, 2001; D'Angelo & Casali, 2013). MFs also show to some extent alternating bands in their expression of the vesicular glutamate transporters (Gebre et al., 2012), reflecting a patterned cortical and subcortical input to the cerebellum through VGLUT1 and VGLUT2, respectively. Nevertheless, it is not always a clear cut, as single MFs can have terminals concomitantly in zebrin positive and negative bands (Quy et al., 2011).

It is important to note that, adjacent microzones are interconnected by perpendicularly running long beams of PFs on the coronal plane (**Figure I7**), forming connection with hundreds of different PCs and MLIs that might, however, have selective modular connectivity (Galliano et al., 2013; Harvey & Napper, 1991; Palay & Chan-Palay, 1974; Valera et al., 2016). Interestingly, heterogeneous molecular markers in GCs reveal regional differences into transverse band and patches (Cerminara et al., 2015; Consalez et al., 2021). For example, patches of the enzyme acetylcholinesterase are expressed in congruence with zebrin positive bands (Boegman et al., 1988), suggesting a spatially distributed cerebellar processing through acetylcholine mediated neuromodulation (Fore et al., 2020). The topography of the GCs input is therefore complex. Although GCs run in coronal beams, most PFs synapse onto PC only with a probability of ~0.5 (Harvey & Napper, 1988), while many existing GC-PC synapses are silent (Ekerot & Jörntell, 2001; Ho et al., 2021; Isope & Barbour, 2002). Moreover, the anatomical and functional patches of GCs organization have been attributed to a "*fractured somatotopy*", conserved across species, that can sometimes overlap with the parasagittal distribution, but not

necessarily (Apps & Hawkes, 2009; Bower, 2011; Shambes et al., 1978). This spatial organization is defined as such by the receptive field of the MFs, which terminate in multiple areas within the GC layer (Quy et al., 2011; Woolston et al., 1981). Trigeminal MFs inputs relaying facial information show this "patchy" distribution throughout lobules Simplex, Crus I – II and IX (Woolston et al., 1981). Such patches have been demonstrated in response to cutaneous stimulation in Crus I – II lobules (Shambes et al., 1978).

Overall, a combination between patched incoming information that can extend transversally and functional parasagittal modules, might form an ideal organization for multimodal information processing.

I1.2.4 Developmental milestones

Developmental stages can give us important insight into functional and connectivity properties conserved throughout adulthood. Although the timeline of developmental stages differs between rodents and humans, the development of the cerebellar cortex starts during embryonic stages and undergoes maturation postnatally, in the first weeks or months, respectively. I will further focus on data from mice and rats. The inhibitory and excitatory neurons in the cerebellar cortex have two separate progenitors: 1) PCs, GoCs and MLIs are derived from the ventricular zone, while 2) GCs and UBCs from the germinal layer of the rhombic lip (reviewed in Rahimi-Balaei et al., 2018). PCs progenitors start migrating around E13. Immature PCs only acquire a monolayer in the first postnatal week, while their neurites mature during the first 3 weeks of life (**Figure I8**; Altman, 1972b). While derived from the same germinal zone, MLIs differentiate and migrate in the first 2 postnatal weeks, when they support the development of the PC dendritic tree. Even from those early stages, mostly earlier born BCs and later born SCs may have separate roles: BCs promote the perpendicular outgrowth of the primary PCs dendrite, while SCs support the expansion and ramification of the secondary branches (reviewed in Schilling, 2022). A recent study takes advantage of the different developmental expression of the gene *Ascl1* to mark early born (embryonic expression) and late born (postnatal days) MLIs separately (A. M. Brown et al., 2019). Consequently, this method produces a laminar labelling and a high degree a segregated marking of BCs and SCs, respectively.

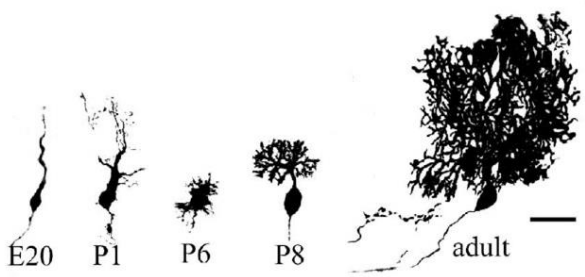

Figure I8. Maturation of the Purkinje cell

Sequence of the different stages of dendritic maturation of the PC from the end of their radial migration (E20) to adulthood with an initial extension (P1) and regression stage (P6) followed by the ultimate dendritic tree maturation onward. PCs are filled with rat horseradish peroxidase dye. Scale bar is 50 µm. From Sotelo, 2004

The GCs are generated within the germinal layer at the cerebellar surface around E20 and start migrating at birth through the future molecular layer. In their descent to form the GC layer, their axons start growing on the mediolateral axis, giving rise to PFs (Rahimi-Balaei et al., 2018). This migration persists up to 3 weeks after birth, producing a laminar effect, by which early born GCs produce PFs in the lower molecular layer, while later born GCs have PFs increasingly closer to the surface (Altman, 1972a; Eccles et al., 1967; Espinosa & Luo, 2008; Zong et al., 2005). Based on birth sequences, it is possible that earlier arising spinal and reticular MFs (E12-E15) could connect to lower layered GCs, while pontine MFs (from E15) would project higher to connect to upper GCs (Altman & Bayer, 1980a, 1980b, 1980c, 1980d, 1981). In contrast, other studies have suggested that MFs can span throughout the entire depth of the GC layer (Krieger et al., 1985; Palay & Chan-Palay, 1974). Interestingly, although this suggests that they contact to a similar degree both inner and outer GCs, it might be possible that they preferentially contact clusters of GCs born at specific time points (T. Kim et al., 2023). As those clusters also span the depth of the GC layer, but show laminar projection of their PFs (Espinosa & Luo, 2008; Zong et al., 2005), this depth dependent effect might be visible in PFs (Wilms & Häusser, 2015) and onto the next step of processing, in MLIs and PCs.

The input pathways into the cerebellar cortex develop at different times. Olivary neurons start earlier at embryonic days 12-13 (E12-13) (Bourrat & Sotelo, 1991). Guided by molecular cues expressed by PCs, CFs start exerting their influence early on, contacting PCs in a topographical manner around E20 and persists maturation (and pruning) up to around postnatal day 21 (P21) under postnatal influences of PFs (Chedotal & Sotelo, 1993). In contrast, brainstem nuclei mature throughout embryonic stages (~ E12-E22) and establish MF contacts

within the cerebellar cortex in the first postnatal weeks (Altman, 1972c; reviewed in Leto et al., 2016).

It is possible that the modular organization is developmentally driven. Evidence suggests that PCs are generated from distinct post mitotic clusters (Hashimoto & Mikoshiba, 2003). The early (E10-11.5) and late (E11.5-13.5) birth date of PCs partially determines the location into zebrin positive and negative bands, respectively (Apps & Hawkes, 2009; J. Zhang et al., 2021). Locally, PCs collaterals send patterned spiking that help refine the downstream network from neonatal stages (Watt et al., 2009). The CF parasagittal topography is established in neonatal rodents, suggesting that CF input might be spatially selected to some extent by PCs types (Sotelo et al., 1984). Furthermore, aberrant projections of CF as well as MFs is seen in Aldolase C mutant mice (Blatt & Eisenman, 1988; Leto et al., 2016; Reeber et al., 2013; Sotelo, 2004).

Experimentally, perturbing cerebellar function in juvenile mice (P21) reveals lobule dependent abnormal cognitive and social behaviour during adulthood, such as motor learning (lobule VI, crus I) novelty seeking (lobule VII) and social performance (Crus I-II) (Badura et al., 2018). Moreover, those behaviours were affected to a greater extent compared to perturbations during adulthood, suggesting a key developmental window for acquiring normal functionality of some behaviours.

Falling within the "*nature versus nurture*" debate, developmental rules (*nature*) may predicate the first lines of axial organization and molecular heterogeneity that set the boundaries within which functionality and experience derived learning (*nurture*) can occur.

I1.3 Sensorimotor integration in the cerebellar cortex

Learning and sensorimotor processing require the ability to represent different contexts, by discriminating between patterns with sub-millisecond temporal precision (Cayco-Gajic & Silver, 2019). The cerebellum is classically known to be involved in motor coordination and adaptation, a sequential execution of behaviours that requires a very high temporal precision within timescales of a tens to hundreds of milliseconds (Paton & Buonomano, 2018). However, the biological mechanisms underlying this temporal processing and encoding within neural networks remain elusive. The next section will give a short overview on temporal processing in the brain. I will further introduce how the cerebellar integrates sensory and motor ques

needed to generate temporally precise behaviour and learning, with a focus on the whisker system.

I1.3.1. Neural representation of time and models of temporal encoding

Conceptually, time is a vast and hard to grasp philosophical notion. Nevertheless, our brains have a remarkable capacity to incorporate time in their functionality in order to fine tune our behaviours to the dynamic environment we live in (Buzsáki & Llinás, 2017). The taxonomy of time implies three important dimensions: subsecond versus suprasecond timing, interval versus pattern timing and sensory versus motor timing (Paton & Buonomano, 2018). Those dimensions are needed to generate properly timed behaviours but might imply different mechanisms at both cellular to network scales.

Considering the intrinsic properties of neurons, axonal time delays models were amongst the first to try and explain how timing is encoded in the brain (Jeffress, 1948). Especially, the long axons of cerebellar granule cells, known as parallel fibres, were thought to function as delay lines of activity (Braitenberg, 1967). Nevertheless, most animal communication sensory timing requires timescales of up to hundreds of milliseconds and those type of models cannot explain timing intervals above tens of milliseconds (Paton & Buonomano, 2018). Potassium and calcium channels have fast kinetics of tens of milliseconds, while ionotropic receptors work within the range of hundreds of milliseconds. Also, synapses can exhibit rapid changes in strength in response to a sequence of consecutive presynaptic spikes, known as short-term synaptic plasticity (STP).

It is now understood that multiple neural and synaptic properties such as excitatory-inhibitory balance and short-term synaptic plasticity act together to create temporal filters. For example, the state-dependent network, is an intrinsic model of sensory timing based on those flexible sets of mechanisms. At a population level, the neural properties given by STP and changes in excitatory-inhibitory balance (referred to as the hidden state) translate in temporally specific properties of the neural network. Activating the same population of input fibres at different times generates a specific pattern of activity, because the neurons respond different depending on the state of the network at each given time (Buonomano & Merzenich, 1995). Therefore, STP is an important factor for temporally selective neurons.

This distinction between sensory and motor timing has been proposed as an important dimension within the taxonomy of time (Paton & Buonomano, 2018). Sensory timers rely on

temporally selective neurons in the brainstem and sensory cortex to behave as temporal filters within a passive mechanism that does not necessarily need to produce a timed motor response. In contrast, motor and implicit timing relies on an active mechanism capable of generating a timed signal.

An alternative state-dependent model for motor timing is the population clock (Hardy & Buonomano, 2016). A population clock implies a neural trajectory in a state space, with each neuron participating in the population clock acting as a variable that codes for a specific moment in time. Importantly, those trajectories emerge internally, from the dynamics of the neural circuits and form a readout of elapsed time for neurons downstream in the circuitry. Those population clocks can take various forms throughout the brain, ranging from sparse to complex patterns of activity, and in some cases the speed of the population clock co-varies with the behaviour (Bakhurin et al., 2017; Paton & Buonomano, 2018). In the simplest form, a sequential chain of feed-forward neuronal activation, called a synfire chain, could be enough to produce a sparse pattern of activity such as for producing bird songs (Abeles, 1982). Although, it has been suggested that underlying dynamics might be due to a more complex recurrent architecture implying well-timed subthreshold inputs to the synfire chain neurons (Long et al., 2010).

Ramping is another feature of some populations of neurons that is believed to be important for timing. Those neurons exhibit linear changes in firing rates. When the threshold value is reached, actions are produced (Balcı & Simen, 2016). Experimentally, ramping neurons have been observed in many brain areas during timing tasks, it is unclear whether they are the timers themselves or act as a prerequisite for tuning upstream neurons that encode time in the changing pattern of neural activity (Paton & Buonomano, 2018).

A general feature of time perception is that it respects Weber's law, which means that it has a scalar property implying a constant coefficient of variation (Gibbon, 1977). In motor timing tasks such as duration discrimination or delayed reinforcement, the standard deviation of the response time across trials increases linearly with the mean of the interval being timed. Both ramping and population clocks can account for temporal scaling. However, population clock models seem better suited to generate complex spatiotemporal patterns needed for complex behaviour such as speech or Morse code (Hardy & Buonomano, 2016). Furthermore, the functionality of individual neurons within the population clock may reflect Weber's law (Tiganj et al., 2017).

Moreover, some animals have temporally selective neurons that respond to specific intervals or rate of activity. For example, mormyrid electric fish's medium ganglion cells can create negative images that predict sensory input caused by the fish's electric organ discharge, therefore distinguishing between the weak external electric field of pray and their own (Carlson, 2009; Kennedy et al., 2014; Sawtell, 2017). This accurate cancellation of self-generated sensory input is thought to be acquired through the activity of GCs in the fish cerebellar-like-structure (Kennedy et al., 2014). As such, GCs integrate proprioceptive and self-generated electrical information from MFs and generate a variety of firing profiles, under the instructive temporal patterns of UBCs.

Interestingly, new data suggests that time-dependent decisions are dependent on speed and patterns of neuronal activity (Monteiro et al., 2023). Using temperature to manipulate striatal neural population dynamics, Buonomano's team was able to influence the judgement of duration in rats, without affecting movement kinematics. It would be worth exploring if manipulating other brain regions, could influence different aspects of this task. For example, cerebellar cooling and heating could in turn influence movement kinematics and latency, similar to optogenetic perturbation during reaching (Becker & Person, 2019).

Overall, some areas of the brain have temporally selective neurons that respond to specific intervals or rate of activity and exhibit ramping type firing (Balcı and Simen, 2016). Other timing mechanisms are believed to rely on population clocks which are internally emerging state-dependent networks. They imply a neural trajectory in an N-state space, with N neurons each coding for a specific moment in time. Motor and implicit timing rely on an active mechanism capable of generating a timed signal, for which the cerebellum might be a key component as will be discussed in the next section.

I1.3.2. Cerebellar dependent behaviours and learning

The cerebellum has a historically established role in movement coordination (see section I1.1.1; Glickstein et al., 2009; Holmes, 1917). Incoming sensory and motor ques need to be constantly assessed with high temporal precision, in order to accurately adapt behaviour in real time. Therefore, this process cannot completely rely on slow feedback control and must incorporate an *internal model* of expectation (Ohyama et al., 2003; Wolpert et al., 1998). The internal model can function on predicting a motor command based on the current state (*forward model*), or by generating the motor command based on the desired outcome (*inverse model*).

Those models can act in synergy to generate movement based on prediction and then compare the outcome with the sensory feedback to correct future movement (Moberget & Ivry, 2016; Wolpert et al., 1998). The internal model can then be refined through learning to produce skilful outcomes, similar to a supervised learning algorithm (Raymond & Medina, 2018).

At the cellular level, GCs can reliably encode multisensory information incoming from MFs (Barri et al., 2022; Chabrol et al., 2015; C.-C. Huang et al., 2013), while PCs activity closely mirrors movement parameters (reviewed in Medina, 2011). In this way, the cerebellar cortex receives this sensorimotor information and processes it within microzones (discussed in section I1.2.3) to produce a well calibrated "*instructive*" outcome through the PCs activity (Medina, 2011). During sensorimotor association, the PC activity integrates with increased coherence through learning, information important for motor initiation and temporal precision, through the activity of simple and complex spikes, respectively (Tsutsumi et al., 2020).

Those models rely on a wealth of information from experiments on cerebellar learning and sensorimotor processing. Classic cerebellar dependent tasks such as the vestibulo-ocular reflex (VOR) and eyelid conditioning have been used extensively to examine the building blocks underlying skilful adaptation and interrogate cerebellar circuitries (**Figure I9**; De Zeeuw, 2021; Ito, 2001; Medina et al., 2000; Raymond et al., 1996). The VOR is a cerebellar dependent adaptive reflex that allows the stabilisation and maintaining of gaze by moving the eyes in the opposite direction to compensate for own head rotations or body movements (Ito, 1982). To achieve this the vestibulo-cerebellum (mainly the flocculus) incorporates incoming information: 1) about the motion and relative position of the head and body is detected by the inner ear's semicircular canals and otolith organs and relayed to the via the vestibular nuclei and from there to the vestibulo-cerebellum via the inferior cerebellar peduncle; 2) about vision relayed via the pretectal and pontine nuclei. The vestibulo-cerebellum processes the gathered information and projects instructive signals via the vestibular nuclei to modulate eye movements accordingly. In order to provide this fast adaptation that preceeds feedback mechanisms, the flocculus needs to establish an associative sensorimotor learning through pairing of visually driven CF input and vestibularly driven PF input (**Figure I1.B)**.

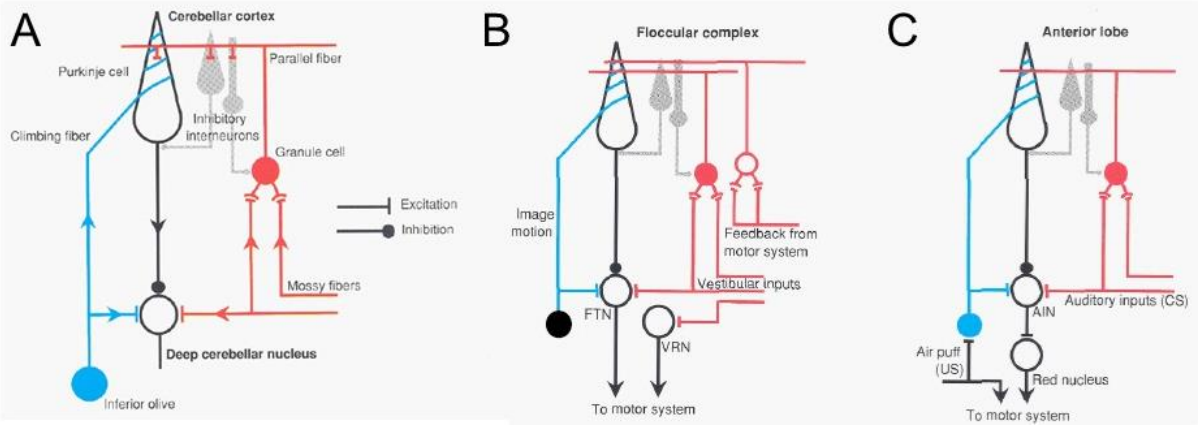

Figure I9. Schematic diagram of the cerebellar circuit involved in classic motor learning

(A) Schematic of the basic cerebellar circuit adapted in B and C, representing the MF ➔ GC➔ PF ➔ input to PCs (red) and the IO ➔ CF input (blue), as well as inhibitory interneurons (grey). **(B)** During VOR, PCs in the floccular lobe receive information about the vestibular system is transmitted by MFs from the brainstem vestibular neurons via GCs, while the visual input is conveyed by both CFs and MFs pathways. PCs project directly to the flocculus target neuron (FTN) in the vestibular nucleus. The motor system further converges information from the FTN and vestibular relay neurons (VRN), sending a feedback efference copy to the cerebellum.**(C)** The unconditional stimulus represented by the aversive air puff during eyelid conditioning are conveyed by CFs to the PCs in the anterior lobe and paired with the conditional stimulus represented by the auditory input is conveyed by MFs to the GCs and further to the PCs. Following learning, the targeted PCs produce a well-timed pause in their signal to the anterior interpositus nucleus (AIN) that further convey a signal to the motor system via the Red nucleus to precisely time the eyelid closure. From Raymond et al., 1996.

Taking advantage of this, the VOR was one of the first cerebellar dependent tasks used to interrogate the molecular basis of associative learning and support the PF-PCs synaptic LTD during CF "*teaching signals*" as an important mechanism underlying the PCs adjusted response (discussed in section I1.1.3; (Ito, 1982, 2001; Ito & Kano, 1982). A recent study developed an optogenetic tool for targeted control of the internalisation of AMPA receptors (Kakegawa et al., 2018). This is a crucial mechanism for inducing LTD, by reducing the number of depolarising sodium and potassium ions entering the postsynaptic neuron. This results in further reduced probability of inducing an AP in the presence of unchanged glutamate released decreases, therefore establishing LTD. Using this technique, they were able to directly manipulate the LTD at PF-PC synapses and consequently affect the VOR, demonstrating a causal effect between the two.

It must be mentioned that alternative learning mechanisms for the VOR have been proposed. As such, this learning occurs outside the cerebellum, in the vestibular nucleus and PCs provide instructive signals (Miles & Lisberger, 1981). In this conformation, the MF input

is already altered preceding the GC to PC synapses, and corresponds to the adjusted response of PCs (Lisberger et al., 1994). Although evidence of plasticity in the vestibular nuclei exists, a general consensus has been achieved that the cerebellum is essential for motor learning such as the VOR (reviewed in Boyden et al., 2004). The cerebellum might, however, rely on multiple plasticity mechanisms (Boyden et al., 2004; Schonewille et al., 2011). In fact, LTD alone cannot account for VOR related gain adaptation (and other cerebellar motor learning), as mutant mice deficient in internalisation of AMPA receptors at PF-PC synapses do not show impaired performance (Schonewille et al., 2011). LTD at PF-PC synapses is an important mechanism of motor learning that can be, however, overcome by compensatory mechanisms in mutant mice (Schonewille et al., 2011), but not during transient perturbation (Kakegawa et al., 2018). One of those mechanisms can be provided by MLI activity which acquires learning dependent changes during gain-increase VOR adaptation (Bonnan et al., 2023) and enhances CF mediated plasticity (Rowan et al., 2018). Moreover, those activity changes are necessary for the expression of the corrective motor memory (Bonnan et al., 2023). It is possible that MLIs may have a dual role to efficiently mediate CF induced PF-PC LTD via MLI-PC and MLI-MLI inhibition (thus PC disinhibition in 20% of the time), respectively (Kondo & Marty, 1998b). This role might be contoured by CF spillover (Arlt & Häusser, 2020) and by CCs and Lugaro cells which both inhibit MLIs (Miyazaki et al., 2021; Osorno et al., 2021).

Furthermore, the cerebellum can process various temporal representations during sensorimotor associative learning, with subsecond precision (Heiney, Wohl, et al., 2014; McCormick & Thompson, 1984; Medina et al., 2000). Experimentally, a specific Pavlovian delay, called the eyelid conditioning task, provides a powerful behavioural paradigm to directly probe the cellular and circuit mechanisms for this temporal learning (Heiney, Kim, et al., 2014; Heiney, Wohl, et al., 2014; Mauk & Donegan, 1997; Medina et al., 2000). Delayed temporal association between a sensory conditioned stimulus (CS – tactile, auditory or visual) and an aversive uncontained stimulus (US – air puff to the eye) have to be learned in order to precisely time the closure of the eyelid to the precise time of the US (**Figure I2.C)**. Only cerebellar cortex lesions can cause the loss of proper timing of eyelid closure, without preventing the conditioned response altogether (Kalmbach et al., 2010; McCormick & Thompson, 1984; Perrett et al., 1993). Similar to mechanisms of acquiring the VOR, the LTD at the PF-PC synapses during CF signalling can be applied for learning the eyelid conditioning (Medina et al., 2000). In this case, coincident CF signalling the US act as teaching signals for the GCs that are active at the time of the US, in order to drive LTD of their PF-PC synapses. Learning occurs through a

decreased GC excitatory drive (following LTD) to the inhibitory PC, causing them to pause their activity and release downstream disinhibition of DCN, finally resulting in a properly timed blink. This GCs activity pattern is properly timed.

The GCs have a particularly important role in learning the temporal delay between the CS and the US. While the aversive information of the US is conveyed via the CF-PC pathway, information about the sensory stimulus, which is at first neutral, is conveyed to the cerebellum via the MF-GC pathway (Medina et al., 2000; Steinmetz et al., 1989). Therefore, GCs may have an intrinsic temporal structure that transforms the incoming constant MF activity into a temporally diverse pattern (Medina et al., 2000; Rössert et al., 2015), thus acquiring a "*temporal basis*". It has been suggested that GCs function as a "*population clock*" , which is central to the ability of the cerebellum to intrinsically encode time (Barri et al., 2022; Buonomano & Mauk, 1994). After learning, the CS sensory context provided by the MF and encoded by the GCs, is sufficient to drive the appropriately timed PC response, in anticipation of the US, and without the need to CF activity.

Recently, it has been shown that GCs acquire a dense conditional response that matches or precedes the eyelid movement (Giovannucci et al., 2017). Therefore, alternative mechanisms at MF-GC synapses, such as STP, might be important to maintain the appropriate temporal dynamics of the pattern encoded (discussed in section I1.1.3; Buonomano & Merzenich, 1995; Cayco-Gajic & Silver, 2019; Chabrol et al., 2019). Moreover, other cellular mechanisms might be equally important in suppressing PC activity at the appropriate time. Tonic inhibition has been shown to differentially act during spontaneous and sensory-evoked responses and contribute to the reliable processing of sensory information in GCs (Duguid et al., 2012).

As seen with GCs, MLI activity also predicts the conditional blink response (ten Brinke et al., 2015). Suppression of MLI activity in paravermal lobule VI in juvenile mice impairs eyelid conditioning during adulthood (Badura et al., 2018), while mutant mice with impaired MLI function exhibit learning deficits (ten Brinke et al., 2015), reminiscent of effects seen during VOR (Bonnan et al., 2023). Interestingly, using a triple transgenic approach to impair LTD at PF-PC synapses or/and feed-forward inhibition at MLI-PC synapses, it was shown that only by supressing both those mechanism eyeblink conditioning is severely impaired. This suggests that those multiple mechanisms work in synergy to instruct the proper PC response and that when only one is disrupted, the other may compensate for the deficit (Boele et al., 2018). Also, the mechanisms underlying eyeblink conditioning may be mediated by TRPC3

function and, thus reliant on zebrin negative bands (also see section I1.2.3; reviewed in De Zeeuw, 2021; Wu et al., 2019).

Being far from understanding the cerebellar mechanism in all its complexity, the principles of motor learning discussed in relationship to the VOR and eyeblink conditioning can apply to a multitude of tasks to which the unique cerebellar processing might be detrimental. For example, the instructive CF signals might also act to cancel the sensory feedback produced by self-generated motion, which is fundamental to distinguishing the relevant sensory information from the environment (Blakemore et al., 1998). Indeed, it has been reported that neural activity differs between voluntary and passive head rotations in monkeys, highlighting the importance of the behaviour context (Brooks et al., 2015; Brooks & Cullen, 2013; Cullen, 2012). Other tasks that are cerebellar dependent include adaptive locomotion and skilled reaching (Becker & Person, 2019; Darmohray et al., 2019), sometimes in an interdependent manner (Albergaria et al., 2018). As such, locomotion can enhance motor learning during eyeblink conditioning, by increased MF input signalling (Albergaria et al., 2018).

Other studies highlight reward signals related to delivery, prediction as well as omission of reward, in the cerebellum especially in lobules VI, simplex and Crus I (reviewed in Kostadinov & Häusser, 2022). The cerebellum's diversity of function can be interpreted as a reflection of the diversity of input sources and output regions to which it is connected to (Medina et al., 2000). The cerebellum shows a direct input into the ventral tegmental area (a reward related region), which shows increased activity during social exploration (Carta et al., 2019). In return the cerebellum receives input from non-motor areas (Bostan et al., 2013).

The internal models governing cerebellar function might be suited for diverse cognitive functions and thus have broad purposes, applied to mental representation of intuitive and implicit thoughts (Ito, 2008; Moberget & Ivry, 2016). Consequently, cerebellar lesions or developmental abnormalities have implications in a spectrum of cognitive, emotional and social related diseases such as schizophrenia or autism (Badura et al., 2018; Craig et al., 2019; D'Angelo & Casali, 2013). As such, classic cerebellar related functions such as eyelid conditioning can be defective in autism patients and mouse models, in relationship to altered temporal prediction (D'Angelo & Casali, 2013; Kloth et al., 2015; Stoodley et al., 2017). This might point towards a generalised mechanism of cerebellar function and malfunction, worth exploring further.

I1.3.3. Whisker representations in the cerebellar cortex

Experimentally, the whisker system provides an ideal sensorimotor context, because in rodents it has a wide representation in the brain, including the cerebellum (reviewed in Bosman et al., 2011). It incorporates sensory representations with somatotopic arrangements (barreloids) relayed from the whiskers mechanoreceptors via the trigeminal nerve, as well as motor pathways for rhythmic and exploratory whisking from central pattern generators in the brainstem and cortical areas via the facial nerve (**Figure I10.A**). In the cerebellum, whisker stimulation of anaesthetised animals, was shown to induce temporally precise sensory representations in the lateral hemispheres (Crus I and II regions) at the level of both MLIs and PCs (Arlt & Häusser, 2020; Bosman et al., 2010; Chu et al., 2011, 2012), that can be enhanced by learning (Romano et al., 2018). Whisker movement kinematics are encoded by PC activity (S. T. Brown & Raman, 2018) and can be reconstructed from single PC simple spikes (Chen et al., 2016).

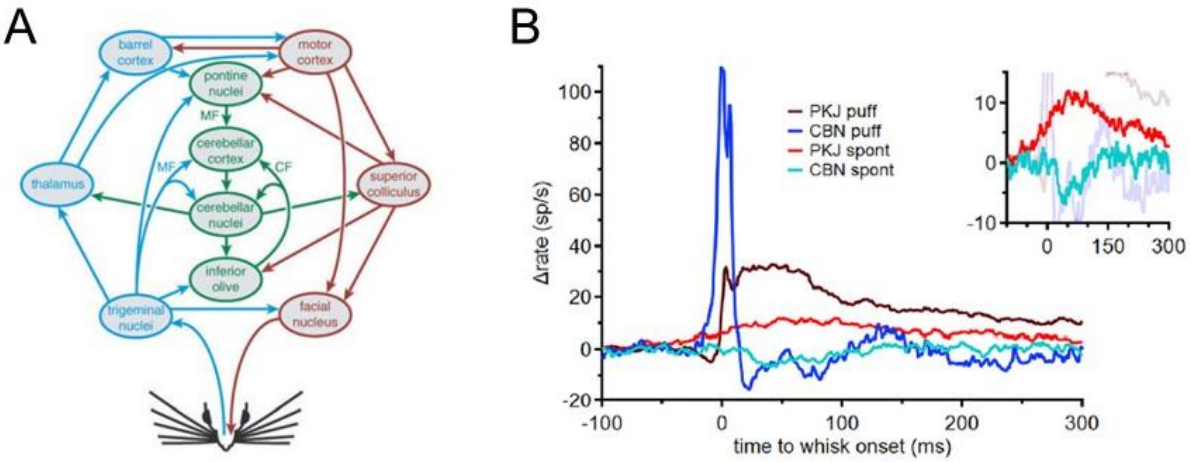

Figure I10. Whisker pathways and representation in the cerebellum

(A) Schematic of the main neuronal somatosensory (blue, left) and motor (red, right) pathways from and to the whiskers and its integration in the cerebellum (green, middle). *Direct trigeminal input*: The trigeminal nuclei send inputs to the pontine nuclei, inferior olive and cerebellar cortex. *Indirect cortical input:* information from the whisker pad travels to the trigeminal nuclei and thalamus to the primary somatosensory (S1) and motor (M1) cortex and through the pontine MFs to the cerebellum. The cerebellum converges direct and indirect mossy fibre (MF) and climbing fibre (CF) information. The processed cerebellar outcome is sent back to the cortex via the thalamus (*upstream cortical feedback loop*) and to the brainstem and spinal cord via the superior colliculus (*downstream motor areas*). From Bosman et al., 2010.
(B) Population instantaneous firing rates during spontaneous and puff-evoked whisking for Purkinje cells (PKJ, spontaneous: *red*, evoked: *brown*) and cerebellar nuclei cells (CBN, spontaneous: *cyan,* evoked: *blue*). From S. T. Brown & Raman, 2018.

Moreover, multiple pathways carrying information about the movement kinematics of the whiskers converge in Crus I and II, which receive input directly from the trigeminal nuclei and from higher order sensorimotor cortex via the pons (**Figure I10.A**; Bosman et al., 2011; Proville et al., 2014; Rondi-Reig et al., 2014). Moreover a strong convergence from sensory cortical regions (S1-2) via the cortico-pontine pathway (Leergaard et al., 2004), might imply the particular role of the cerebellum in processing the sensory aspect of whisking (Bosman et al., 2011). Interestingly, early Crus I-II representation of the whisker position does not depend on input from the primary motor cortex, while inhibiting the reticular formation only reduced later PC responses (S. T. Brown & Raman, 2018; Chen et al., 2016). This suggests that the initial ∼50 milliseconds of the response are initiated by the direct sensory-evoked input from the trigeminal nucleus and does not require sensorimotor feedback, as supported sensory representation in anaesthetised animals (Arlt & Häusser, 2020; Bosman et al., 2010; Chu et al., 2011). The later part of the PC response might however correspond to the rhythmic whisking-related internal motor commands conveyed by the brainstem (Kleinfeld et al., 2014; Takatoh et al., 2013).

In turn, the cerebellum might have an active role in coordinating this sensorimotor behaviour, through connectivity with the inferior olive, cerebral cortex (via the ventrolateral thalamus and basal ganglia) and facial nerve (via the superior colliculus and pons) (reviewed in Bosman et al., 2011). A recent study shows that optogenetically induced PC activity in Crus II during whisker stimulation, affects the coherence between primary sensory and motor cortical regions S1-M1 (Lindeman et al., 2021). Moreover, this effect is temporally precise and does not apply after a short 20 ms delay. As a behavioural consequence, the optogenetic stimulation of PCs was seen to suppress the amplitude of whisker protraction following stimulation (S. T. Brown & Raman, 2018). Interesting, PC stimulation during spontaneous whisking shifts the whisker set point without abolishing whisking completely (Proville et al., 2014). It is possible that only a fraction of PCs responsible for suppressing whisker related DCN cells were actually activated. Therefore, it is probable that this effect is underestimated and the complete effective silencing of the DCN whisker pathways might have stronger behavioural implications. Nevertheless, these effects highlight a partial role of the cerebellum in controlling sensorimotor processing and a possible differential processing in stimulated and spontaneous whisking. Indeed, the strong stimulus-induced activation of both PCs and DCN, is weaker or lacking during spontaneous whisking in PCs and DCN, respectively (S. T. Brown & Raman, 2018). As spontaneous whisking is self-generated as opposed to sensory-induced, it might have a similar sensory cancelation as seen during head rotations in monkeys (Brooks & Cullen, 2013;

Cullen, 2012, also discussed in previous section I1.3.2). Nonetheless, cerebellar cortex neurons including PCs, GCs and MLIs encode spontaneous whisker kinematics showing activity that follows or precedes the movement (Chen et al., 2016, 2017).

The information processing between the cerebellar cortex to the DCN differs in some key aspects. The PC simple spiking follows the full length of whisker kinematics during both spontaneous and sensory-evoked whisking (S. T. Brown & Raman, 2018; Chen et al., 2016), while the DCN activity is transient and centred around the onset of the sensory-evoked whisking and absent in spontaneous whisk (S. T. Brown & Raman, 2018). Interestingly, the strong initial response of the DCN is marked by a slight inhibition in PC simple spikes (**Figure I10.B**; S. T. Brown & Raman, 2018), suggesting a possible involvement of MLIs at this early stage (Barri et al., 2022; Chu et al., 2011). Interestingly, a simple training protocol comprising of repeated 4 Hz brief air puff-stimuli to the whiskers, can enhance both simple spike frequency in PCs and whisker protraction amplitude. Additionally, following training, optogenetic activation of the relevant PC in the early phase of protraction can further enhance this protraction (Romano et al., 2018). Repeated air puffs were also shown to induce adaptation of PCs complex spikes, which either increased or decreased in rate after a few tens of milliseconds and then followed the opposite pattern (Zempolich et al., 2021). Following adaptation, stimulus omission further suppressed complex spikes with different latencies, reminiscent of an error signal (Albus, 1971; Marr, 1969). Moreover, this differential pattern of complex spikes corresponds to different adaptations of basal simple spikes rates which decrease substantially only for the PCs with the initial decrease in complex spikes rates. The initial short-latency transient decrease in simple spike rate that is consistently reported (S. T. Brown & Raman, 2018; Chu et al., 2011), also seems to undergo habituation and gradually disappear in the PCs with the initial increase in complex spike rate (Zempolich et al., 2021). As previously seen for other learning tasks such as VOR and eyebink conditioning (discussed in section I1.3.2, Kakegawa et al., 2018; Medina et al., 2000), this learned adaptation reflects once more the dynamic interplay between the two pathways relaying sensorimotor information to PCs, namely the PFs and CFs inducing the simple spike activity and the complex spike activity, respectively.

With the end goal in mind, it is important to understand the relevance of this research to humans. As such, the cerebellar lobule relevant for sensorimotor representations of whisking Crus I show homology to monkey and human Crus I-II lobules (Sugihara, 2018). Those lobules have undergone a specific evolutionary expansion in skilful primates (and even more so in humans) and are highly involved in visuo-motor and cognitive functions (Balsters et al., 2010; Sugihara, 2018). Although whisker representation would not be of direct relevance, there might

be a correspondence with visuo-motor functions on which primates and humans are specifically reliant upon. Thus, simple whisker stimulation protocols can test general rules of information processing important for generating behaviour.

II2. Molecular layer interneurons: organization and role

Within the nervous system, interneurons are critical for the local processing and integration of information, despite constituting only ~10-30% of neurons in a given regions (Tremblay et al., 2016). They are mostly inhibitory, with different morphological, functional and neurochemical classifications across areas, such as the cortex (parvalbumin - PV, somatostatin - SST vasointestinal peptide - VIP and cholecystokinin expressing interneurons; Tremblay et al., 2016), cerebellum (BCs, SCs, GoCs but also PLIs; J. Kim & Augustine, 2021) and spinal cord (galanin interneurons, neuropeptide Y interneurons, PVs and calretinin expressing interneurons; Boyle et al., 2017). At the most basic level, they help maintain an excitatory-inhibitory balance, which if disrupted leads to neurological disorders such as epilepsy (Fritschy, 2008). Nonetheless, they have various functions in the type of inhibition they provide to projection neurons, but also to one another, leading to both inhibitory and indirect-excitatory effects.

In the cerebellar cortex, MLIs are the most abundant type of interneurons and are involved in many cerebellar functions, from associative learning, VOR, eyeblink conditioning to social behaviour, as highlighted in previous sections (Badura et al., 2018; Boele et al., 2018; Bonnan et al., 2023; Ma et al., 2020; Rowan et al., 2018; ten Brinke et al., 2015). An interesting feature about MLIs is that their target projection neuron is also inhibitory. The PC is derived from the same developmental zone (Rahimi-Balaei et al., 2018), and can inhibit back MLIs to some extent (Halverson et al., 2022; Witter et al., 2016).

Suitable to their broad behavioural role, MLIs express a high heterogeneity of neurochemical markers, suggesting more diversity than previously thought within a morphological continuum (see section I1.2.2.4, Kozareva et al., 2021; W. X. Wang & Lefebvre, 2022). Alongside their intrinsic heterogeneities, the pattern of connectivity might differ amongst MLIs and with other cell types. They have a predominantly sagittal interconnectivity and a depth gradient in electrical coupling (Hoehne et al., 2020; J. Kim et al., 2014; Rieubland et al., 2014). Moreover, at different depths MLIs might sample different ratios of input from GCs, PCs, and MLIs (Lemkey-Johnston & Larramendi, 1968b), as well as different GCs

subtypes (Straub et al., 2020). The modular organization or type of sensorimotor information relayed within a given lobule might further contributes to their diversity of function (see section I1.2.1 and I1.2.3).

Overall, heterogeneous intrinsic properties and connectivity patterns might underlie a complex role. This section is therefore dedicated to addressing how the input to MLIs and their internal properties might shape their diversity in function. I will then discuss what consequences this has on their output towards PCs and behaviour.

I2.1 Intrinsic properties of functional diversity in MLIs

MLIs have diverse spontaneous firing frequencies ranging between 1-35 Hz *in vivo* (Jirenhed et al., 2013; Ruigrok et al., 2011), matching with slice measurements of 1-41 Hz (Häusser & Clark, 1997). This consistency under the two experimental conditions, suggests that the properties underlying their firing patterns are intrinsic. Also, those frequencies are similar between SCs and BCs *in vitro* (Häusser & Clark, 1997). By comparison, in anaesthetised mice *in vivo,* SCs have a mean spontaneous firing rate of ~ 4 Hz which is higher than that of BCs at ~ 1 Hz (Chu et al., 2012).

Despite some functional differences between SCs and BCs, this morphological classification granted by Ramón y Cajal might be an oversimplification of their complex organisation required for this diversity of functions (see section I1.2.2.4). Within the brain, some morphological aspects can correspond to molecular expression. For example, the SC target the PC dendrites similar to how the SST interneurons mostly target the pyramidal cells dendrites, while the BCs target the PC soma in the same way PV interneurons target the pyramidal cell soma (Palay & Chan-Palay, 1974; Tremblay et al., 2016). Interestingly, about 20% of MLIs target other MLIs, which might have a distinct role in the cerebellar circuitry, reminiscent of cortical VIP interneurons (Karnani et al., 2016; Kondo & Marty, 1998b). Nonetheless, MLIs inhibiting other MLIs have not yet been segregated into a separate subtype.

It is possible that it has been harder to classify MLIs, as they all share PV expression together with their projection neuron, the PC. Novel functional classifications might be possibly based on gene expression, which shows that MLIs are more diverse than previously thought within a morphological continuum (Kozareva et al., 2021; W. X. Wang & Lefebvre, 2022). This is not surprising by comparison to other areas of the brain which also show high degrees of diversity in interneuron types. For example, the cerebral cortex is estimated to incorporate

about 50 different types of inhibitory interneurons, based on developmentally driven different expression profiles (Lim et al., 2018). In the striatum, new RNA sequencing data challenges the classic interneurons subtypes, suggesting a gradient in PV expression, as well as a higher degree of discrete interneuron subtypes (Muñoz-Manchado et al., 2018). Following patterns seen in other areas of the brain, those newly identified neurochemical groups might provide novel avenues for preferentially targeting and manipulating MLI subsets. To the extent that those markers correspond to functional classes we can interrogate their differential role within the cerebellar processing.

It is important to properly classify them, as this MLI to MLI interconnectivity sculpts their function as individual cells and as a network. Regarding electrical connectivity, MLIs directly connected through gap junctions belong exclusively to the molecularly defined class MLI1 (Kozareva et al., 2021). Nevertheless, the class of MLI1 shows further diversity in molecular expression, making it unclear if they form a gradient, or should be further subdivided into two more subclasses.

Functionally, electrical coupling between MLI dendrites permits a direct propagation of the depolarizing current called a spikelet, which enhances spiking probability (Hoehne et al., 2020). The electrical coupling also permits the propagation of the AP from the connected neuron. This forms the second hyperpolarizing component of the spikelet and a faster decrease of the excitatory postsynaptic potential (**Figure I11.A-D**). Together those components lead to an increased spike probability in a narrower time window, hence, increased synchrony of firing.

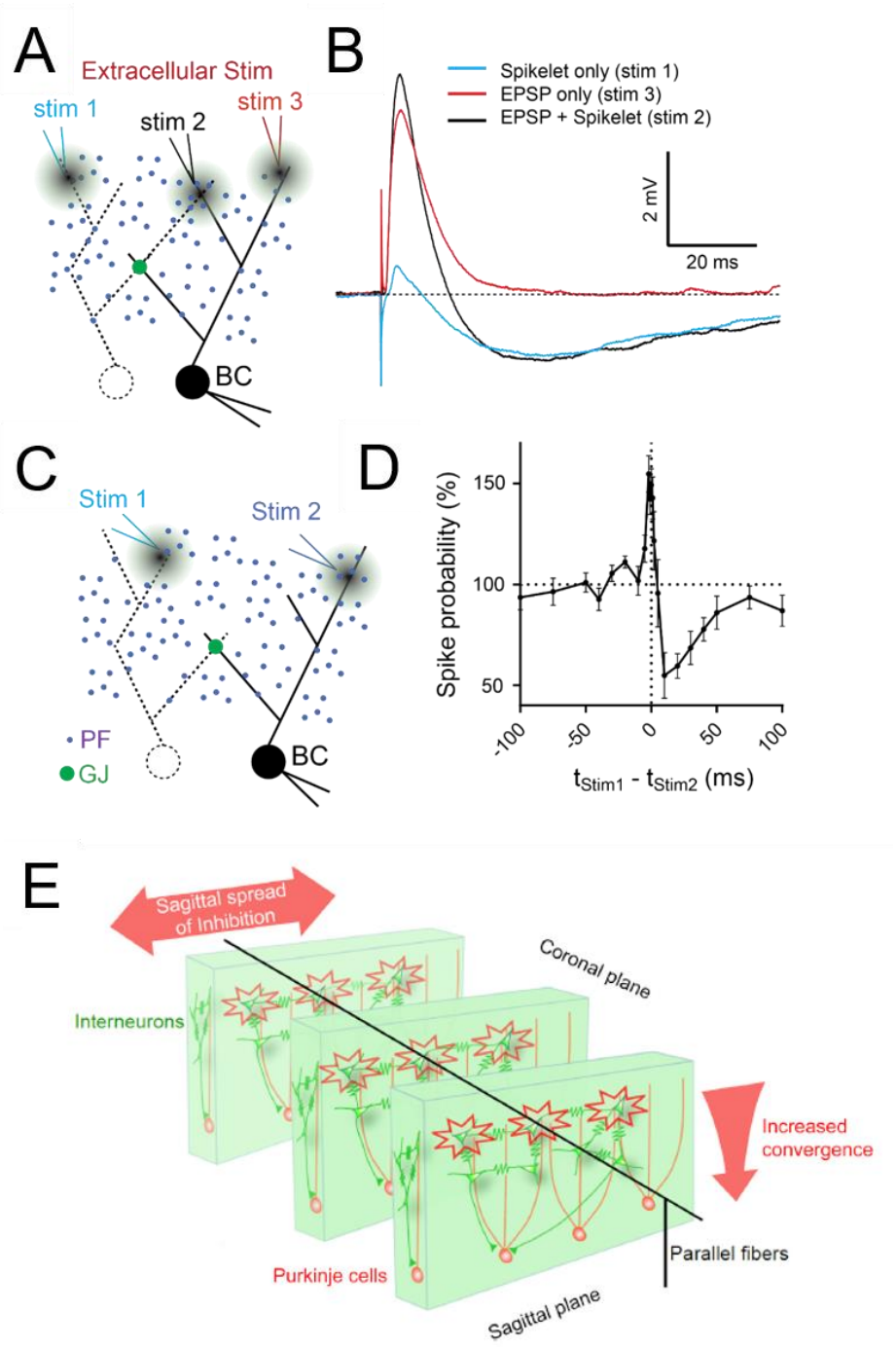

Figure I11. Effects of electrical coupling in MLIs

(A-D) Electrical feed-forward modulation between MLIs and highly-expressed in BCs, narrows the time window of excitatory synaptic integration (**A,B**) and boosts spike probability (**C,D**). Blue dots are a cross-sectional representation of GC axons (parallel fibres, PF) running perpendicular to the planar BC dendrites. Green circle represents a gap junction (GJ). Extracellular stimulation (*stim*) configurations are indicated in A and C. Adapted from Hoehne et al. 2020.

(E) Diagram of the spatial organization of electrical coupling in MLIs (*green*), biased on the sagittal plane and with increasing depth, allowing synchronisation perpendicular to the input received from PFs (*black*) and increased convergence of inhibition to PCs (*red*). From J. Kim et al., 2014.

On a network level, MLIs have a chemical and electrical connectivity preferentially oriented on the parasagittal plane on a distance of ~150 µm, compared to less than 50 µm on the transversal axis (**Figure I11.E**; J. Kim et al., 2014; Rieubland et al., 2014). Their spatial organisation also extends in depth, where deeper BCs have a higher degree of electrical coupling with up to four neighbouring cells, compared to only one in superficial SCs (Alcami & Marty, 2013; Hoehne et al., 2020). Hence, outer MLIs might have a spatially restricted, local inhibitory effect, compared to the broader and stronger influence of inner MLIs.

I2.2 Parallel Fibre input diversity

Electron microscopy analysis of synaptic density and input type revealed early on a different distribution in the depth of the molecular layer (Lemkey-Johnston & Larramendi, 1968b, 1968a). BCs have a higher synaptic density than SCs on both their somas (~15% for BCs compared to ~4.5% for SCs of somatic surface) and dendritic tree (~ 21% for BCs compared to ~10 % for SCs of dendritic surface) (Lemkey-Johnston & Larramendi, 1968a). While the PF synaptic connectivity is the main source of input to MLIs, BCs also have a diversity of inputs from PCs collaterals and other MLIs to a higher extent than do SCs (Lemkey-Johnston & Larramendi, 1968b). By comparison, the upper most SCs receive almost exclusively PF inputs and very few MLI inhibition. This highlights a top down organisation of the lateral inhibition from MLIs.

Interestingly, the PF input might also show a depth dependent heterogeneity (Espinosa & Luo, 2008; Straub et al., 2020; W. Zhang & Linden, 2012). Conserving this laminar arrangement, the PFs at different depths correspond to the location of the somas in the GC layer (birth-timing dependence discussed in section I1.2.4; Espinosa & Luo, 2008; Straub et al., 2020). Those GCs integrate and convey multisensory information from MFs (Chabrol et al., 2015; C.-C. Huang et al., 2013) that is mostly uniform across depth (Markwalter et al., 2019; Shuster et al., 2021). However, inner- and outer-zone GCs are preferentially tuned to high frequency and low-frequency inputs, respectively. This suggests that they might process and further relay the MF information in a depth dependent manner (Straub et al., 2020).

Moreover, the PF diameter and their boutons have a consistently larger diameter in the inner MLI compared to the outer (Eccles et al., 1967; Pichitpornchai et al., 1994; Straub et al., 2020; W. Zhang & Linden, 2012), suggesting faster signal propagation. Indeed, PF fibres

boutons show depth dependent differences in Ca^{2+} dynamics and clearance efficiency, which impacts their diversity in single AP induced Ca^{2+} decay times (W. Zhang & Linden, 2012). As such, PF boutons in the inner molecular layer display faster decay kinetics than outer ones. Also, inner-zone GCs show higher firing thresholds and elicit faster synaptic potentials in PCs, in line with their efficient signal propagation of the inner PFs (Straub et al., 2020). Other evidence suggests that the pattern of the sensorimotor information relayed by PFs is clustered (Wilms & Häusser, 2015) and can be further affected by CF mediated learning induced plasticity (Ekerot & Jörntell, 2001, 2003).

Furthermore, diversity in STP may also impact the PF to MLI information transfer, although it is unclear if this effect is dependent on depth. It has been suggested that synapses with BCs display a higher degree of synaptic depression compared to SCs (Bao et al., 2010), while other data suggests that PF-MLI synapses exhibit four different patterns of plasticity identified to a similar degree in SCs and BCs (Dorgans et al., 2019). This synaptic diversity could be explained by different expression levels of presynaptic proteins that regulate glutamate release, such as Mnc13-3 (Bao et al., 2010) and synapsin II (Dorgans et al., 2019). Another contributing factor can be the location of the synapse on the dendritic tree, because the strength and latency of the SC response can decrease with distance from the soma (Abrahamsson et al., 2012). The PF-MLI synaptic properties and location might therefore play a role in diversifying temporal coding of MLIs (Dorgans et al., 2019), with preferential sustained and narrow inhibitory effects in SCs and BCs, respectively (Bao et al., 2010).

With regards to types of input to MLIs, it is important to mention that chemogenetically suppressing PF activity during sensory stimulation of whiskers greatly reduces MLI response, but does not abolish it completely (Gaffield et al., 2019). This suggests that alternative excitatory mechanisms such as CF spillover (Arlt & Häusser, 2020), may also contribute to their activation during sensorimotor processing. Moreover, MLIs also receive inhibition from PLIs such as CCs and Lugaro cells (Miyazaki et al., 2021; Osorno et al., 2021), however it is currently not well established if they exhibit any gradients or preferential targets.

Overall, the major excitatory input to MLIs is provided by GCs, with some indirect CF activity via spillover and other inhibitory effect via PCs, MLIs and PLIs (Arlt & Häusser, 2020; Dorgans et al., 2019; Lemkey-Johnston & Larramendi, 1968b; Miyazaki et al., 2021; Osorno et al., 2021; Szapiro & Barbour, 2007). Of those, GCs might have diverse intrinsic properties with which they integrate MF information and further relay it to MLIs and PCs, in a depth dependent manner (Straub et al., 2020; W. Zhang & Linden, 2012). This laminar effect might

further be inherited by MLI and contribute to how they process the sensorimotor information received (Bao et al., 2010).

I2.3 Molecular layer interneurons representations during behaviour

Despite their physiological and input differences, it is not well understood how MLI subtypes modulate the representation of sensory contexts. For example, MLIs elicit coherent sensory responses to whisker air puffs in anaesthetised mice (Chu et al., 2012). Those responses have a higher prevalence in BCs of which all cells recorded responded, compared to two thirds of SCs. Also, the excitatory postsynaptic currents (EPSCs) evoked in MLIs are increasingly larger, with faster onset and shorter with depth (**Figure I12**). This suggests a stronger and more temporally precise sensory representation in BCs compared to SCs. This might be partially due to a high degree of electrical coupling that can produce a fast and strong synchronized and BC output in response to coincident or sequential PF input (discussed in I2.1, Alcami, 2018; Hoehne et al., 2020). Although the role of MLI electrical coupling has not been tested *in vivo* yet, for GoCs, electrical coupling was shown to be essential in controlling temporal precision and degree of correlated activity in both spontaneous and sensory-evoked responses via air-puffs to the whiskers (van Welie et al., 2016). Moreover, recent work showed that Golgi cells exhibit clustered activity related to the sensory context which is dependent on electrical coupling (Gurnani & Silver, 2021).

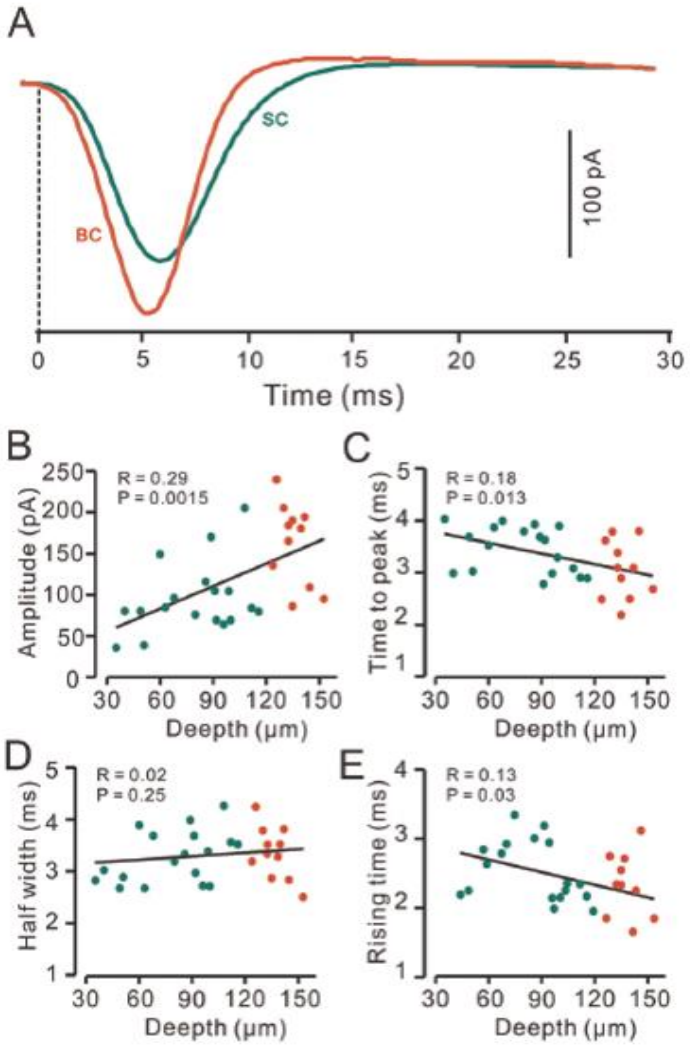

Figure I12. Depth-dependent differences in air puff stimulation-evoked EPSCs

(A) Representative current traces in a basket-type MLI (BC; *red*) and stellate-type MLI (SC; *green*) aligned to the onset of their responses (time point 0).
(B-E) Cross-correlation plots showing relationship between depth of soma and EPSC **(B)** amplitude, **(C)** time-to-peak, **(D)** half-width **(E)** rise time (10-90%), with linear regression line (R, *black line*). SCs represented by green dots and BCs by red dots. From Chu et al., 2012.

MLIs ensembles show highly coherent activity during behaviour, such as licking or whisking (Astorga et al., 2017; Chen et al., 2017; Gaffield & Christie, 2017). In Crus II, MLI activity encodes lick rate (Astorga et al., 2017; Gaffield et al., 2019). Interestingly, the correlation in SCs activity decreases within 120 microns distance on the parasagittal plane, while being maintained for the same distance in BCs (Astorga et al., 2017). This suggests that SCs and BCs might employ a different response pattern during behaviour. As such, the orientation of coherent activity of SCs is perpendicular to their dendritic tree, consistent with PF mediated synchronization through chemical synaptic input coming from GCs. In contrast,

BCs are preferentially electrically coupled in addition to chemical synapses, which generate transversal synchronized recruitment of this population through the electrical transmission of spikelets (Hoehne et al., 2020; J. Kim et al., 2014). Although further investigation would be needed to test this causality *in vivo*.

Also, the MLI activity can vary between different types of licking behaviour, by expressing or not delays between exploratory licking (to search for the presence of water) and consuming water, respectively (Astorga et al., 2017). This suggests that MLI activity during behaviour can be mediated by input and vary based on motivational state. The MLI activity can also differ depending on the type of behaviour. The behaviourally correlated activity seen during licking was not seen during bruxing, in which case it is not temporally correlated with oromotor activity and does not show a spatial organization (Astorga et al., 2017).

Moreover, MLIs have a functional role in the behaviour they encode. For example, suppressing MLI activity leads to disruption of licking (Gaffield & Christie, 2017). Also optogenetic activation of MLIs can induce eyelid closure and orofacial movements (Heiney, Kim, et al., 2014), highlighting their role in motor control. This role also extends to a broad range of cerebellar function such as associative learning or even social behaviour (Badura et al., 2018; Ma et al., 2020; Rowan et al., 2018; ten Brinke et al., 2015). As seen for the VOR, MLI activity can mediate CF dependent learning (see section I1.3.2, Rowan et al., 2018). It has also been shown that associative learning can shape MLI population activity (Bonnan et al., 2023; Ma et al., 2020), and that this acquired pattern of MLI activity is important for task performance during odour discrimination (Ma et al., 2020). Contrary, their inhibition does not alter fear conditioning in a transgenic mouse with deficient MLI to PC signalling (Marshall-Phelps et al., 2020), suggesting a minimal role of MLIs, or a compensatory mechanism during long-lasting changes during this type of task. Nevertheless, their normal function is significant for the normal development of a broad range of cognitive and social functions (Badura et al., 2018). As a result, suppression of MLI activity in juvenile mice causes persistent cognitive and social impairments, which vary dependent on the cerebellar lobule targeted. The behaviours impacted include associative and reversal learning (lobule VI and Crus I), novelty-seeking (lobule VII) and social preference (Crus I-II).

On the whole, MLIs are an integral part of the cerebellar circuitry, that can encode and drive behaviour (Badura et al., 2018; Bonnan et al., 2023; Gaffield et al., 2019; Heiney, Kim, et al., 2014; Rowan et al., 2018). Some evidence suggests that MLI subtypes might encode

sensory and motor responses differently (Astorga et al., 2017; Chu et al., 2012). However, to what extent those different patterns underlie heterogeneous roles remains yet to be explored.

I2.4 The influence of molecular layer interneurons on Purkinje cell activity

The propagation of excitatory signals throughout the neural circuit is known to be modulated by inhibition from GABAergic interneurons, creating an important temporal balance for information processing (Duguid et al., 2012; Isaacson & Scanziani, 2011). In the cerebellum the impact that MLIs have on modulating behaviour (described in the previous section I2.3), mainly predicates on the inhibition exercised upon PCs (Han et al., 2018; Häusser & Clark, 1997; Mittmann et al., 2005). Common to brain circuitries, interneurons inhibit principal neurons upon receiving collaterals from excitatory projections that target those principal neurons, a connectivity motif called feed-forward inhibition (FFI) (Blot et al., 2016; Mittmann et al., 2005; Pouille & Scanziani, 2001; Tremblay et al., 2016). It was firstly shown in the hippocampus that FFI is essential for the temporal precision of pyramidal cells spikes, by only allowing a brief temporal summation (under 2 milliseconds) of its excitatory input (Pouille & Scanziani, 2001). This is also true for the cerebellar cortex, where between PF → PC excitation, the mechanism of action of MLIs is mainly through FFI in a PF → MLI → PC configuration. As GCs may have dense representations of sensorimotor contexts (Giovannucci et al., 2017), this precisely-timed FFI might help disentangle their input, by narrowing the time window in which PFs inputs are integrated by PCs (Mittmann et al., 2005). This further promotes synchrony in PCs activity within milliseconds precision (Han et al., 2018; Wise et al., 2010), enabling precisely-timed PCs responses tuned to detailed features of the sensory context (De Solages et al., 2008; De Zeeuw & Romano, 2022; Lindeman et al., 2021; Person & Raman, 2012). Computational models also support that FFI provides an effective threshold to the network that helps PCs to decorrelate the GC activity patterns (Cayco-Gajic et al., 2017; Cayco-Gajic & Silver, 2019), as well as a negative weight that is crucial for PCs learned firing pauses (Barri et al., 2022).

The failure to provide this well calibrated PC output is linked to various disorders such as ataxia or autism (De Zeeuw et al., 2011; Stoodley et al., 2017; Tsai et al., 2012). Outnumbering PCs at a ratio of 1:10 (Korbo et al., 1993), the input of two to nine MLIs converges onto one PCs to shape their firing rate on a millisecond scale (Arlt & Häusser, 2020; Blot et al., 2016; Häusser & Clark, 1997; J. Kim et al., 2014). The accurate control of PC activity

by MLI inhibition was reported to be important during various cerebellar dependent behaviours and learning tasks (Chu et al., 2011; Heiney, Kim, et al., 2014; Jelitai et al., 2016; Rowan et al., 2018; ten Brinke et al., 2015). Experimentally, inhibiting PCs by a strong activation of lobules V-VI MLIs can induce eye closure and orofacial movements (Heiney, Kim, et al., 2014). This MLI activity induced inhibition of the PCs leads to the indirect DCN disinhibition, generating uncontrolled movements.

In contrast, silencing MLI activity results in an increased rate and regularity of PC simple spikes that disrupts locomotion, probably by a failure to relate information about movement changes and to gate against excessive PF input integration (Jelitai et al., 2016). Moreover, during whisker stimulation MLIs spiking precedes PCs evoked inhibitory postsynaptic potentials by ~1 ms (Chu et al., 2012). The selective impairment of MLI inhibitory synaptic input into PCs through $GABA_A$ receptors agonists, abolishes the sensory-evoked PCs pauses of simple spikes (Chu et al., 2011). Also, transgenic mice with mutated $GABA_A$ receptors at MLIs to PCs synapses have impaired associative learning in eyeblink conditioning (ten Brinke et al., 2015). MLIs also act to control CF mediated plasticity in order to provide the accurate adaptation during VOR (Rowan et al., 2018). Under normal circumstances of motor learning, during practiced behaviour, MLIs act to supress PF enhanced CF singling in PCs (Gaffield et al., 2018). In this respect, MLIs can act as a gate keeper to provide appropriate inhibition during learning-related plasticity.

All those effects are induced by the influence of MLIs on PCs, but, within their diverse population, their mechanism of action might imply diverse strategies with spatial and temporal heterogeneities (Arlt & Häusser, 2020; Chu et al., 2012; Hoehne et al., 2020; J. Kim et al., 2014). One main distinction of interneurons is their target location on the principal neuron, either somatic or dendritic, which dictates the strength of the inhibition (Pouille & Scanziani, 2001). For hippocampal pyramidal cells it has been shown that a higher degree of excitation can overcome concomitant dendritic inhibition, but not somatic inhibition. In the cerebellar cortex, deep BCs specifically show ephaptic coupling at the axon initial segment of the PC which is almost a millisecond faster than a chemical synapse (Blot & Barbour, 2014). This almost instantaneous inhibition voltage change of the local extracellular space can allow GC input to indirectly produce a net inhibitory effect onto the PCs and promote their synchronous firing (Han et al., 2018). Meanwhile, SCs show nonlinear integrations that may act as temporal filters (Abrahamsson et al., 2012), similar to dendritic-targeting inhibitory interneurons in the hippocampus (Schulz et al., 2018).

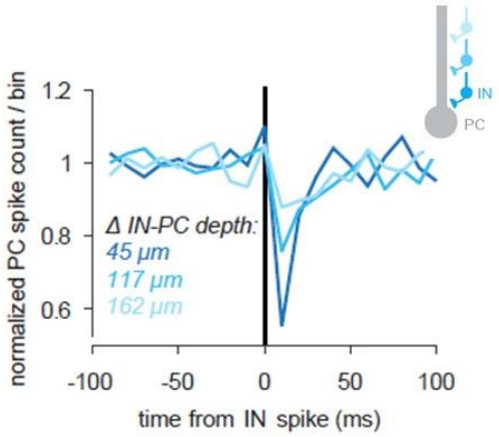

Figure I13. Depth-dependent strength of inhibition between MLI – PC pairs

Baseline-normalized spike counts/bin for 3 example PCs paired with interneuron (IN) inhibition from deep (*dark blue*), intermediate (*blue*) and superficial (*light blue*) ML and aligned to the IN spike (time point 0, *black line*). Depths indicate intersomatic transverse distance of the IN-PC pairs. From Arlt & Häusser, 2020.

It is important to mention that the segregation into SCs and BCs is not a clear cut, and their morphological and electrophysiological properties are more likely provided within a spatial and temporal gradient (Rieubland et al., 2014; W. X. Wang & Lefebvre, 2022). Indeed, MLIs sculpt the activity of PCs with a gradual increase in strength and temporal precision with increasing depth (**Figure I13**; Arlt & Häusser, 2020). This effect is not surprising considering the aforementioned depth dependence in intrinsic properties of MLIs, as well as the PF input which might have different effects on their temporal recruitment (see sections I2.1 and I2.2, Chu et al., 2012; Hoehne et al., 2020; Straub et al., 2020; W. Zhang & Linden, 2012).

Another important connectivity pattern that dictates the temporal integration of PF input and spread of inhibition onto PCs is provided by the electrical coupling of MLIs (Alcami, 2018; Hoehne et al., 2020; Rieubland et al., 2014). Electrical connectivity can accelerate PF input integration and improve MLI recruitment (Alcami, 2018). The electrically coupled MLIs are present throughout the depth of the molecular layer (Kozareva et al., 2021), but with an increasingly higher degree with depth (J. Kim et al., 2014). Furthermore, electrical coupling is preferentially organized on the parasagittal plane (J. Kim et al., 2014; Rieubland et al., 2014). The axons of MLIs, in particular BCs, also run on the sagittal plane for over a hundred microns to provide lateral inhibition to far away PCs (Palay & Chan-Palay, 1974). This planar orientation, permits discontinuous inhibition of PCs along the transversal PF input and reinforces the sagittal organisation of cerebellar information processing into microzones, to

which MLIs largely abide (segregation into microzones discussed in I1.2.3, Ekerot & Jörntell, 2003; W. Gao et al., 2006; Valera et al., 2016).

Importantly, PCs to MLIs feedback inhibition (Halverson et al., 2022) as well as MLI to MLI inhibition (Kondo & Marty, 1998b), might also have an important regulatory role in motor coordination, via a resulting disinhibitory effect of the respective PCs. Evidence from the cortical VIP interneurons suggests that their indirect disinhibition of the pyramidal cells is a crucial circuitry element for learning (Karnani et al., 2016; Krabbe et al., 2019; Tremblay et al., 2016; Turi et al., 2019).

Overall, MLIs are key elements of the cerebellar cortex circuitry that gate and sculpt PCs dynamics to regulate the proper integration of sensorimotor information and generate appropriate behaviours.

II3. Objectives

The cerebellum integrates sensorimotor information with high temporal precision, needed to accurately tune behaviour. With consideration to the anatomo-functional arrangement of the cerebellar cortex, it has three axes of heterogeneity: 1) medio-laterally into microzones as functional units of circuitry (Apps et al., 2018), 2) rostro-caudally axis into lobules receiving different input patterns and 3) a depth axis of laminar cellular transcriptional and functional diversity (Arlt & Häusser, 2020; Bao et al., 2010; Hoehne et al., 2020; Kozareva et al., 2021; Straub et al., 2020). MLIs function within this arrangement to process sensorimotor information and directly sculpt the activity of the sole output of the cerebellar cortex, the PC, in a depth dependent manner (Arlt & Häusser, 2020).

With respect to the laminar organisation, MLIs may receive a depth-dependent sensorimotor input from GCs, as well as exhibit a depth-dependent intrinsic diversity primarily through electrical coupling and transcriptional clusters (Alcami, 2018; Hoehne et al., 2020; Kozareva et al., 2021). Nevertheless, little is known about their *in vivo* laminar representation of sensorimotor variables during behaviour. Furthermore, MLIs encode both sensory (Chu et al., 2012) and motor features of whisker kinematics (Chen et al., 2017). However, how sensory and motor variables are balanced in the MLI representations is less understood.

Consequently, this project explores:

1. the depth-dependent diversity of MLI representations of sensorimotor variables during the behavioural context of whisking

2. how the MLI representation changes with sustained sensory input; also to what extent MLIs representations differ between sensory-evoked and self-initiated whisking, where the latter lacks any external sensory input.

II. Methods

II1. Animals

All animal experimental procedures were conducted in compliance with French and European regulations on care and protection of laboratory animals (EC Directive 2010/63, French Law 2013-118, February 6th, 2013), and approved by the Ethics Committee for animal experimentation at the Pasteur Institute (CETEA) and the Institute of Experimental Medicine Protection of Research Subjects Committee. Mice were housed in the Pasteur Institute animal facilities accredited by the French Ministry of Agriculture for performing experiments on live rodents. After weaning age (PND21), mice were housed with 1-5 littermates per cage and kept on an inverted 12/12h light/dark cycle, standard temperature of 21-22 °C, with food and water ad libitum. A total of 24 adult male and female mice were used for this study.

For *in vivo* imaging experiments 5 mice resulting from the cross of Penk-Cre (courtesy of our collaborator Jason Christie) with a tdTomato reporter line (Ai14, Jackson Laboratory strain 007914) and 7 Gabra6$^{tm2(cre)Wwis}$ (Jackson Laboratory strain 3047798) mice were used for in recordings of MLIs and GCs activity, respectively. For MLI *in vivo* imaging experiments, 2 wild-type (C57BL/6J, Jackson Laboratory strain 000664) mice were added for experiments where distinction of Penk-cre gene was not necessary. For *in vitro* experiments, 7 Penk-Cre x tdTomato mice were used. For Neuropixels recordings, 3 wild-type mice (C57BL/6J) were used.

II2. Cranial window surgery and viral injection

For *in vivo* imaging experiments, mice aged between 8-12 weeks underwent stereotaxic surgery under sterile conditions. They were given Buprenorphine (Buprecare, 0.05 mg/kg subcutaneously) 30 minutes in advance and then deeply anesthetized with isoflurane (4% for induction, 1–2% for maintenance). The skull was exposed and the periosteum removed by gently drilling on low speed across the area. A 3.5 mm circular craniotomy was performed above the right hemispheric cerebellum, leaving the dura intact and exposing lobule Crus I and part of Simplex and Crus II (6.5 mm anterior and 2.5 mm lateral relative to bregma). To avoid the exposed dura drying out for the duration of the surgery, dental gelfoam sponges (Spongostan, Ethicon) submerged in sterile physiological serum solution (Physiodose; Laboratoires Gilbert) were placed around the margins of the craniotomy.

For viral injections borosilicate glass pipettes (World Precision Instruments, 1B100F-4, 1/0.58 mm OD/ID) were bevelled to 30 degrees with a ~ 10 mm tip opening. We took advantage of the synapsin 1 gene promoter of the AAV1-syn-GCaMP8f-WPRE (virus titer: 3 x 10^{13} GC/ml; virus batch from Adam Hantman laboratory, Janelia Research Campus) to bias our expression of the Ca^{2+} indicator GcaMP8f in MLIs and avoid detectable PC expression and signal contamination (Kuhn et al., 2012). The virus was diluted 1:10 in a NaCl 0,9% sterile solution and then delivered (Nanoject III, Harvard Apparatus) in 3 to 5 injection sites within the exposed cerebellar Crus I at a volume of 100 nl per injection site, with a speed of 2nl/sec and a depth of -0.2 µm from the brain surface. Before slowly removing the injection pipette, 3 minutes post injection were allowed each time for the virus to fully diffuse.

To specifically express the Ca^{2+} indicator GcaMP8f in GCs, we used the Gabra6tm2(cre)Wwis mouse line which expresses Cre recombinase exclusively in GCs (Aller et al., 2003). AAV-290-DJ-CAG-FLEX-jGCaMP8f (virus titer: 5 x 10^{13} GC/ml; virus batch from Halina Staniszewska Goraczniak laboratory, Princeton University) was delivered using a similar injection protocol, but at a depth of -0.5 µm from the brain surface.

A window composed of a glass coverslip (Multichannel Systems, CS-3.5R Small round cover glass, #1 thickness) glued (Norland Optical Adhesive 71) to a stainless steel ring (Ziggy's Tubes and Wires, 316 S/S Hypo Tube 9R GA. 1470/.1490"OD x .1150/.1200"ID x 0.0197" long; cut and deburred, facing upward) was carefully placed over the craniotomy and fixed with Vetbond (3M, World Precision Instruments) to the edges of the skull. A one-piece titanium headplate (Pasteur Institute Technology and Service Unit) was attached and secured around the craniotomy to the mouse's skull with dental cement (Paladur, Dentalzon). Anti-inflamatory Metacam (1 mg/kg) was administered to the neck area subcutaneously at the end of the surgery. Injected mice were closely monitored for 3-days post-surgery and kept for 2 weeks to allow recovery and transgene expression.

II3. *In vivo* optical imaging

Two-photon calcium imaging was performed using a custom-built two-photon microscope (2PLSM, Ultima IV, Bruker). A laser beam tuned at an excitation wavelength of 920 nm was generated by a pulsed Ti:Sapphire laser (MaiTai eHP DeepSee, Spectra- Physics). Power control was obtained via a Pockels cell (ConOptics, Model 350-80, Controller 320RM). The region exposed by the cranial window was scanned in resonant mode using a 5 mm galvanometer and an 8-kHz resonant scan mirror (Cambridge Technologies, CRS 8kHz),

through a low power objective (Nikon 16X, 0.8 NA water) immersed in ultrasound gel (Sonigel, Mettler Electronics). To minimize tissue heating and photodamage (Picot et al., 2018; Schmidt & Oheim, 2020), the laser power measured at the front of the objective did not exceed 60 mW, and was kept typically at 45 to 55 mW, for outer and inner molecular layer, respectively. The emission light was split into red and green channels using a filter cube (BRUKER C-138730) comprising of a 575nm dichroic mirror (CHROMA, 575dcxr, lot 226893), and two bandpass filter for green (CHROMA HQ525/70m-2p; lot 225777) and red (CHROMA HQ607/45m-2p; lot 224958) emission, then detected using GaAsP photomultiplier tubes (H7422PA-40 SEL, Hamamatsu) and amplified using a high-speed current amplifier (Bruker, U-PA 518564). The resulting signal was recorded using a high speed acquisition card (General Standard, 66-14-HSAI4).

To enhance capturing the fast dynamics of the GCaMP8f sensor (Y. Zhang et al., 2023) the image size (frame rate of 30fps in full image mode at 512x512 px image resolution) was reduced on the resonant scanning axis, which allowed a high speed image acquisition frequency of 100 Hz. Therefore, time-series of a 495 x 140 µm FOVs with a pixel size of 0.952 x 0.952 µm / pixel were recorded using Prairie View software (Bruker) at 100 Hz. For the small PFs buttons a zoom of 4-6 was used to record at a higher image resolution. Regions within the cerebellar lobule Crus I were identified based on observing a general cells response within the area upon delivering air puffs to the whiskers, as described in the next section. FOVs were selected across those regions using the blood vessel landmark to identify approximate location within the lobule and avoid resampling neurons. Two to four FOV at each depth were imaged per mouse. Anatomical boundaries were used to identify and delimitate different depths within the molecular layer. Outer MLIs and PFs were imaged within the focal plane immediately below the pial surface, where a full-filed plane of the molecular layer was visible (16 ± 1.9 µm below pia, n = 4 FOVs). Within consistent x-y locations, inner MLIs and PFs were identified based on the proximity to the Purkinje cell layer, where basket terminals or PFs surrounding PCs somas, respectively, were forming web-like structures (85 ± 11.2 µm below pia, n = 4 FOVs). For some experiments a middle depth point between the outer and inner region of a given x-y location (46 ± 6.3 µm below pia, n = 4 FOVs) was used to define middle layer MLIs or PFs, respectively.

II4. Behavioural procedure for *in vivo* imaging

To enable imaging of MLIs and PFs responses to tactile stimulation, mice were head-fixed under the two-photon microscope using two custom headplate holder bars (Pasteur Institute Technology and Service Unit) and rested in a custom transparent plastic tube (10 cm long, 5 cm inner diameter) to reduce confounding influence of body movements during experiments. Mice were habituated to the set-up and head fixation in at least 3 sessions of at approximately 15 minutes each, the days preceding the start of the imaging experiments.

Behavioural movies were acquired using two Basler Cameras (ace acA1440-220um USB3 Monochrome, 1440 px x 1080 px resolution) to image the mouse head and whiskers and other body movements, respectively. A python-based custom written camera driver was used to select optimized image parameters and record single frame timestamps with microsecond precision. The whisker camera was positioned in the front of the mouse and an ROI of approximately 500x300 pixels was defined from the full frame and imaged at 250 Hz, with a 500 microsecond exposure time to capture whisker fast movement and avoid blur. The second body camera, with an ROI of approximately 850x300 pixels was focused on the mouse's limbs from below through a mirror (100 Hz imaging rate, 1000 microseconds exposure time) and used for qualitative inspection of big body movements. Illumination was provided by an infrared lamp (CMVision IR30 WideAngle IR Illuminator) at 850 nm.

Air puffs were produced by a Picospritzer III (Parker Hannifin Corporation) and delivered to the right Whiskers (ipsilateral to the imaging brain hemisphere) via a nozzle (1 mm diameter opening). A first set of experiments was done by directing the nozzle from the side at the center of the whisker pad ~1.5 cm away and delivering a brief strong air puff (10 ms, 20 psi), as previously described (Brown & Raman, 2018). To allow longer sensory stimulation while preventing aversive eye closure, a second set of either brief (10 ms) or long (1000 ms) air puffs (5 psi) were delivered from the front, perpendicular to the whiskers (2 cm frontal and 1.5 cm lateral to the centre of the whisker pad). Control air puff directed away from the mouse were also given, as well as no-stimulation baseline trials for recording of spontaneous whisk.

The timing of the behavioural imaging, calcium imaging time series and whisker air puff delivery was controlled by triggering TTL pulses with Neuromatics (IGOR Pro, WaveMetrics). The delay between the TTL signal and the air-puff arrival at nozzle was measured and accounted for in further behavioural analysis. at One experiment consisted of interleaved sets of baseline, short, and long air puff stimulation described above, of 30 trials each, in a randomized order generated and stored by Neuromatics. Individual trials lasted either

6 or 10 seconds with a 2 second inter-trial interval. The total experimental time did not exceed 120 min per mouse within a given day.

II5. Imaging data processing

To correct for spatial motion in the FOV, the time-series images of the Ca^{2+} activity of neurons expressing GCaMP8f were firstly registered using the Suite2p rigid registration algorithm to the reference image of the 20 most correlated frames (Pachitariu et al., 2016). For the experiments involving Penk-cre mice co-expressing tdTomato in Penk-positive cells the movement correction was done using the non-functional red channel (n = 5 mice). Both registered and raw t-series were inspected for general recording stability and excluded from further analysis if visible movement was present. To maximize the number of ROIs detected in highly synchronized MLI population (Gaffield & Christie, 2017), a custom graph based segmentation algorithm was further applied on the registered single plane images to extract ROIs of neuronal somas, as well as PF axonal buttons. The segmentation algorithm generates a network between locally highly correlated pixels and employs the Louvain algorithm to find individual cells as communities of the network. The ROIs created by the algorithm were manually curated. Where available, the traces of the non-functional red channel (corresponding to tdTomato expression) extracted from the same ROIs selected via the functional green channel (corresponding to GCaMP8f expression) were also visually inspected for any residual movement artefacts. Only ROIs delimitating buttons or single somas, respectively, fully contained within the FOV were selected for further analysis. The ΔF/F0 fluorescence intensity was calculated using a baseline fluorescence period (100 frames) immediately prior to stimulation, or an identified spontaneous whisking event for non-stimulated experiments. Average traces across trials centred around either stimulation points or spontaneous whisking events, were stored for each ROI. Further, ROIs from each recording session were defined as responsive based on a Peak signal across 50 milliseconds of the trial-averaged ΔF/F0 trace exceeding at least two times the standard deviation of the baseline trace one second before stimulation, or onset of the spontaneous whisking event, respectively (SNR = Peak $_{\Delta F/F}$ / SD $_{\text{Baseline } \Delta F/F}$). The Ca^{2+} traces of responsive cells were further fitted to Becker's multi-exponential function with 3 exponents, one rise and two decay exponents $y = \left(1 - e^{\frac{-(X-X_0)}{TR1}}\right)^N \left(A1e^{\frac{-(X-X_0)}{TD1}} + A2e^{\frac{-(X-X_0)}{TD2}}\right)$ (IGOR Pro, WaveMetrics). Time-to-peak, rise time (10 to 90 % of the peak), decay time (time from peak to 50 % of maximum), onset time (to 10

% above baseline) and FWHM (time from 50 % rise to 50 % decay) were determined for each cell based on the curve fit.

II6. Behavioural data processing

To extract whisker kinematics, we used a custom written python-based whisker detection and tracking software. The angle of deflection of left and right whisker arrays was calculated for each time point, within a radial region around the centre of the whisker pad that was manually selected. For stimulated experiments, sessions were then visually inspected and only trials in which the mouse was in a quiet non-whisking wakefulness state at least 500 milliseconds before delivering the air puff, were selected for further analysis. A few rare cases in which eye closure was observed as a response to the air puff were also excluded. Grooming epochs involving ample body movements were also excluded. For spontaneous whisking a custom-written analysis pipeline was used to identify whisking epochs, defined as an angle of deflection of at least 10° and a one-second-long baseline immediately preceding the whisking lower than four standard deviations. The angle of deflection during both stimulated and spontaneous whisking epochs was normalized to the relative mean angle of the whisker one second preceding the air puff or onset of spontaneous whisking, respectively, for each given trial. For stimulated experiments trial-averaged whisker responses were fitted as for the Ca^{2+} traces using the Becker's multi-exponential function described in the previous section.

II7. Surgery for Neuropixels recordings

For *in vivo* electrophysiology experiments, mice underwent a first stereotaxic surgery under sterile conditions for headbar and recording chamber implantation. They were given Buprenorphine (Buprecare, 0.05 mg/kg subcutaneously) and injectable Meloxicam (anti-inflammatory, 1mg/kg) 30 minutes in advance and then deeply anesthetized with isoflurane (4% for induction, 1–2% for maintenance). Injections of Xylocaine (5mg/kg) ensured local analgesia before incisions were made. The skull was exposed, thoroughly cleaned and dried. Custom-made titanium headbars and 3.5 mm diameter recording chambers cut from plastic pipettes were secured to the skull using Metabond. Recording chambers were secured over the location of Crus1 following stereotaxic coordinates (-3,2 mm lateral, -6,25 mm posterior from bregma, Brown & Raman 2018) and visual landmarks. Mice were provided with DietGel Recovery Purified Dietary Supplement (Clear H2O) filled with Meloxicam oral for analgesia

following the procedure. Mice were observed for signs of pain and infection for 3 days following the procedure, and recovered for at least 2 weeks prior to recording. On the morning of the first recording day, animals underwent a second surgery to open a craniotomy over the cerebellum. They were subcutaneously injected with Buprenorphine (0.05 mg/kg) 30 minutes prior to the procedure and anesthetized with isoflurane as during the first surgery. Dental cement and skull within the recording chamber were drilled away to create a 3mm craniotomy exposing Crus1. The exposed tissue was cleaned and preserved with artificial cerebral spinal fluid (aCSF), and Kwikcast (World Precision Instruments) was placed over the craniotomy and only removed prior to probe insertion later in the day.

II8. Neuropixels recordings

We used Neuropixels 1.0 high-density silicon probes from Imec (Jun et al., 2017) with the SpikeGLX 3.0 software to record from the cerebellum on 384 channels at 30 kHz sampling rate (AP channel, filtered between 0.3 and 10 kHz before on-chip digitalization). A silver wire placed acutely in aCSF in the recording chamber was used as reference. The probe was coated with DiI in 70% ethanol prior to each recording session, for staining of the probe track in the tissue. A PatchStar micromanipulator (Scientifica) was used to position the probe using vessel landmarks over Crus I while viewing with a Dino-lite USB microscope, and to insert it 2 mm into the tissue over several minutes. The probe was left in place for about 10 min prior to the beginning of the recording.

The behavioural procedure was very similar to the one described above for 2-photon imaging, although it was performed on a different setup (mouse habituated to sit under head fixation in a plastic tube, imaging of whiskers and body/paws with Basler cameras, air puffs delivered to whisker pad or whiskers by a Picospritzer). Also similarly, Neuromatic IgorPro software was used to trigger stimuli and video acquisition with TTL pulses. Neuropixels recording was continuous throughout each 2h session. An additional TTL pulse was generated by Neuromatic and sent to the Neuropixels acquisition system (SpikeGLX software) at the onset of every trial for synchronization of spiking and behavioural data during later analysis.

II9. Neuropixels data processing

The CatGT tool (from SpikeGLX's author Bill Karsh) was used to concatenate Neuropixels files from a single session if needed, to detect TTL syncing pulses and to de-noise by subtracting the average of all channels from all signals. MATLAB-based Kilosort2 was then used as an automatic spike sorting algorithm, using default parameters excepted from the sampling rate (small difference from 30kHz detected for each headstage using Bill Karsh's calibration procedure) and probe layout ('Neuropixels 3B1 staggered'). The python-based Phy GUI was used for manual single unit curation of the outcome of Kilosort2. Single unit activity was identified as displaying a refractory period after each spike, visible in the autocorrelogram as a through for about 2 ms around the 0 bin (1 ms in the case of fast firing Mossy Fibres). Spike activity that did not meet these criteria was registered as multi-unit. Units were merged if waveforms looked similar, autocorrelograms (ACGs) looked similar, and crosscorrelograms (CCGs) had noticeable refractory periods and were similar to the ACGs. Units that were located in the molecular layer, ie in the vicinity of clearly identified Complex Spikes, but that displayed higher firing rates than typical Complex Spikes, were classified as MLIs. Finally, custom Matlab scripts built upon code developed by the Cortex lab at UCL (https://github.com/cortex-lab, 'spikes' repository) were used to compute PSTHs of responses to air puffs for all the single units. Stimulus timing was computed based on the TTL syncing pulses generated by Neuromatic at the onset of each trial. Time to the peak firing rate and to 10% of the peak firing rate following air puff stimuli were extracted from the PSTHs and compared to the times of peak and 10%-of-peak whisker angle deflections.

II10. Cerebellar slice preparation

Acute sagittal slices (200 µm) of cerebellar hemispheres were prepared from adult Penk-Cre X tdTomato mice, aged between 1 and 5 months. Following transcardial perfusion with an ice-cold solution containing (in mM): 2.5 KCl, 0.5 CaCl2, 4 MgCl2, 1.25 NaH2PO4, 24 NaHCO3, 25 glucose, 230 sucrose, and 0.5 ascorbic acid, the brain was removed and placed in the same solution. Slices were cut from the dissected cerebellar hemispheres using a vibratome (Leica VT1200S), and incubated at room temperature for 30 min in a solution containing (in mM): 85 NaCl, 2.5 KCl, 0.5 CaCl2, 4 MgCl2, 1.25 NaH2PO4, 24 NaHCO3, 25 glucose, 75 sucrose and 0.5 ascorbic acid. Slices were then transferred to an external recording solution containing (in mM): 125 NaCl, 2.5 KCl, 1.5 CaCl2, 1.5 MgCl2, 1.25 NaH2PO4, 24 NaHCO3,

25 glucose and 0.5 ascorbic acid, and maintained at room temperature for up to 6 hr. All solutions were bubbled with 95% O2 and 5% CO2.

II11. Two-photon imaging *in vitro*

The brain slices were placed in the recording chamber and perfused with the recording solution. The Crus I region was identified with a 4x objective lens (Olympus UplanFI 4x, 0.13 NA). MLIs were then identified using infrared Dodt-gradient contrast and a QlClick digital CCD camera (QImaging, Surrey, BC, Canada) mounted on an Ultima multiphoton microscopy system (Bruker Nano Surfaces Division, Middleton, WI, USA) that was mounted on an Olympus BX61W1 microscope, equipped with a water-immersion objective (Olympus 60x, 1.1 NA). Two-photon excitation was performed with a Ti-sapphire laser (Spectraphysics). *Penk1*/tdTomato-expressing neurons were identified visually with two-photon excitation at 920 nm. Infrared Dodt-gradiend contrast was then used to position the recording pipette and to perform whole-cell patch-clamp on both Penk-positive and Penk-negative MLIs. For patch-clamping, thick-walled glass patch electrodes with a tip resistance of 5-8 MΩ were fire-polished and filled with an internal solution containing (in mM): 115 $KMeSO_3$, 40 HEPES, 1 EGTA, 6 NaOH, 4.5 $MgCl_2$, 0.49 $CaCl_2$, 0.3 NaGTP, 4 NaATP (adjusted to 300-310 mOsm, pH = 7.3, referred to a K^+-based internal solution). For morphological characterization, Alexa 488 (2 mM) was added to the internal solution and dialyzed via the patch electrode. Cells were perfused for at least 15 min with the internal solution to ensure proper loading of the dye into the dendritic and axonal arborization. Two-photon excitation of Alexa 488 was then performed at 810 nm and a Z-stack of images was acquired to characterize the neuronal morphology. Fluorescence was detected using both proximal and substage gallium arsenide phosphide (GaAsP) photomultiplier tubes (H10770PA-40 MOD, Hamamatsu). The signal was separated using a filter cube (BRUKER C-120413) comprising of a 575nm dichroic mirror (CHROMA, 575dcxr), and two bandpass filter for green and red emission, CHROMA HQ525/70m-2p and CHROMA HQ607/45m-2p, respectively.

II12. Morphological identification of basket-like projections *in vitro*

Image analysis was performed in Fiji-ImageJ (Schindelin et al., 2012). To characterize the morphology of Penk-positive and Penk-negative cells we considered as main feature of the neuron the presence of basket-like projections. Among basket-like projections, we

distinguished between “basket projections” and “PC projections”. We classified as “basket projections” those axon collaterals resembling the canonically described pinceau terminals of basket cells, which traverse the PCL and engulf the PCs bodies. On the other hand, we named “PC projections” those that even while reaching towards the PCs layer, do not traverse it.

II13. Quantification and statistical analysis

Additional calculations on the processed data were performed in Excel (Microsoft, Redmond, WA). Plotting and statistical analysis was done using Prism Version 9 (GraphPad, CA, USA). Mann-Whitney and Kruskal–Wallis test with Dunn’s multiple comparison correction where used where appropriate, as indicated in the results section. Significance was defined using GraphPad significance style with asterisks symbolizing number of significant digits, starting from a p-value ≤ 0.05 (*), $p \leq 0.01$(**), $p \leq 0.001$(***), $p \leq 0.0001$ (****) and $p > 0.05$ as non-significant (ns). In figures, summary plots are shown as median with error bars indicating the inter quartile range (IQR). Traces of neural activity and whisker angle are represented as mean response ± SEM. A power analysis was not performed prior to experimental procedures to predetermine numbers of replicates. Investigators were not blinded during outcome assessment.

II14. Data and code storage and availability

Each experiment was identified based on the unique id formed by the experimental date, time and a unique incrementing number. The details about each experiment within the imaging dataset were extracted from the xml file generated by the imaging software Prairie View and automatically written and stored in a MySQL database using a custom python script. Subsequently, analysis notes were manually added.

Analysis codes for Ca^{2+} imaging, whisker tracking as well as data processing and camera drivers are stored on the laboratory’s internal gitlab.pasteur.fr platform and are available upon request.

III. Results

Statement of contribution

The current work concerns the study of MLI diversity in representation in the lateral cerebellum of sensorimotor variables within the behavioural context of whisking. This project is a collaborative effort of members the DiGregorio laboratory. As first author I adapted and performed all the *in vivo* two-photon Ca^{2+} imaging and behavioural protocols, data processing and analysis of the Ca^{2+} traces and behavioural responses. The Neuropixels recordings and analysis were done by Zuzannna Piwkowska-Zvonkine. The *in vitro* imaging of MLIs was done by Berat Semihcan Sermet and Stefano Borda Bossana. I would like to acknowledge Giovanni Diana for developing the behaviour and Ca^{2+} analysis pipeline and help with data analysis, also Franziska Bender for her help with cranial window surgeries, imaging procedures and data analysis, Gael Moneron for developing the behavioural imaging software, Florian Ruckerl for building and maintaining the optical imaging system and Cécile Saint-Cloment for establishing and maintaining the mice crosses necessary and histology preparations. I would also like to acknowledge our collaborator Jason Christie for kindly providing us the Penk-Cre transgenic mouse line and for his valuable contribution to scientific discussions. All work was done under the supervision of David DiGregorio who had a principal role in the project design and data interpretation.

Introduction

Throughout the brain, precisely timed neural activity within neural networks is thought to be important in regulating synaptic strength and generating well-timed behaviours (Paton & Buonomano, 2018). This is also true for the cerebellum, a brain region critical for fine-tuning temporally precise behaviours contingent on sensory contexts. The cerebellar cortex transforms temporally distributed contextual representations into precise motor actions. Its neuronal circuit receives this sensory information and translates it into precisely timed, synchronised activity of its principal output neurons, the Purkinje cells (PCs) (Person & Raman, 2012). Despite the temporal diversity of its inputs, how PCs generate precisely timed neural activity remains an open question.

Molecular layer interneurons (MLIs) provide feed-forward inhibition to PCs and thus are in a pivotal position to shape the output of the cerebellar cortex. MLIs are diverse and are thought to vary in their dendritic and axonal morphology across a continuum that primarily correlates with their depth location within the molecular layer (Sultan & Bower, 1998; W. X. Wang & Lefebvre, 2022), leading to a differential impact on PC firing *in vivo* (A. M. Brown et al., 2019). Single-cell transcriptomic profiling has identified multiple classes of MLIs, consistent with distinct subtypes that may perform different functions (Kozareva et al., 2021).

Furthermore, MLIs encode both sensory (Chu et al., 2012) and motor features of whisker kinematics (Chen et al., 2017). Simple spike activity of PCs can be used to reconstruct whisker set point (Chen et al., 2016), but whether different subtypes show a systematic diversity in their representation of sensorimotor variables is not known. PCs receive increasing inhibition from MLIs with increasing depth within the PC layer (Arlt & Häusser, 2020). This could be due to 1) depth-dependent differences in GC activation (Straub et al., 2020) and/or 2) a depth-dependent diversity of MLI function.

However, how sensory and motor variables are balanced in the MLI representations is less understood. We, therefore hypothesize that MLIs might exhibit a depth-dependent diversity in their representation of sensorimotor variables. Here we investigate the depth-dependence of MLI representation of somatosensory and whisker kinematic information within the lateral cerebellum and how MLI sensory and motor representations change between evoked and spontaneous whisking.

III1. Depth-dependent differences in stimulus-evoked MLI Ca^{2+} responses amplitude and onset delay

Increased inhibition of PC simple spikes (Arlt & Häusser, 2020) and the acceleration of synaptic responses of MLIs (Chu et al., 2012) have been shown to vary with depth in the molecular layer relative to the pia. To investigate the mechanisms of this depth-dependence of MLI representations of sensory and motor information, we monitored MLI activity in awake head-fixed mice using high-speed two-photon (2P) imaging (100 Hz) of the rapid genetically encoded indicator GCaMP8f (Y. Zhang et al., 2023) following a brief air puff to the whisker pad (10 ms, 20 psi; **Figure III1 A**). MLIs were specifically transduced with GCaMP8f using an adeno-associated virus serotype 2.1 and the synapsin promotor (Syn). The simple stimulus

generates a reliable reflexive whisking bout that is associated with the millisecond precision recruitment of Purkinje and nuclear cells (S. T. Brown & Raman, 2018).

To reliably monitor from MLIs at different depths, we simply adjusted the image focal plane to be within the outer (**Figure III1 B,C**), inner (**Figure III1 D,E**) and middle third of the molecular layer. Repeated somatosensory stimulation of the ipsilateral whiskers to the imaging side (blocks of 30 trials for each focal plane) induced bilateral whisker protractions and wide-spread, coherent Ca^{2+} responses ($\Delta F/F(t)$) in both outer and inner MLIs (**Figure III1 C,E,F**), similar to MLI responses in the adjacent region Crus II during licking in MLIs (Astorga et al., 2017; Gaffield & Christie, 2017). Ca^{2+} responses in both regions were variable in their time course across the example fields of view, but reliable across trials (see cross-validation **Suppl. Figure III1.1**). Puff-evoked responses in inner MLIs showed smaller $\Delta F/F$ peak amplitudes (**Figure III1 B,D**) and a larger number of cells responding with short onset delays up to 24 ms before the start of whisker protraction (**Figure III1 C,E**). The number of cells showing detectable GCaMP8f fluorescence transients was consistent across depth (**Figure III1 F**) and most often was between 70 and 90%. To rule out movement artefacts, we monitored GCaMP8f transients in MLIs of a specific Cre-line sparsely co-expressing the activity-independent fluorescence reporter, tdTomato (Cre line discussed further in sections III2-3). Cells showing a fluorescence transient in the green (GCaMP8f) channel did not show a fluorescence change in the red, tdTomato, channel (**Suppl. Figure III1.2**). The stimulus-aligned average response traces for the whisker pads and individual cells across trials were fitted to an exponential curve (see section II Methods, **Figure III1 B,D**) used to further estimate differences in temporal patterns of activity (**Figure III1 G-J**).

As for the example FOVs, we observed a reliable depth-dependent decrease in peak amplitude (41% change; **Figure III1 F**) and an acceleration of the onset delay (from a median of 27 to 18 ms; **Figure III1 J**). The width of the fluorescence responses showed an increase with depth (**Figure III1 H)**, while there was no systematic depth-dependence of the time-to-peak (**Figure III1 I)**. It should be noted that the peak amplitude of the fluorescence response is strongly influenced by the number and frequency of neuronal spikes, while the time-to-peak and width relate to the duration of activity. The longer fluorescence decays are more related to the unbinding of calcium from the indicator, which is on the order of 30-40 ms for a single AP (Y. Zhang et al., 2023). Nevertheless, the depth dependence of onset, FWHM and peak amplitude are consistent with a systematic difference in the pattern and frequency of MLI firing

rates. The time-to-peak was not influenced by the peak amplitude, while all other parameters did not have a consistent effect on the Ca^{2+} response durations (**Suppl. Figure III1.3**).

Since air puff-evoked Ca^{2+} responses are concomitant with whisker deflection, we further analysed the patterns in whisker dynamics (**Suppl. Figure III1.4,5**). Averaged deflection kinematics following an air puff to one whisker pad induced a rapid bilateral protraction (rise) and slower retraction (decay) (**Suppl. Figure III1.4**), as shown previously (S. T. Brown & Raman, 2018). The onset delay, time-to-peak, and width of whisk deflection were on average 27 ms, 67 ms, and 136 ms, respectively. The whisk kinematic analysis showed a variable maximal angle of protraction and whisking duration (**Suppl. Figure III1.4 F,G**), with coordinated time-to-maximal whisker protraction between the two whisker fields and faster onsets for the ipsilateral whiskers, to which the puff-stimulation was applied (**Suppl. Figure III1.4 H, I**). We therefore analysed mostly the kinematics of the ipsilateral whisker field. Also, considering the higher prevalence of sensory inputs to the ipsilateral cerebellar hemisphere (Bosman et al., 2010, 2011), other parameters of whisker kinematics were inferred from the ipsilateral side of the whiskers, unless otherwise stated. Although the patterns of whisking show diversity between experimental sessions, no difference in maximal protraction, duration, time-to-maximal protraction and the onset of whisking between the whiskers corresponding to the sessions imaging at different depths (in outer, middle and inner, respectively) was found (**Suppl. Figure III1.5**), suggesting that the depth-dependent differences of MLI responses are most likely not explained by the behavioural variability.

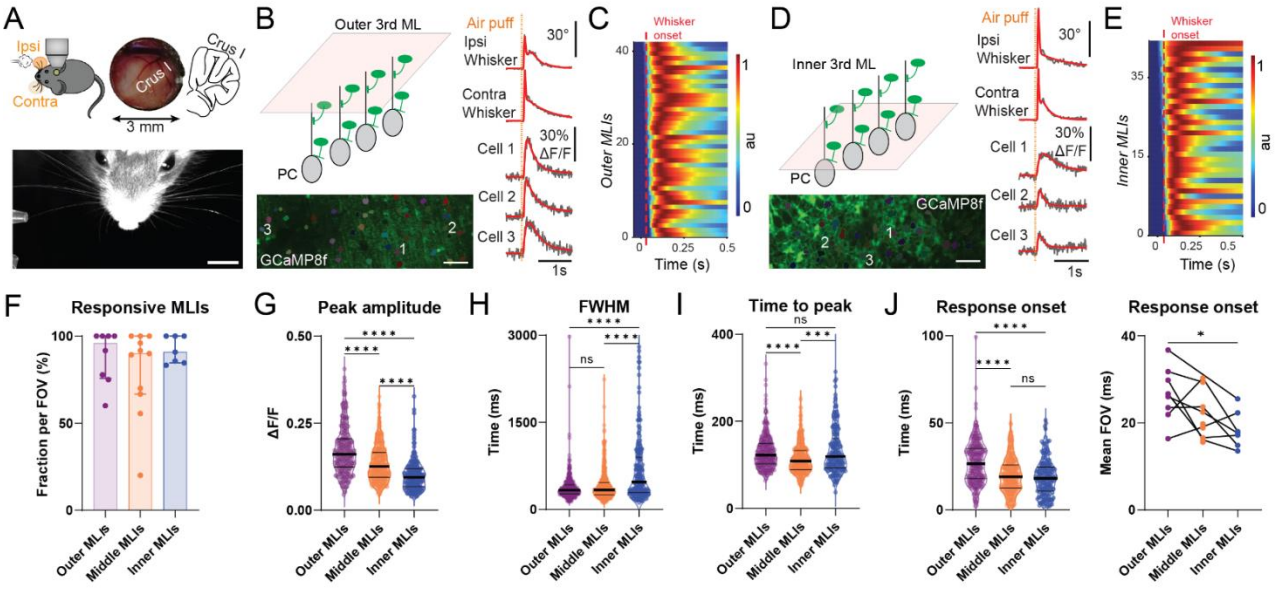

Figure III1. Depth-dependent differences in stimulus evoked MLI Ca^{2+} responses

(A) *Top:* Schematic of the experimental protocol comprised of 2p-imaging and air puff stimulation (10 ms, 20 psi, blocks or 30 trials) of the ipsilateral whisker to the imaging side (*left*). Example of cranial window over the left lateral cerebellum covering Crus I (*middle*) and schematic diagram of a sagittal section through the cerebellum highlighting the location of Crus I (*right*). *Bottom:* Example videography frame of a resting and awake head-restrained mouse during imaging recordings. Scale bar is 0.5 cm.

(B) *Left:* The 2-photon imaging plane through the cranial window was adjusted close to the pia to image the outer molecular layer (ML). Example of maximum intensity projection (MIP) of the imaging field of view (FOV) during *in vivo* recordings, with the extracted regions of interest (ROIs) of the somas of the molecular layer interneurons (MLIs). Scale bar is 50 µm. *Right*: Trial-averaged traces of the whisker deflection (upwards indicates protraction) and of GCaMP8f Ca^{2+} traces of three MLIs imaged at 100Hz (*grey*), with the superimposed exponential fits (*red*). Cell numbers correspond to the ROIs on the left. Orange dashed line represents the stimulus timing.

(C) Exponential fits of trial-averaged Ca^{2+} activity measurements of all responsive MLIs in the FOV presented in (B) normalized to the peak amplitude ordered by response onset, following air puff stimulation at time 0. Red dashed line represents the onset of the ipsilateral whisker protraction.

(D and E) The 2-photon imaging, example responses **(D)** and trial-averaged Ca^{2+} activity for the FOV **(E)** as in (B) and (C), but for an adjusted deeper plane, close to the Purkinje cell (PC) cell body to image the inner ML.

(F) The fraction of MLIs responsive to stimulation for each FOV present no statistical difference (outer ML: median (IQR) = 95.8 (75.7 – 100) %, n = 8 FOVs; middle ML: median (IQR) = 90.0 (66.7 – 100) %, n = 11 FOVs; inner ML: median (IQR) = 90.9 (84.6 – 100) %, n = 7 FOVs; 5 mice for all; ns $p > 0.05$ - not shown, Kruskal-Wallis with Dunn's multiple comparisons test). Error bars are median with interquartile range (IQR).

(G) Summary plot for peak amplitude of puff-evoked Ca^{2+} activity of MLIs imaged at different depths (each dot represents the trial-averaged MLI response, for the same FOVs as in (F)), in the outer (n = 315 cells), middle (n = 383 cells) and inner (n = 192 cells) ML, respectively, showing a depth-dependent significant decrease (outer: 0.16, middle: 0.13, inner: 0.10 ΔF/F, medians; ****$p < 0.0001$; Kruskal-Wallis with Dunn's multiple comparisons test). Error bars are median with IQR.

(H) Summary plot of the full width over half maximum (FWHM) of the same Ca^{2+} traces as in (G) showing a significant difference between the width of responses of inner MLIs compared to other layers (outer: 331, middle: 336, inner: 472 ms, medians; ****p < 0.0001; non-significant (ns) p = 0.88; Kruskal-Wallis with Dunn's multiple comparisons test). Error bars are median with IQR.
(I) Summary plot of the time-to-peak of the same Ca^{2+} traces as in (G) showing no depth-dependent trend, but significant differences between the middle MLIs compared to other layers (outer: 122, middle: 108, inner: 119 ms, medians; ****p < 0.0001; ***p = 0.0005, ns p = 0.96; Kruskal-Wallis with Dunn's multiple comparisons test). Error bars are median with IQR.
(J) *Left:* Summary plot of the response onset (measured at a delay to 10% to peak amplitude point) of the same Ca^{2+} traces as in (G) showing a depth-dependent significant decrease (outer: 27, middle: 19, inner: 18 ms, medians; ****p < 0.0001; ns p = 0.76; Kruskal-Wallis with Dunn's multiple comparisons test). Error bars are median with IQR. *Right*: Summary plot of the mean response onset comparison for location matched FOVs (outer – middle: n = 7 pairs, ns p = 0.47; outer – inner: n = 7 pairs, *p = 0.047; middle – inner: n = 6 pairs, ns p = 0.22; Wilcoxon matched-pairs signed rank test).
See also Supplementary Figures III1.1-5

III2. Ca^{2+} response onset time of MLIs precedes whisker onset, supporting a representation of the sensory stimulus

The observation that some cells respond before whisker onset argues against the initial activity being driven by sensory feedback from the whisking behaviour, and possibly encoding the whisker deflection to an air or a motor command corollary discharge. We therefore examined the prevalence and statistics of short-onset responses more in detail. For a given FOV, the average Ca^{2+} response precedes whisker movement for inner, but not outer MLIs (**Figure III2 A**). Across experiments, the average onset delay of outer MLI Ca^{2+} responses were similar to that of the whiskers (outer MLIs: mean = 27 ms; whiskers: median = 25 ms; $p > 0.05$; Kruskal-Wallis test, n = 8 FOVs, 5 mice; **Figure III2 B**) with evenly distributed fast and slow MLIs that precede or succeed the whisk onset, respectively (**Figure III2 C**). Meanwhile, MLIs in the middle and inner layers showed onset delays that were ~6 ms faster on average as compared to that of whisker deflections (middle MLIs: mean = 19 ± 0.5 ms, median = 19 ms, n = 11 FOVs; inner MLIs: mean = 19 ± 0.8 ms, median = 18 ms, n = 7 FOVs; middle MLIs - whiskers $p < 0.01$, inner MLIs – whiskers: $p = 0.001$, Kruskal-Wallis test; n = 5 mice; **Figure III2 B,C**). Fast puff-evoked MLI responses were observed in 6 out of 7 putative MLIs recorded with high-temporal resolution electrophysiological recordings with Neuropixels probes during the same stimulation protocol (**Suppl. Figure III2.1**). The peak firing rates of their responses (mean = 16 ± 3.3, median = 15, n = 3 experiments, 3 mice) are comparable to the delays found with Ca^{2+} transients. Those values are also consistent with previously reported sensory responses of MLIs to air puff in anaesthetized mice, showing ∼20 ms delays from the puff onset (Chu et al., 2012). In the middle and inner layers, we observed a larger fraction of MLIs that respond before whisk onset (>50 %; **Figure III2 B, C)**. Nor do we see a correlation between the Ca^{2+} response onset and that of whisking (**Figure III2 D**). Thus, proprioceptive signals from whisking cannot account for these shorter delays. It then begs the question as to whether the depth-dependence of onset delays imply a depth-dependence in representation of the somatosensory information evoked by the air puff. We will investigate this further in subsequent figures (sections III6-9). Although, an alternative hypothesis is that the depth-dependence of Ca^{2+} responses are due to the distribution of specific cell-types. We test the latter hypothesis below.

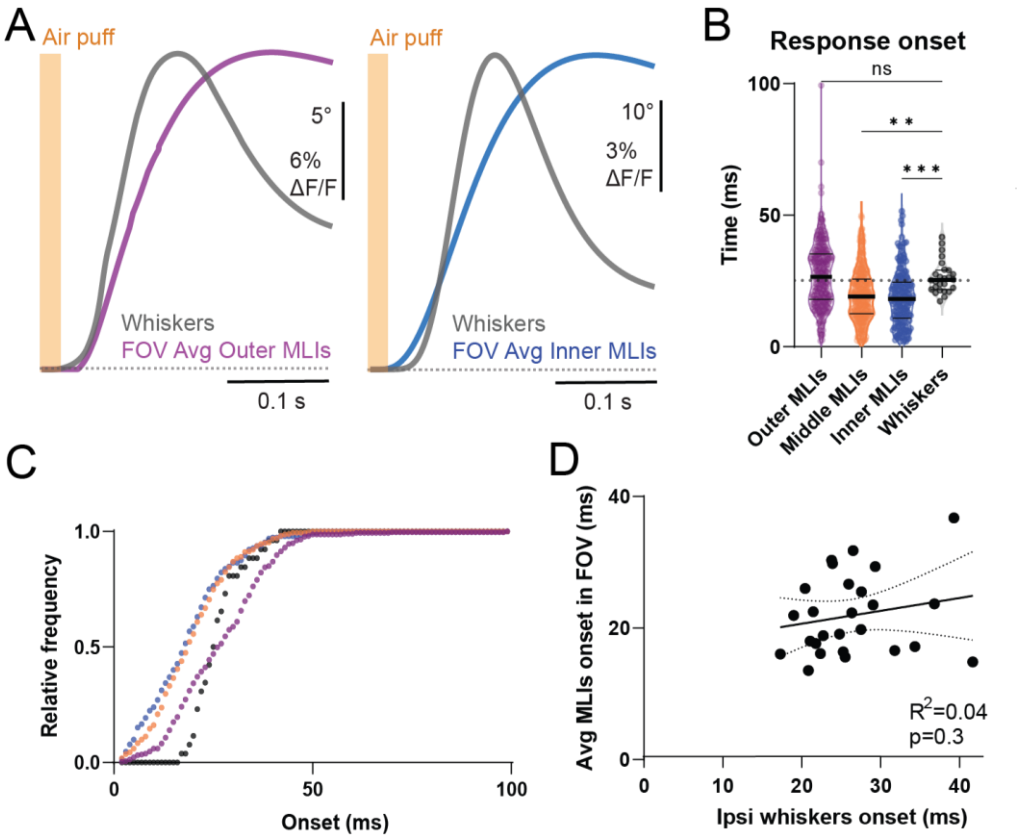

Figure III2. Ca^{2+} response onset time of MLIs precedes whisker onset

(A) Superimposed exponential-fits of trial-averaged whiskers (*grey*) and Ca^{2+} trace across MLIs in the FOV, for an example session in the outer (*magenta, left pannel*) and inner (*blue, right panel*) ML, immediately following whisker air puff stimulation (*orange*). Note the difference in onset for the outer and inner MLIs to the corresponding whisking behaviour.
(B) Summary plot for response onset of puff-evoked Ca^{2+} activity of MLIs imaged at different depths and ipsilateral whiskers of all sessions (n = 26 sessions), showing a depth-dependent significant difference between the onset of cells and behavioural response (outer: 27, middle: 19, inner: 18, whiskers: 25 ms, medians; ns $p > 0.99$; **$p = 0.002$, ***$p = 0.0005$; Kruskal-Wallis with Dunn's multiple comparisons test). Dashed black line marks median of whisker response onset. Error bars are median with IQR.
(C) Frequency distribution (1 ms bins) of the values measured in (B).
(D) Cross-correlation of the response onset of the cell-average MLIs in each FOV vs whiskers ($r = 0.21$, Spearman's rank correlation). Linear fit black line with 95% CIs dashed black line.

III3. *Penk1* gene marks a subset of MLIs whose somas are predominantly located in deep molecular layers and form basket-like terminals

To test whether the depth dependence of MLI responses is related to MLI cell types, we sought out markers for MLI types thought to be predominantly deep in the molecular layer. MLIs are comprised of dendritic targeting (stellate cells) and somatic targeting (basket cells) neurons (Palay & Chan-Palay, 1974). Whether they contain distinct classes is more controversial (Sultan and Bower, 1998), but recent evidence further supports a continuum of cell-type variation (Wang and Lefebre). MLIs were recently categorised into two main classes (MLI1 and MLI2) based on transcriptional profiling, that span the entire depth of the molecular layer and underlie functional differences (Kozareva et al., 2021) and therefore do not correlate with depth-dependent properties. However, mining the cell RNA sequencing (scRNA-seq) database provided by Kozareva et al. (2021) (**Figure III3 A**), we identified *Penk1* gene as a potential marker for MLIs that are preferentially located in the inner molecular layer. Indeed, in situ hybridization (ISH) labelled Penk1 RNA expression from the Allen Mouse Brain Atlas (Allen Institute for Brain Science, 2004; Lein et al., 2007) confirms that the expression of Penk1 is confined to within the molecular and GC layers, with a clear bias towards the deep molecular layer (**Figure III3 B**). Within the cerebellar cortex, Penk1 RNA expression exclusively overlaps within the cell type clusters expressing *Gjd2* gene that marks electrical coupling, namely MLIs (type 1) and Golgi cells (**Figure III3 A**).

The expression pattern of Penk+ cells looked suspiciously like that expected for MLIs that target PC somas and contribute to the pinceau morphology of those axon terminals. To examine the morphology of Penk-expressing MLIs (Penk+), we used a transgenic Penk-Cre mouse line crossed with the Cre-dependent tdTomato reporter line (see section II Methods), to selectively express the tdTomato dye in Penk+ cells (**Figure III3 C**). Penk-negative (Penk-) cells were first visualised using DODT imaging and identified by the lack of tdTomato expression (see section II Methods**; Figure III3 D,E**). Penk- and Penk+ MLIs were whole cell patched (in acute brain slices) with Alexa 488 in the internal solution and imaged using 2P microscopy (810 nm) to characterize their morphology. Over 2/3 of the Penk+ MLIs analysed had axonal projections that traversed the PC layer and appeared to envelope PC somas, typical of previously identified basket cell terminals (**Figure III3 C,G**). In contrast, only one of 15 Penk- MLIs (identified by negative staining) exhibited axons that traversed the PC layer (**Figure III3 F,H**). Several Penk- MLIs appeared to project to the PC layer but did not traverse

the layer and thus did not form typical basket-like terminals. These data strongly suggest that the *Penk1* gene can be used as a marker for a subset of MLI1 that form basket terminals.

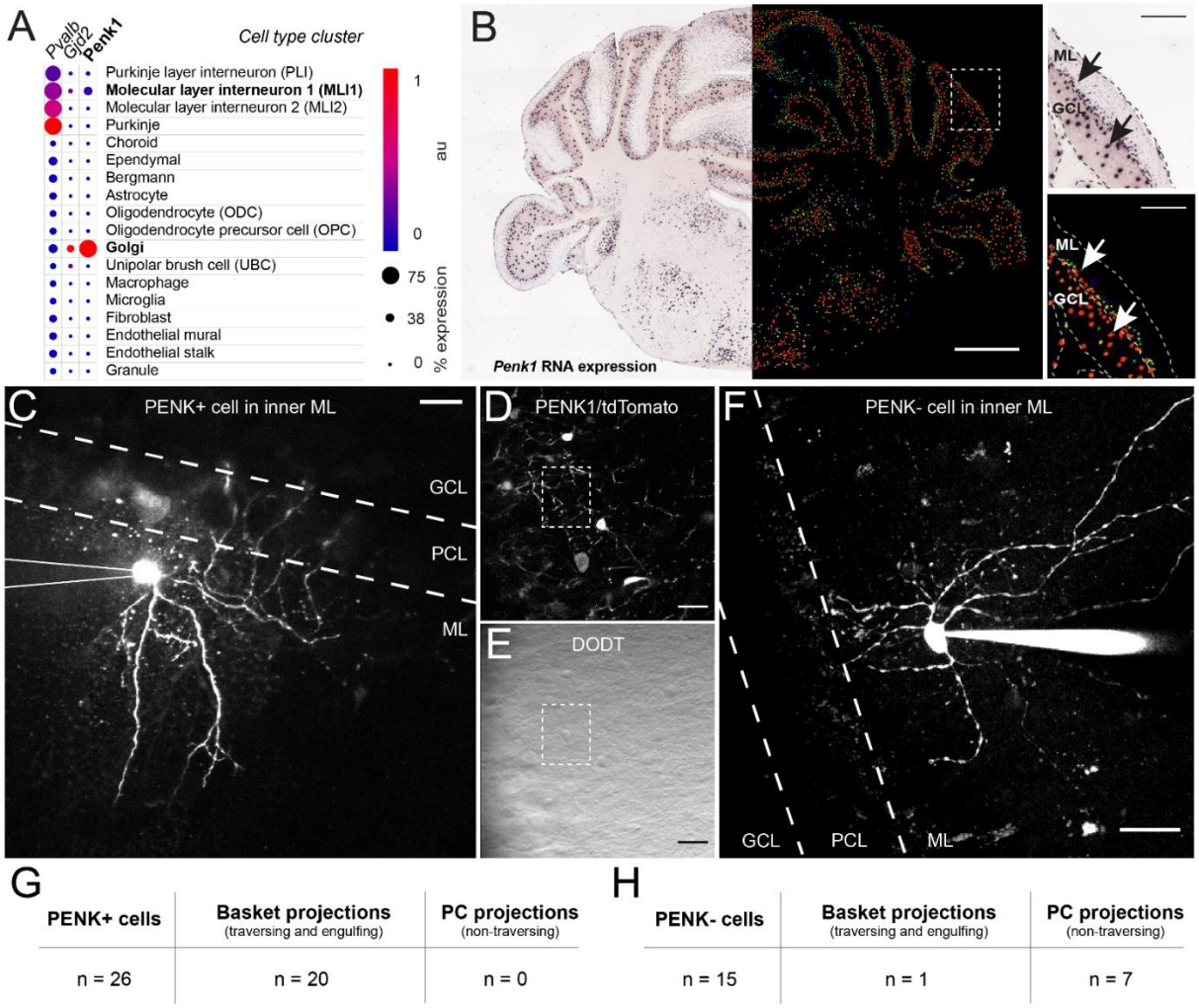

G

PENK+ cells	Basket projections (traversing and engulfing)	PC projections (non-traversing)
n = 26	n = 20	n = 0

H

PENK- cells	Basket projections (traversing and engulfing)	PC projections (non-traversing)
n = 15	n = 1	n = 7

Figure III3. *Penk1* gene marks a subset of MLIs preponderantly deeper with basket-like terminals

(A) Scaled RNA expression pattern of *Parvalbumin* (*Pvalb*), *Gjd2* and *Penk1* in cerebellar cortex cell types characterized using snRNAseq. Database from Kozareva et al. (2021) accessed through the single Cell Portal study (https://singlecell.broadinstitute.org/single_cell/study/SCP795/).
(B) *In situ* hybridization labelled RNA expression of *Penk1* in the adult mouse brain. Allen Mouse Brain Atlas, mouse.brain-map.org/experiment/show/74881286. Indent shown on the right. Arrows indicate Penk-expression in the molecular layer (ML) and the granule cell layer (GCL). Scale bar is 1000 µm (*left*) and 250 µm (*right*, indent).
(C) Representative maximum intensity projection of a Z-stack of images from a *Penk1*/tdTomato-expressing cell (Penk+) in the inner ML, under 2-photon excitation (920 nm). Note traversing and engulfing basket-like projections of the cell into the Purkinje cell layer (PCL). Dashed line delimitates ML, PCL, and GCL. Scale bar is 20 µm.
(D) Representative FOV from acute brain slice under 2-photon excitation (920 nm) showing *Penk1*/tdTomato-expressing cells. Scale bar is 20 µm.
(E) DODT imaging is used to identify Penk- cells (same FOV as in (E) showed). Inset highlights the cell body of the Penk1/tdTomato-negative neuron. Scale bar is 20 µm.
(F) Maximum intensity projection of a Z-stack of images of the whole cell patched (Alexa 488 filled) Penk- cell highlighted in (E) under 2p –excitation (810 nm). Scale bar is 20 µm.

(G-H) Summary tables for the morphological characterization of basket-like projections in Penk+ and Penk- cells, subdivided between basket projections (traversing the PCL and engulfing the PCs bodies) and PC projections (not traversing the PCL).

III4. Ca^{2+} response onset and peak amplitude are similar between Penk-expressing and non-expressing MLIs at the same depth

To determine whether Penk+ MLIs exhibit short onset delays consistent with the inner layer MLI responses to whisker pad air puffs, we set out to compare puff-evoked GCaMP8f responses in Penk+ and Penk- MLIs. To do this, we transduced all MLIs with AAV1-Syn-GCaMP8f in Penk-Cre x tdTomato mice, allowing the recording of fluorescence responses in both Penk+ and Penk- cells (**Figure III4 A, B**). The number of Penk+ and – MLIs in the outer, middle and inner molecular layer shows that the number of Penk expressing MLIs gradually increases with depth, indicating a four-fold increase between outer and inner layers (**Figure III4 B**; n = 890 cells, 26 FOVs, 5 mice). Puff-evoked fluorescence responses from inner Penk+ neurons were small amplitude and exhibited a rapid onset delay, similar to the whole population of inner MLIs (**Figure III4 C)**. However, the outer layer Penk+ neurons had larger peak amplitudes and exhibited longer onset delays. This depth dependence was indistinguishable from Penk- MLIs and was similar to the depth dependence shown in Figure III1 (**Figure III4 D; Suppl. Figure III4.1**). Thus, the laminar diversity of MLIs cannot be accounted for by the unique laminar distribution of Penk+ MLI1s. Although we cannot rule out the possibility that other MLI1 or ML2 neurons have distinct air puff response properties, the large fraction of Penk+ MLIs in the inner molecular layer (67%) strongly suggests that the depth dependence of MLI responses are not accounted for by cell-type specific properties.

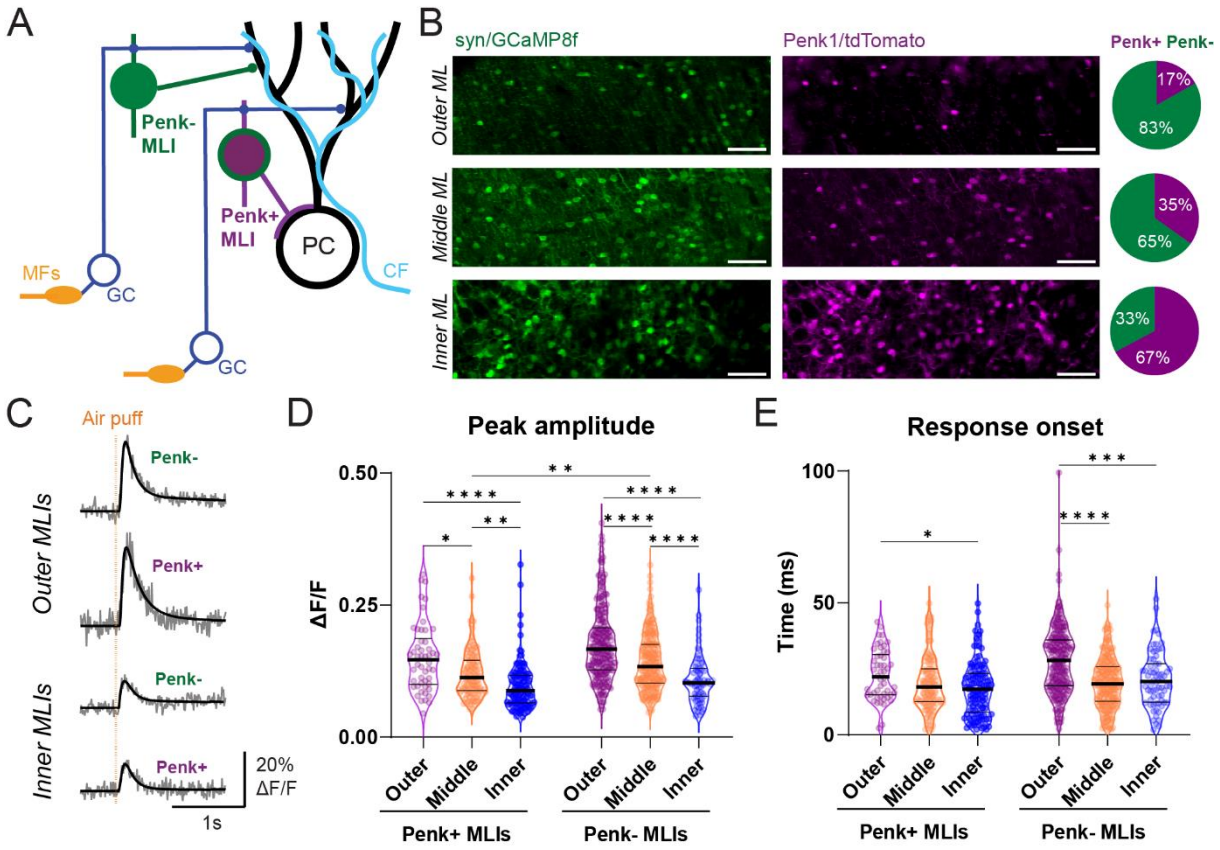

Figure III4. Similar Ca^{2+} response onset and peak amplitude of depth-matched Penk+ and Penk- MLIs

(A) Penk+ and Penk- mLIs express the Ca^{2+} indicator GCaMP8f (*green*), while only Penk+ cells are co-labelled with the *Penk1* cre depenent tdTomato (*magenta*). Within the cerebellar cortex, representative deeper MLIs are Penk+ and target the soma of the PC, while representative outer MLIs are Penk- and target the dendritic tree of PCs. MLIs transform sensorimotor information received GCs which in turn receive it via mossy fibres (MFs) entering the cerebellar cortex, while PCs also receive input from climbing fibres (CF).
(B) MIP of representative FOVs at different depths (top to bottom: outer, middle and inner ML) during 2p-imaging *in vivo* of Penk-cre x tdTomato mice, for the two imaging channels: green (GCaMP8f, *left*) and magenta (cre-dependent tdTomato, *middle*). Scale bar is 50 µm. *Right*: Pie charts showing quantification of Penk+ (co-expressing GCaMP8f and tdTomato) and Penk- (expression of GCaMP8f only) MLIs in the respective planes (outer: n = 50 Penk+ and 265 Penk- cells, 8 FOVs; middle: n = 130 Penk+ and 253 Penk- cells,11 FOVs; inner n = 124 Penk+ and 68 Penk- cells, 7 FOVs, 5 mice), showing depth-dependent increased expression of Penk+ cells.
(C) Example trial-averaged traces of GCaMP8f Ca^{2+} traces a Penk+ and Penk- MLI from the same FOV (*grey*), with the superimposed exponential fits (*black*) in the outer (*top*) and inner (*bottom*) ML, respectively. Orange dashed line represents the stimulus timing.
(D) Summary plot for peak amplitude of puff-evoked Ca^{2+} activity of MLIs imaged at different depths (each dot represents the trial-averaged MLI response, for the same FOVs as in (B)), segregated based on Penk expression, showing a conserved decrease with depth independent of *Penk* expression (layer-matched non-significant differences not shown $p > 0.05$, *$p < 0.05$, **$p < 0.01$, ***$p < 0.001$, ****$p < 0.0001$; Kruskal-Wallis with Dunn's multiple comparisons test). Error bars are median with IQR.

(E) Summary plot of response onset of the same Ca^{2+} traces as in (D) showing a conserved decrease with depth independent of *Penk* expression (layer-matched non-significant differences not shown $p > 0.05$, *$p < 0.05$, ***$p < 0.001$, ****$p < 0.0001$; Kruskal-Wallis with Dunn's multiple comparisons test). Error bars are median with IQR.

III5. Depth-dependent differences in GC parallel fibres Ca^{2+} response onset delay

Experiments in acute cerebellar brains slices demonstrated a laminar dependence of the speed of AP conduction velocities, with deep PFs transmitting electrical information the fastest (Straub et al. 2020). Other studies have observed a particular MF-GC connectivity that suggest a non-random laminar organization of information flow within the PF population (Shuster et al. 2021; Kim et al. 2023). We next examined whether the depth-dependent MLI responses are inherited from a laminar organization of GC activity, perhaps even due to a spatial segregation of sensory modalities within the PF population. GCaMP8f was expressed specifically in GCs using a Flexed AAV virus and the a6-GABA receptor-Cre mice. We imaged PF responses in similar focal planes in the depth of the molecular layer as for the imaging of MLIs using identical air-puff stimulus protocols (outer, middle and inner molecular layer, n = 155 PFs, 43 FOVs, 7 mice; **Figure III5 A,B**). The peak amplitude of PF responses did not show a significant depth dependence, (**Figure III5 C**), whereas the width (FWHM) and time-to-peak decreased with depth, which were not observed in MLI responses (**Figure III5 D,E**). The FWHM of MLI responses lengthened with increasing depth, which cannot be explained by the population response properties of PFs. However, the onset delay of PF responses accelerated with increasing depth (from 37 to 25 ms, medians; **Figure III5 F**), reminiscent of the laminar dependence of the offset delay found in MLIs. A direct comparison of the onset delays within layers showed that the MLI onset delays were systematically faster than their PF counterparts. We confirmed that the whisker kinematics were not statistically different between MLI and PF experiments kinematics (23 vs 25 ms, medians for experiments associated with PFs and MLIs, respectively; **Figure III5 G**). Notably, the variability in onset delays was much larger than that in MLIs (*outer ML*: median (IQR) PFs = 37 (17-80) ms vs median (IQR) MLIs = 27 (18-35) ms; *inner ML*: median (IQR) PFs = 25 (16-39) ms vs median (IQR) MLIs = 18 (11-25) ms; **Figure III5 G**). These PF findings are consistent with a distributed temporal representation predicted by modelling studies (Medina and Mauk, 2000).

But how can we account for the faster onset times? It seems plausible that the MLI dendritic tree samples from thousands of PFs (Abrahamsson et al., 2012; Palay & Chan-Palay, 1974), such that there is a high probability of MLIs receiving "fast" PFs, which have short onset delays are sufficient to trigger an AP. Nevertheless, the laminar dependence of onset delays is present

in the PF population suggesting that the spatial dependence of MLI responses is inherited from GCs and biased towards the synaptic input of the short-delay GCs.

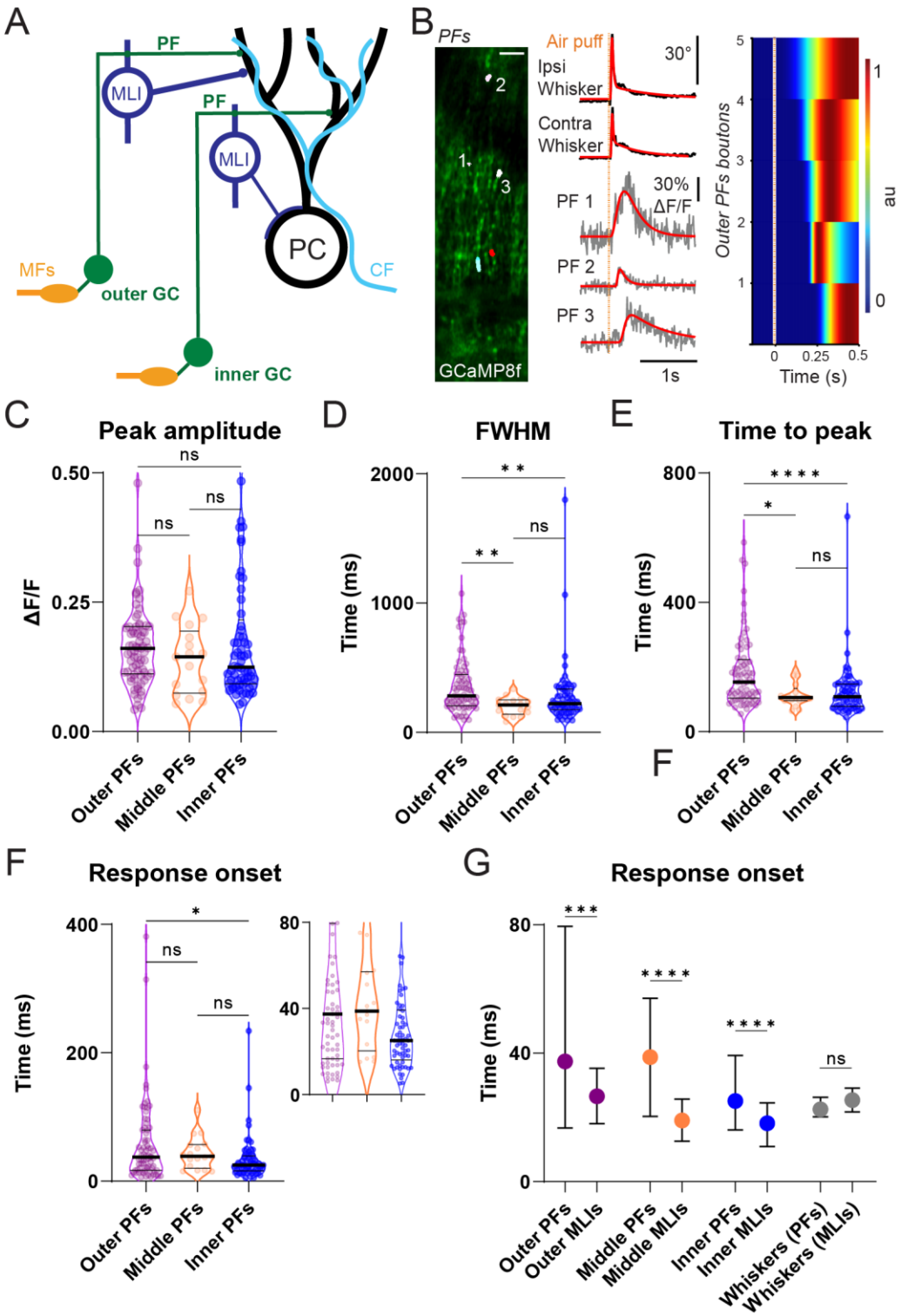

Figure III5. Depth-dependent differences in GCs parallel fibres Ca^{2+} responses

(A) GCs expressing the Ca^{2+} indicator GCaMP8f (green) form layered parallel fibres (PFs) that target MLIs at different depths.
(B) *Left:* MIP of a representative FOV during *in vivo* 2p imaging of PFs expressing GCaMP8f (example from outer ML region). Example of maximum intensity projection (MIP) of the imaging field of view (FOV) during *in vivo* recordings, with the extracted ROIs of boutons. Scale bar is 10 µm. *Middle*: Trial-averaged traces of the whisker deflection (upwards indicates protraction) and of GCaMP8f Ca^{2+} traces of three PFs imaged at 100Hz (*grey*), with the

superimposed exponential fits (*red*). Cell numbers correspond to the ROIs on the left. *Right:* Exponential fits of trial-averaged Ca^{2+} activity measurements of all responsive PFs in the FOV normalized to the peak amplitude and ordered by response onset. Orange dashed line represents the stimulus timing.
(C) Summary plot for peak amplitude of puff-evoked Ca^{2+} activity of PFs imaged at different depths (each dot represents the trial-averaged PF response, n = 7 mice), in the outer (n = 73 cells, 19 FOVs), middle (n = 17 cells, 7 FOVs) and inner (n = 65 cells, 18 FOVs) ML, respectively, (outer: 0.16, middle: 0.14, inner: 0.13 ΔF/F, medians; outer – middle: ns p = 0.51, outer – inner: ns p = 0.89, middle – inner ns p > 0.99; Kruskal-Wallis with Dunn's multiple comparisons test). Error bars are median with IQR.
(D) Summary plot of the FWHM of the same Ca^{2+} traces as in (C) showing a significant depth-dependent difference (outer: 282, middle: 212, inner: 223 ms, medians; outer – middle: **p = 0.002, outer – inner: **p = 0.009, middle – inner ns p = 0.43; Kruskal-Wallis with Dunn's multiple comparisons test). Error bars are median with IQR.
(E) Summary plot of the time-to-peak of the same Ca^{2+} traces as in (C) showing a significant depth-dependent difference (outer: 154, middle: 106, inner: 108 ms, medians; ns p > 0.99, *p = 0.002, ****p < 0.0001; Kruskal-Wallis with Dunn's multiple comparisons test). Error bars are median with IQR.
(F) Summary plot of the response onset of the same Ca^{2+} traces as in (C) showing a significant depth-dependent difference (outer: 37, middle: 39, inner: 25 ms, medians; outer – middle: ns p > 0.99, outer – inner: *p = 0.03, middle – inner: ns p = 0.15; Kruskal-Wallis with Dunn's multiple comparisons test). Error bars are median with IQR.
(G) Summary plot showing significantly shorter response onsets of MLIs compared to PF in the corresponding layer (outer: 37 vs 27, middle: 39 vs 19, inner: 25 vs 18, whiskers: 25 vs 23 ms, medians of PFs and MLIs; *** p = 0.0002; ****p < 0.0001, ns p = 0.07, Mann-Whitney test for each group). Error bars are median with IQR.

III6. Depth-dependent differences in correlations of Ca^{2+} responses time-to-peak and whisker movement kinematics

It has previously shown that MLIs encode motor command information and proprioceptive feedback of spontaneous whisker movements (Chen et al., 2017), as well as somatosensory information about the air puff stimulation (Chu et al., 2012). Nevertheless, the contribution of sensory and motor variables during sensory evoked whisking in awake mice, has not yet been examined. To probe how the responses of MLIs at different depths represent behaviour and or sensory stimulation by the air puff, we compared the mean Ca^{2+} responses of the MLIs in each FOV to their corresponding whisker kinematics (**Figure III6**). We did not find a consistent relationship between the peak amplitude and width of the Ca^{2+} traces of outer MLIs and the protraction angle and whisking duration, respectively (**Figure III6 A,B**), but observed a strong correlation between the time-to-peak of the Ca^{2+} response and maximal protraction of the whiskers ($r = 0.81$, $R^2 = 0.66$; **Figure III6 C**). In contrast, none of the inner MLI response parameters correlated with the kinematics of the whiskers (**Figure III6 D,E,F**). It is therefore possible that the timing of the puff-induced protraction influences the firing pattern of MLIs in a depth dependent manner.

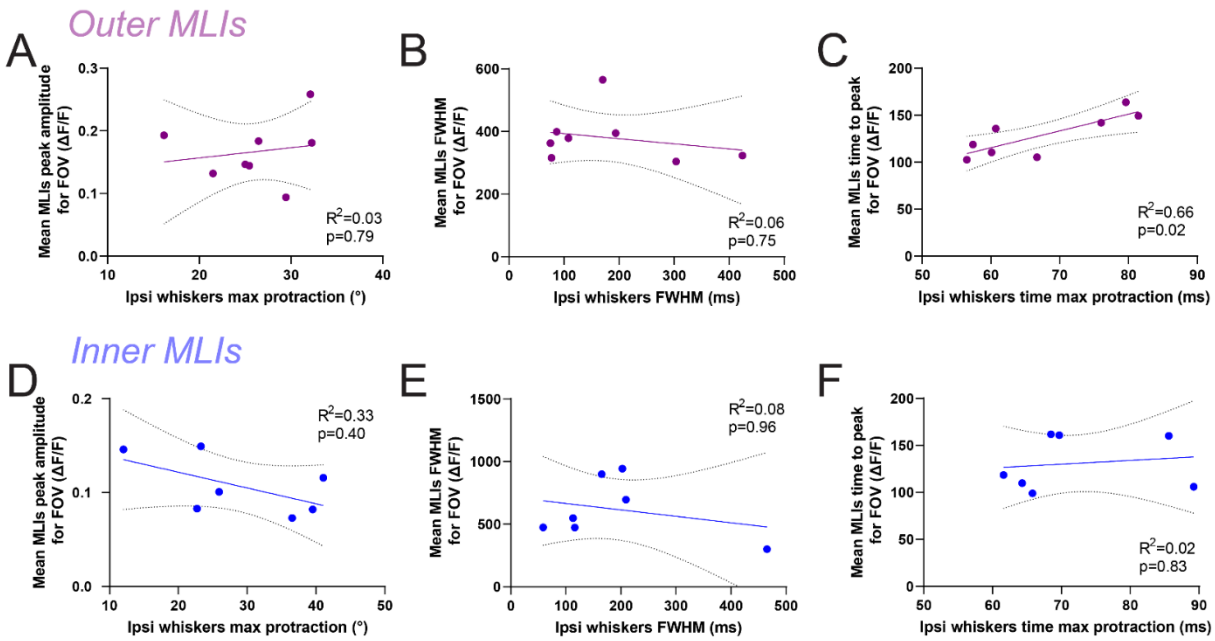

Figure III6. Depth-dependent differences in correlations of Ca^{2+} responses time-to-peak and whisker movement kinematics

(A) Cross-correlation of the peak amplitude of the cell-average outer MLIs in each FOV vs whiskers maximal protraction angle (r = 0.12, Spearman's rank correlation). Linear fit line with 95% CIs dashed black line.
(B) Cross-correlation of the FWHM of the cell-average outer MLIs in each FOV vs whiskers (r = -0.14, Spearman's rank correlation). Linear fit line with 95% CIs dashed black line.
(C) Cross-correlation of the time-to-peak of the cell-average outer MLIs in each FOV vs whiskers time to maximal protraction (r = 0.81, Spearman's rank correlation). Linear fit line with 95% CIs dashed black line.
(D – F) Cross-correlations of the same parameters measured (A – C) for the Ca^{2+} activity of inner MLIs vs whiskers, **(D)** peak amplitude vs maximal protraction angle (r = -0.39), **(E)** FWHM (r = 0.04), **(F)** time-to-peak vs time to maximal protraction (r = 0.11), Spearman's rank correlation. Linear fit line with 95% CIs dashed black line.

III7. Time-to-peak of average Ca^{2+} responses and whiskers correlate stronger for slow-onset MLIs

Thus far we have described two results that suggest somatosensory and whisk-related variables have a spatially biased organization according to depth within the molecular layer: 1) MLI response onset delays occurring before whisk onset are more prominent in the inner molecular layer (**Figure III1-2**); 2) Ca^{2+} response time-to-peak is correlated with the peak protraction angle only in outer MLI responses **(Figure III6)**. The remainder of the chapter will be dedicated to exploring the evidence of spatial biases in MLI encoding of sensory-motor information.

Because MLIs responses occurring before the whisk are likely to encode features of the air puff stimulus (and perhaps motor commands), we next examined if those cells with onsets after the start of whisking might be biased towards encoding whisk parameters (*slow onset cells*). First, we aligned Ca^{2+} response onsets to the onset of the trial-averaged whisk (n = 890 cells, 26 FOVs, 5 mice). We then classified MLIs as slow-onset and showed that only 26% of inner MLIs are slow-onset, while 53% of cells in the outer layer were slow-onset ($p < 0.0001$ outer vs middle and inner layers, Kruskal-Wallis test; **Figure III7 A**). If we calculated the fraction of slow-onset MLIs across FOVs, we observed a similar decrease in the relative number with increasing depth (**Figure III7 B**). The higher prevalence of slow-onset MLIs in the outer layers may underlie the correlation seen between the time-to-peak of outer MLIs and whiskers kinematics that was not reproduced in the inner layers (**Figure III6 C,F**). To further investigate this possibility, we analysed the mean Ca^{2+} responses within each FOV for all MLIs or for only slow-onset MLIs. We then correlated those means to their corresponding whisker kinematics (**Figure III7 C-H**). The peak amplitude and width of Ca^{2+} responses did not correlate with and kinematic parameters, regardless of the onset-delay category (**Figure III7 C-F**). However, the time-to-peak of the Ca^{2+} response and maximal whisker protraction angle did correlate and was made stronger when excluding the fast-onset cells (all MLIs: $r = 0.55$, $R^2 = 0.26$ vs slow-onset MLIs: $r = 0.61$, $R^2 = 0.61$; **Figure III7 G,H**). These data are consistent with slow-onset MLIs being more prevalent in the outer molecular layer and having a bias in their whisk representation when compared to fast-onset MLI responses.

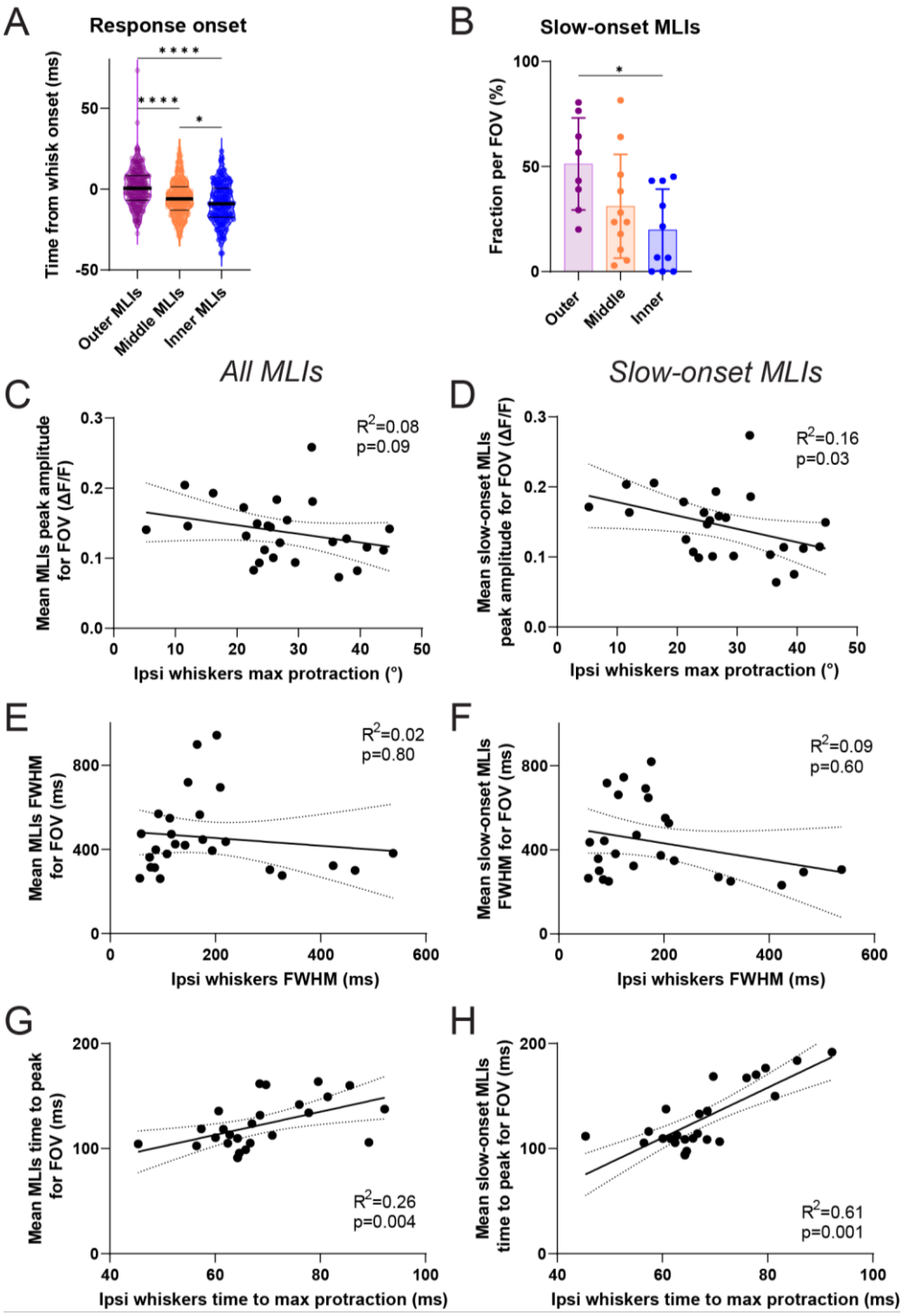

Figure III7. Time-to-peak of average Ca^{2+} responses and whiskers correlate stronger for slow-onset MLIs

(A) Summary plot of the response onset of the Ca^{2+} traces aligned to the onset of the whisk, showing a depth-dependent significant decrease (outer: 0.6, middle: -6, inner: -9 ms, medians; ****p < 0.0001; *p = 0.04; Kruskal-Wallis with Dunn's multiple comparisons test). Error bars are median with IQR.
(B) Summary plot of the fraction of slow-onset MLIs (following whisker onset) for FOVs of outer (median = 50%), middle (median = 24%) and inner (median = 14%) ML, showing a significant depth-dependent decrease (*p = 0.03, non-significant comparisons p >0.05 not

shown; Kruskal-Wallis with Dunn's multiple comparisons test). Error bars are median with IQR.
(C – D) Cross-correlation of the peak amplitude of the cell-average Ca^{2+} traces in each FOV vs whiskers maximal protraction angle for all (r = -0.34) and slow-onset MLIs (r = -0.43). Spearman's rank correlation. Linear fit line with 95% CIs dashed black line.
(E – F) Cross-correlation of the FWHM of the cell-average Ca^{2+} traces in each FOV vs whiskers for all (r = 0.05) and slow-onset MLIs (r = -0.11). Spearman's rank correlation. Linear fit line with 95% CIs dashed black line.
(G – H) Cross-correlation of the time-to-peak of the cell-average Ca^{2+} traces in each FOV vs whiskers time to maximal protraction for all (r = 0.54) and slow-onset MLIs (r = 0.61). Spearman's rank correlation. Linear fit line with 95% CIs dashed black line.

III8. Ca^{2+} responses are longer when increasing stimulus duration

While early-onset MLIs are likely to encode information about the air-puff, it is not clear if all MLIs have a sensory component and the spatial distribution of onset delays represents a cellular or circuit delay (Straub et al. 2020). To specifically examine MLI sensitivity to somatosensory stimuli we delivered air puff stimulation with increased duration (10 and 1000 ms), thus potentially biasing MLI response in favour of the somatosensory stimulation (**Figure III8 A**). To minimise confounding stimulus of the eye, we oriented the puff direction to be perpendicular to the whiskers and reduced the pressure of the stimuli to 5 psi (see section II Methods). **Figure III8 A,B** shows an example in which a 1000 ms air puff evoked a prolonged Ca^{2+} response the outlasted the whisking duration. Following 1000 ms air puff stimulation, 57% of the MLIs showed Ca^{2+} responses with widths greater than 1000 ms. In comparison, only 9% of MLIs exhibited long-lasting Ca^{2+} responses for 10 ms front stimuli. In contrast, the duration of the whisking remained comparable for the two puff durations (189 ms and 156 ms, medians for short and long front stimulations, respectively; **Figure III8 B**) and did not mirror the changes in MLIs Ca^{2+} response duration. The strong sensitivity of MLIs to stimulus intensity also manifested in a longer Ca^{2+} response duration for the higher pressure 10 ms puff, as compared to the 5 psi, 10 ms puff delivered to the front (from 393 to 311 ms, medians; **Figure III8 B**).

The other parameter that did not correlate to motor features following brief pad stimulation is the peak amplitude of the Ca^{2+} response (**Figure III7 C,D**), which remains overall constant throughout stimulation types (**Figure III8 A,D**). This pattern in MLI response is independent of the amplitude of the whisker protractions, which are systematically larger during strong pad stimulation compared to the mild front simulation (**Figure III8 E**). The protraction angle of contralateral whiskers remained similar for short and long front stimulation (**Figure III8 A,E**), while the ipsilateral whisker was deflected backwords by the air puff, suppressing whisking on the stimulated side (**Figure III8 F**). A robust depth-dependent decrease in peak amplitude was also observed for stimulation protocols, as well as a systematic acceleration of the onset of response, as expected for a parameter that is independent from stimulus duration (**Suppl. Figure III8.1 A,D**).

To assess how the stimulus duration affects the response of individual MLIs, we further delivered interleaved short and long stimuli (10 vs 1000 ms) and analysed the change in the width and peak amplitude of MLI responses for the two puff durations (n = 333 MLIs, 11 FOVs,

3 mice; **Figure III8 G-M, Suppl Figure III8.3**). As with pad stimulation (**Figure III1 F**), the short front puff to the whiskers induced wide-spread responses in 74.3% of the MLIs and recruited an additional 12.7% of the population during longer stimulation (**Figure III8 G**). Interestingly, a small proportion of cells 1.6% responded to short stimuli, but did not show detectable responses during sustained puffs (**Figure III8 G**), possibly due to recruitment of inhibition from other MLIs or Purkinje layer interneurons (Kondo & Marty, 1998b; Miyazaki et al., 2021; Osorno et al., 2021). Most MLIs significantly increase their response duration from short to long stimulation up to 33-fold (96.5%; **Figure III8 H, I**), in a similar fashion across depth (**Figure III8 J**), and to various degrees (**Figure III8 I; Suppl Figure III8.3 A**), suggesting a distribution in the somatosensory sensitivity of MLIs. The more sensitive cell-matched analysis suggests that MLIs have a greater tendency to increase their amplitude of response with longer stimulation (**Figure III8 K, Suppl Figure III8.3 B**), with an average change of only 20% (**Figure III8 L**) and in a similar manner across depth (**Figure III8 M**), suggesting that Ca^{2+} response width is a better metric for predicting somatosensory stimulus duration.

We did not, however, observe a laminar dependence in the duration sensitivity or peak amplitude sensitivity of MLIs (**Figure III8 J, M; Suppl. Figure III8.1 B**). In contrast, the long puff stimulation induced comparable long Ca^{2+} responses across layers with longer times to peak (**Suppl. Figure III8.1 B,C**). We also tested if the Penk+ and Penk- MLIs acquired a different representation in response to increased sensory drive during long stimulation, but did not find a significant difference between the two cell types (**Suppl. Figure III8.2**). Furthermore, the width of the MLI Ca^{2+} responses to long puff stimulation did not correlate with the corresponding whisking duration ($r = -0.26$, $R^2 = 0.06$; **Figure III8 C**), similar to what has been observed for the short puffs (**Figure III7 E**). This result suggests that the width of puff-evoked MLI Ca^{2+} transients is driven primarily by the sensory duration of somatosensory stimuli.

Therefore, increasing stimulus duration, and effectively the duration of somatosensory input, prologues Ca^{2+} responses, perhaps overwriting depth-dependent differences in motor representations during short stimulation. The persistent duration sensitivity throughout molecular layer lamina is consistent with a homogenous spatial representation of somatosensory stimuli, despite the robust laminar dependence of MLI response onset delays.

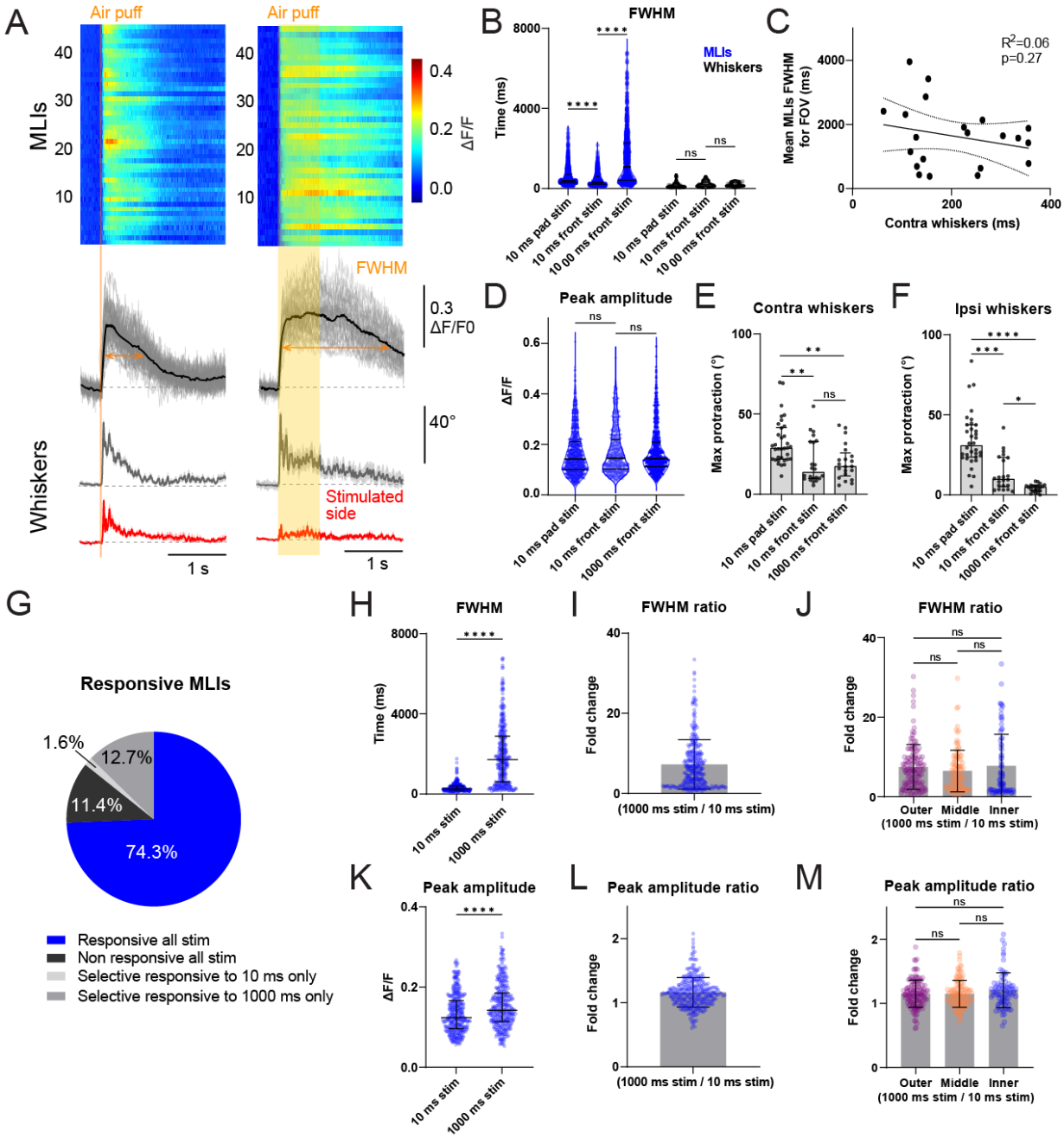

Figure III8. Prolonged Ca^{2+} activity in response to increased stimulus durations

(A) *Left*: Trial-averaged GCaMP8f Ca^{2+} activity measurements for a FOV (*top*) and traces (*middle*) with superimposed mean (black) and trial-averaged contralateral (*grey*) and ipsilateral (*red*, stimulated whiskers) whisker traces (*bottom*). Orange line represents the stimulus timing (front, 10 ms, 5 psi). *Right:* Cells from the same FOV as on the left panel during same-intensity stimulation with longer duration (1000ms), showing prolonged Ca^{2+} responses.
(B) Summary plot of the FWHM of puff-evoked Ca^{2+} activity of MLIs (*blue*) and contralateral whisker protraction (*black*) during different stimulation protocols, *10 ms pad stimulation* (20 psi, n = 1068 cells, 34 FOVs, 7 mice), *10 ms front stimulation* (5 psi; n = 583 cells, 22 FOVs, 7 mice) and *1000 ms front stimulation* (5 psi; n = 646 cells, 21 FOVs, 6 mice), respectively, showing increased widths of Ca^{2+} responses when increasing stimulus strength or duration (****p < 0.0001; ns p > 0.99; Kruskal-Wallis with Dunn's multiple comparisons test). Error bars are median with IQR.

(C) Cross-correlation of the FWHM of the cell-average Ca^{2+} traces in each FOV vs whiskers (r = -0.25; Spearman's rank correlation). Linear fit line with 95% CIs.
(D) Summary plot of the peak amplitude of Ca^{2+} activity of MLIs from (B) showing no significant change in amplitude of Ca^{2+} responses when increasing stimulus strength or duration (ns p > 0.99; Kruskal-Wallis with Dunn's multiple comparisons test). Error bars are median with IQR.
(E) Summary plot of the maximal protraction angle of contralateral whiskers from (B) showing significantly stronger protraction angles for higher intensity stimulus (20 psi vs 5 psi), but not duration (10 ms vs 1000 ms) (10 ms pad vs 10 ms front stim: **p = 0.001; 10 ms pad vs 1000 ms front stim: **p = 0.003; ns p > 0.99; Kruskal-Wallis with Dunn's multiple comparisons test). Error bars are median with IQR.
(F) Same as in (E), but comparing ipsilateral whiskers (stimulated side) (*p = 0.04; ***p = 0.0002; ****p < 0.0001; Kruskal-Wallis with Dunn's multiple comparisons test). Error bars are median with IQR.
(G) Pie chart showing quantification of MLIs responsiveness to short and long front stimulation (n = 448 cells, 11 FOVs, 3 mice)
(H) Summary plot of the FWHM Ca^{2+} activity of responsive MLIs in (G) to short and long front stimulation (****p < 0.0001; Wilcoxon matched-pairs signed rank test). Error bars are median with IQR.
(I) Summary plot showing the distribution of FWHM ratios for the MLI responses in (H). Error bars are mean with SEM.
(J) Same as in (I) but comparing the FWHM ratios for MLIs at their corresponding depth in the outer (n = 131 cells), middle (n = 120 cells) and inner (n = 82 cells) ML, respectively (outer – middle: ns p = 0.43, outer – inner: ns p = 0.29; middle – inner: ns p >0.99; Wilcoxon matched-pairs signed rank test). Error bars are mean with SEM.
(K) Summary plot of the peak amplitude Ca^{2+} activity of responsive MLIs in (G) to short and long front stimulation (****p < 0.0001; Wilcoxon matched-pairs signed rank test). Error bars are median with IQR.
(L) Summary plot showing the distribution of peak amplitude ratios for the MLI responses in (K). Error bars are mean with SEM.
(M) Same as in (L) but comparing the peak amplitude ratios for MLIs at their corresponding depth (outer – middle: ns p > 0.99, outer – inner: ns p = 0.72; middle – inner: ns p = 0.40; Wilcoxon matched-pairs signed rank test). Error bars are mean with SEM.

III9. Ca^{2+} responses amplitudes to spontaneous whisking are smaller and well correlated with whisker maximal protraction

MLIs have been shown to linearly encode the kinematics of spontaneous volitional whisker deflection (Chen et al., 2017). In order to examine the MLI response sensitivity to whisker deflection in isolation and in the same cells in which puff-evoked responses were measured, we investigated MLI Ca^{2+} response during spontaneous volitional whisking. In the same cells we compared stimulated responses during brief whisker pad stimulation (20 psi, 10 ms) with the average Ca^{2+} responses of the same MLIs during spontaneous whisking (**Figure III9 A, Suppl 9.1 A**). The example experiment shows that many cells respond to both somatosensory and whisking stimuli. The peak whisk deflection is indeed slightly smaller and importantly, the ratio between the amplitude of the evoked and spontaneous Ca2+ response is highly variable (**Figure III9 A,D)**, suggesting a variability in the sensorimotor representations. Chen et al (2017) previously reported increasing and decreasing changes in MLI firing rates, tuned to whisker movement kinematics. We too observed reliable Ca^{2+} responses during spontaneous whisking in 59.2% of the MLIs recorded (n = 136 MLIs, 3 FOVs, 2 mice; **Figure III9 B**). However, we did not detect any decreasing Ca^{2+} transients. One explanation may be that because the decreasing firing rates previously observed were 10-fold smaller compared to the increasing cases (Chen et al., 2017), those changes might be undetectable with Ca^{2+} imaging.

Air puff stimulation recruited an additional 36.3% of MLIs (**Figure III9 B**), suggesting that MLIs responding only to somatosensory stimuli comprise one third of the population of the MLI responses. When comparing the Ca^{2+} responses to evoked and spontaneous whisking, 94% of cells exhibit smaller peak amplitudes for spontaneous whisking (30% decrease on average; **Figure III9 C,D**). The maximum whisker angle deflection in spontaneous bouts are smaller (**Figure III9 E**), which might partially explain the smaller amplitudes in Ca^{2+} activity across FOVs. To examine the influence of whisker angle more specifically, we compared the Ca^{2+} response peak to the mean maximum deflection angle (**Figure III9 F,G; Suppl. Figure III9.1 B,C**). For spontaneous whisking, we found that the Ca^{2+} response amplitude is strongly correlated with the corresponding maximal protraction angle mean between both whisker sides during spontaneous whisking ($r = 0.69$, $R^2 = 0.7$, n = 15 FOVs, n = 6 mice; **Figure III9 G, Suppl. Figure III9.1 C**), but not in response to air puff stimulation ($r = -0.25$, $R^2 = 0.01$, n = 34 FOVs, n = 7 mice; **Figure III9 F, Suppl. Figure III9.1 B**). Interestingly, over the same

range of maximum deflection angles, only the spontaneous whisking shows a correlation with Ca^{2+} response amplitude. These results suggest that although MLIs can encode both somatosensory and motor information, when a sensory stimulus evokes whisking, the representation is biased towards somatosensory representations.

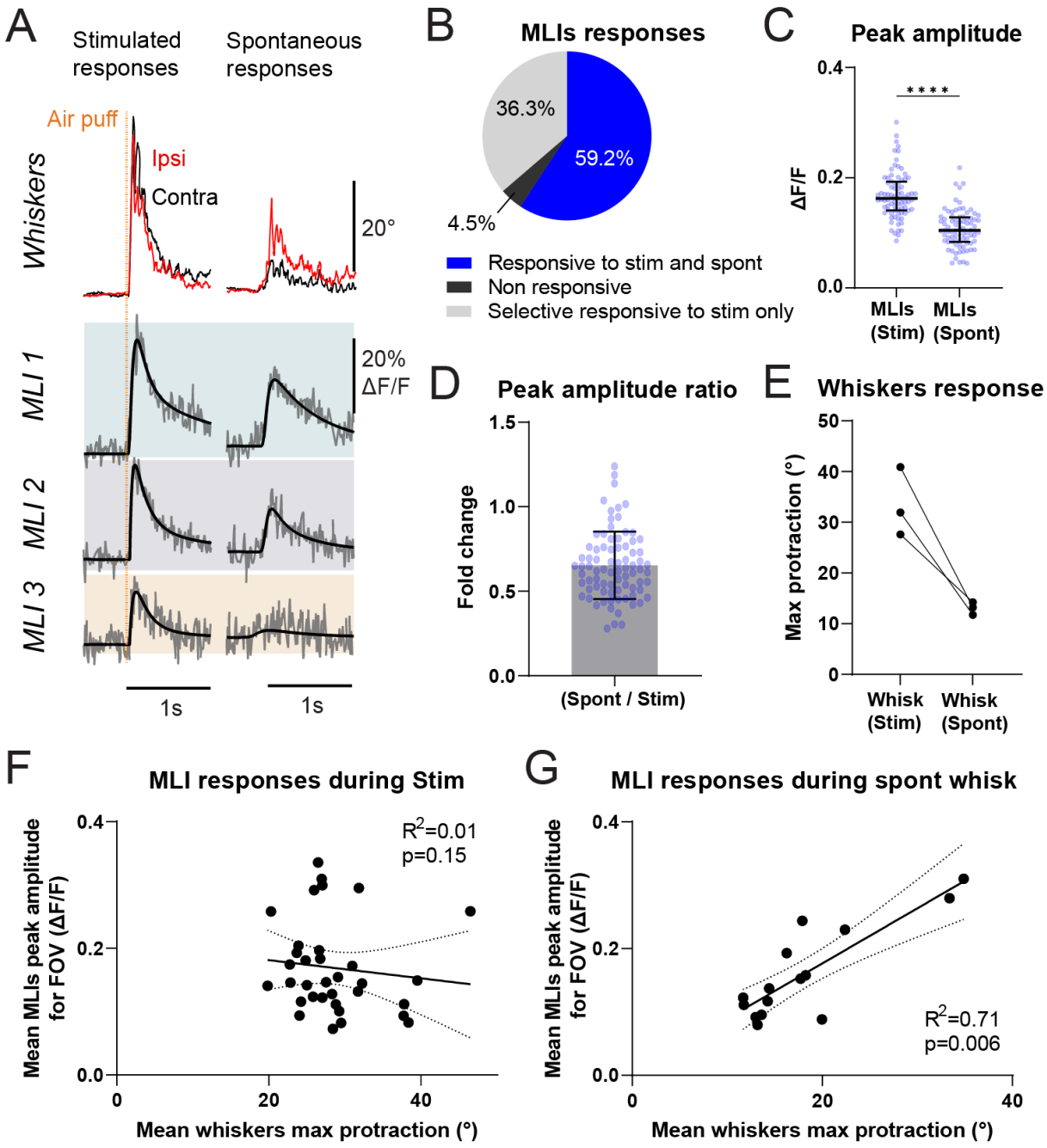

Figure III9. Smaller and movement-correlated Ca^{2+} responses amplitudes during spontaneous whisking

(A) *Left:* Trial-averaged traces of puff-evoked (10 ms, 20 psi) whisker deflection (upwards indicates protraction) and of Ca^{2+} traces of three MLIs imaged at 100Hz (*grey*) with the superimposed exponential fits (*black*). *Right:* Cell-matched Ca^{2+} traces during spontaneous whisking.
(B) Pie chart showing quantification of MLIs responsiveness to puff-evoked and spontaneous whisking (n = 80 cells, 3 FOVs, 2 mice).
(C) Summary plot of the peak amplitude Ca^{2+} activity of responsive MLIs in (B) puff-evoked and spontaneous whisking (****p < 0.0001; Wilcoxon matched-pairs signed rank test). Error bars are median with IQR.
(D) Summary plot showing the distribution of peak amplitude ratios for the MLI responses in (C). Error bars are mean with SEM.

(E) Summary plot of the maximal angle of protraction of the same-session puff-evoked and spontaneous whisking.
(F – G) Cross-correlation of the peak amplitude of the cell-average Ca^{2+} traces in each FOV vs whiskers maximal protraction angle for puff-evoked (n = 34 FOVs; r = -0.25) and spontaneous (n = 15 FOVs; r = 0.69) whisking. Spearman's rank correlation. Linear fit line with 95% CIs dashed black line.

Discussion

It was previously shown that MLIs encode spontaneous whisker movement (Chen et al., 2017) and can generate sensory-evoked responses to whisker stimulation (Chu et al., 2012). *In vivo*, MLIs can acquire a coherent behavioural representation important for the accurate generation of motor actions (Astorga et al., 2017; Gaffield et al., 2018; Gaffield & Christie, 2017; Rowan et al., 2018). Both *in vitro* and *in vivo* evidence suggest that MLIs are a heterogeneous population (Kozareva et al., 2021) and have a depth-dependent functional organization (Alcami, 2018; Chu et al., 2012; Hoehne et al., 2020; J. Kim et al., 2014). However, it is not clear how their responses might differ during sensorimotor representations of behaviour.

Here we examined their laminar representation during sensory-evoked whisking and how those sensorimotor representations are altered by different sensory-stimulation protocols. Our findings indicate that MLIs in Crus I acquire a widespread coherent representation of whisker kinematics, in line with previous observations regarding licking in the adjacent region Crus II (Astorga et al., 2017; Gaffield & Christie, 2017). Moreover, MLIs exhibit a depth-dependent representation of sensorimotor variables (**Figure III1-2**), with increasingly smaller peak amplitudes of Ca^{2+} responses deeper in the molecular layer. Inner MLIs also show a significantly higher degree of rapid sensory responses, that precede behaviour in a proportion of over 70% in middle to inner molecular layer (**Figure III2,7**). Those rapid response patterns are reminiscent of the faster sensory-induced excitatory postsynaptic currents in MLIs with increasing depth in anaesthetised mice (Chu et al., 2012). Penk-expressing basket-like MLIs exhibit similar depth-dependent differences (**Figure III3,4**). With a larger range diversity, PF show a similar pattern of response onset delays in depth, pointing towards an input driven diversity of response initiation in MLIs (**Figure III5**).

With regards to behavioural representations, MLIs across layers encode somatosensory and whisker kinematic information with variable response duration depending on the sensory drive. The time-to-peak of slow-onset MLIs correlate stronger on average with that of whiskers (**Figure III7**), suggesting that cells that respond after whisker movement is initiated are most likely representing proprioceptive or movement related parameters. Moreover, a 100-fold increase in sensory duration drives prolonged MLI responses that exceed stimulus duration and whisking to a great extent (**Figure III8**). Finally, during self-initiated whisking the Ca^{2+} response amplitudes of MLIs are smaller and better correlated with the maximal protraction of

the whiskers, in comparison with sensory-evoked representations (**Figure III9**). This suggests a differential representation depending on magnitude of somatosensory and motor or proprioceptive variables, as highlighted by puff-evoked responses of different magnitudes (short vs long stimulation) and non-stimulated (spontaneous) responses, respectively.

Within the context of the cerebellar circuitry, there are both external factors and intrinsic properties that influence to a varying extent the laminar distribution of MLI responses observed during sensory-evoked whisking. Although the current work does not test the mechanisms that causally drive the heterogeneous responses, we examined if 1) intrinsic differences marked by the *Penk1* gene (**Figure III3,4**), or 2) external input patterns from PFs, could relate and possibly explain those differences (**Figure III5**).

1. Penk1 expression as a marker for putative basket cells

Penk-expression was seen to mark a separate transcriptional cluster of MLIs (unpublished, Jason Christie Laboratory). By comparison, within the functional classes of MLIs proposed by Kozareva et al. (2021), the *Penk1* gene is exclusively expressed in MLI1 group (and GoCs outside the molecular layer), which corresponds to the same class incorporating all the electrically coupled MLIs (**Figure III3**). Our morphological analysis shows that Penk-positive cells have basket terminals. They are also increasingly more prevalent with depth, while gap junction coupling is also more common in BCs (Hoehne et al., 2020; Rieubland et al., 2014). Together, these results suggest a link between Penk-positive MLIs and electrical connectivity. Permitting the direct propagation of current, electrical connectivity has been previously linked to stronger and temporally precise spike timing (Hoehne et al., 2020; J. Kim et al., 2014). It was therefore surprising that Penk-positive and negative MLIs followed very similar patterns of response to sensory-evoked whisking (**Figure III4**).

While Penk-positive MLIs did not seem to have distinctive sensorimotor representations apart from simple depth dependence (**Figure III4, Suppl. Figure III8.2**), electrical connectivity and basket-like terminals in this subpopulation might still be important for differentia controlling of PC firing rates. a direct assessment of the degree of electrical coupling between Penk-positive compared to Penk-negative cells might be required, to determine the proportion of electrically coupled Penk-positive MLIs form separate subgroups of the MLI1 transcriptomic type, which itself shows within heterogeneous marker expressions (Kozareva et al., 2021). Given these heterogeneous responses of MLIs during sensorimotor integration, a closer look at the link between multiple transcriptomic classes and functionality might provide

better insight into their differential mechanisms of information processing. For example, a similar analysis used imaging coupled with ex vivo scRNA-sequencing to reveal differential behavioural encoding in molecularly defined classes of hypothalamic neurons (Xu et al., 2020).

2. Penk1 expression as a mechanism for unique MLI function

The current study identified the *Penk1* gene as a marker for putative basket cells, which do not have a distinguishable sensory-motor representation as compared to their layer Penk1-counterparts. It could also be important to consider the purpose of the gene expressed in a subset of MLIs and with a higher prevalence in the inner molecular layer. The *Penk1* gene encodes for the precursor protein proenkephalin to the enkephalins opioid peptides (Kieffer, 2009). Within the central nervous system, enkephalins are neuromodulators highly expressed in areas such as the amygdala and striatum, with an important role in pain regulation, but also emotional and cognitive functions (Bodnar, 2022; Kieffer, 2009; Wilson & McDonald, 2020). With this in mind, the expression of proenkephalin in the subset of Penk-positive MLIs might indicate towards their differential role in regulating pain and emotional perception. Indeed, there is a growing consensus that the cerebellum is involved in cognition and reward signalling (reviewed in Kostadinov & Häusser, 2022; Wagner et al., 2019). Moreover, MLI function has been specifically linked to affective and social related functions (Badura et al., 2018; Y. Liu et al., 2010; Ma et al., 2020). Meanwhile, other neuromodulators such as norepinephrine can bind to b-adrenergic receptors to actively increase the firing rate of MLIs and shape emotional learning (Kondo & Marty, 1998a; Y. Liu et al., 2010). As a consequence, the neutral behavioural paradigm of evoked whisking used here, might be unsuited to trigger the specific role or Penk-positive MLIs (**Figure IIII4**). Studying the function of proenkephalin modulation in MLIs might need a reward based or fear conditioning task. It is possible that selectively manipulating Penk-expressing MLIs through chemogenetic or optogenetic means, might pinpoint towards novel mechanisms of affective perception in the cerebellum. Therefore, even though the current work does not support the hypothesis that Penk-positive MLIs differ functionally from Penk-negative ones, assessing if the Penk gene marks a segregated functional subpopulation of MLIs in more complex tasks involving affective perception, merits further investigation.

3. Diversity of MLI intrinsic and input integration properties

MLIs show gradually smaller amplitudes and faster onset of Ca^{2+} responses with increasing depth that are consistent across different stimulation types, suggesting an implicit mechanism underlying this laminar effect (**Figure III1**, **Suppl. Figure III8.1**). In line with our findings, air puffs to the whiskers of anaesthetised mice induce sensory-evoked temporally faster and narrower excitatory postsynaptic currents in MLIs with increasing depth (Chu et al., 2012). Meanwhile, MLIs have comparable spontaneous firing patterns *in vivo* and *in vitro* (Chen et al., 2017; Häusser & Clark, 1997; Jirenhed et al., 2013; Ruigrok et al., 2011), which were previously reported to be similar throughout the molecular layer (Häusser & Clark, 1997). Those patterns are however diverse, ranging from $\sim 1 – 35$ Hz *in vivo* (Jirenhed et al., 2013; Ruigrok et al., 2011), suggesting that the intrinsic mechanisms regulating firing patterns have a consistent diversity throughout the molecular layer. This is reminiscent of the continuum in morphology and gene expression of MLIs (Kozareva et al., 2021; Sultan & Bower, 1998; W. X. Wang & Lefebvre, 2022). Thus, the diversity of responses seen within each layer could correspond to those intrinsic heterogeneities.

MLIs sample multiple PFs inputs with somas at corresponding depths in the GC layer (Espinosa & Luo, 2008; Zong et al., 2005). Although the dendritic tree of MLIs can span different depths (W. X. Wang & Lefebvre, 2022), it has previously been shown that the strength of synaptic inputs increases with proximity to the soma of MLIs (Abrahamsson et al., 2012). It is therefore likely that PF inputs arriving at a similar location to the MLI soma, influence the output of the MLIs to a greater extent. Because GCs *in vitro* show a laminar distribution in their responses to low- and high-frequency inputs, with a preference for the latter in inner- GCs (Straub et al., 2020), we considered that the depth-dependence differences of MLI responses could be driven by the layer-corresponding GCs inputs (**Figure III5**). Concurrently, a layered diversity in the sensory information incoming through PFs (Straub et al., 2020) might generate some of the depth-dependent differences seen during sensory-evoked responses (Chu et al., 2012). In the inner MLIs the effect of gap junctions might be congruent with the layer-dependent GC input (Straub et al., 2020) and, as such, contribute to assimilate this fast PF excitation appropriately (Alcami, 2018). In this case a direct manipulation of gap junctions might provide more insight into the role of electrical connectivity.

4. Diversity of granule cell PF representations as a source for MLI response diversity

Following a similar trend to MLI responses, our results show that PFs also have significantly more rapid-onset responses to whisker stimulation deeper in the molecular layer (**Figure III5**). Although GCs receive multisensory information from multiple MFs that span the entire GC layer (Chabrol et al., 2015; C.-C. Huang et al., 2013; Markwalter et al., 2019; Shuster et al., 2021), they might preferentially integrate this information in a layer-dependent manner (Straub et al., 2020; W. Zhang & Linden, 2012). The higher prevalence of rapid responses seen in inner- MLIs might therefore be explained by the tuning of inner- GCs to higher frequency input and a faster conductance and synaptic properties as expected by the larger diameters of inner-PFs and their boutons (Eccles et al., 1967; Pichitpornchai et al., 1994; Straub et al., 2020; W. Zhang & Linden, 2012). As a PF can extent as far as 2 mm in length in mice (Huang et al., 2006), those propagation properties might become particularly important for distal synapses on the PF.

We also find that MLIs onsets of response are on average faster and temporally less diverse than their layer corresponding PFs, possibly because MLIs sample and average over the input of multiple GCs (**Figure III5**). Their early response may therefore reflect the integration of the initial fast-onset GCs. Considering the strength and latency of MLIs responses depends on the location of the synapse (Abrahamsson et al., 2012), it would be interesting to test if fast- and slow-onset PFs are preferentially oriented on more proximal or distal MLI dendrites.

However, as fast-onset PF responses are present throughout the depth of the molecular layer, it is possible that inner MLIs have a more efficient method of integrating this input and trigger synchronous activation in response to the earlier-onset PFs. A similar mechanism has been previously reported for electrically coupled GoCs, that can compensate for subthreshold dendritinc integration through gap junction mediated direct propagation of excitatory flow (Vervaeke et al., 2012). In MLIs, electrical coupling was also seen to enhance and accelerate interneuron recruitment in response to excitatory input (Alcami, 2018). Therefore, it is probable that few fast PFs can induce a faster and stronger widespread recruitment of MLIs with increasing depth. Moreover, the PF input was shown to be spatially clustered (Wilms & Häusser, 2015), and depending on their dendritic span and location, some MLIs might receive a higher convergence of excitatory PF input during whisker stimulation. To this too, electrical connectivity might help spread on the parasagittal plane the sensorimotor information clustered

in transversally running axonal beams (J. Kim et al., 2014). This direct propagation may therefore result in a net increase in excitatory drive with inner MLIs.

One possibility is that a strong sensory input (produced by the 20 psi air-puff to the whisker pad) favours the information provided via the MF-GC pathway and therefore it is not surprising that the MLI activation follows the rules of this information flow (**Figure III5**). In this case, the sensory drive provided might further overwrite some of the intrinsic processing specific to functional subsets of MLIs. Separately, MLIs were shown to widely encode information regarding both whisker kinematics during spontaneous whisking (Chen et al., 2017) as well as sensory-evoked responses under anaesthesia (Chu et al., 2012). In our recordings, the average response amplitude of MLIs is significantly correlated to the maximal protraction of the whiskers only during self-initiated whisking, but not during sensory-evoked protocols (**Figure III9**). This further emphasises that movement kinematics are preferentially encoded only in the absence of the sensory drive, reinforcing an overwriting stimulus effect. Nevertheless, it cannot be ruled out that more mild forms of sensory stimulation might provide a balanced encoding of sensory and motor variables. For example, differences of MLIs responses have been previously observed between bruxing and licking behaviours, in which only the latter behaviour induces a coherent activity on the coronal plane as expected during a PF driven sensorimotor input (Astorga et al., 2017).

Furthermore, the specificity of MLI subtypes might be of importance in more engaging and decisional tasks such as associative learning, for which MLIs are known to be important (Bonnan et al., 2023; Ma et al., 2020; Rowan et al., 2018). Related to whisking, adaptation of PCs simple spikes follows regular air puff induced whisking (Romano et al., 2018; Zempolich et al., 2021), probably through anticipation of the stimulus. As this PCs activity is induced by GCs input and mediated by MLIs, it would be interesting to see if similar adaptations can be observed in MLI activity, especially in the early sensory response during which MLI activation strongly inhibits PCs responses (Chu et al., 2011, 2012).

5. Influence of climbing fibre synapse and inhibitory drive on MLI representations

As chemogenetic inhibition of GCs does not completely ablate MLIs responses to air puffs (Gaffield et al., 2019), other mechanisms besides GCs input must be considered as contributing factors to the resulting MLI response dynamics. Particularly, indirect spillover from CF-PC synapses can engage MLIs during sensory processing (Arlt & Häusser, 2020; Szapiro & Barbour, 2007). Also, MLIs receive direct inhibition from PCs, Lugaro cells, CCs

and other MLIs (Kondo & Marty, 1998a; Mittmann et al., 2005; Miyazaki et al., 2021; Osorno et al., 2021; Witter et al., 2016). Inhibition from MLIs and PCs is more prevalent with depth (Lemkey-Johnston & Larramendi, 1968b). If anything, in the current work we see some longer activation windows in mostly deeper MLIs (**Figure III1**), suggesting that this inhibition does not promptly shorten their response. It is however a possibility that inhibitory input contributes to decreasing the frequency of MLI firing rate, which would translate into the smaller amplitudes of Ca^{2+} responses seen with increasing depth. Also, additional work would be needed to assess the spatial organisation and functional implications of the inhibition from PLIs. The interplay between the CF activation of MLI within the range of spillover and their lateral inhibition of other MLIs could further segregate the duration of their sensory-induced responses (Coddington et al., 2013). This could lead to the particularly long-lasting Ca^{2+} responses of MLIs in the CF spillover range and the narrow responses of the ones inhibited by those MLIs. However, further investigation would be needed to understand the impact of CF to MLIs spillover during behaviour and the way inhibition sculpts the temporal patterns of MLI responses.

6. Spatial distribution of sensorimotor information and GC-MLI transformations

In the cerebellum, there is a high convergence of whisker-related MFs pathways carrying sensory and motor information at different levels of processing (Bosman et al., 2011). As such, air puff stimulation to the whiskers is known to highly engage MLIs (Chu et al., 2012) and in general cerebellar neurons (Arlt & Häusser, 2020; Bosman et al., 2010; S. T. Brown & Raman, 2018; Chu et al., 2011; Romano et al., 2018). Previous findings show that the sensory input engages MLIs in a proportion of ~80% (29 out of 36 MLIs) in anaesthetised mice (Chu et al., 2012). Similarly, in our study, this sensory drive reliably induced a widespread activity of MLIs (**Figure III1**), in awake mice, that precedes whisking to a high extent. Although the initial response preceded whiskers in many MLIs responding to air puff stimulation (**Figure III2,7**), the time-to-peak for a given FOV correlates with the whisker time of maximal deflection, and even more so for cells responding after the initiation of the whisking. The different delays in response raise the question of whether those slower-onset MLIs are more likely driven by whisker kinematics and less by the initial sensory-input, as suggested by their stronger correlation of time-to-peak with the maximal whisker protraction. Our data therefore supports a possible motor drive in the later part of the MLIs responses, especially in the subset of slow-onset MLIs (**Figure III7**). This was previously suggested by responses in PCs, which

share the same GCs information with MLIs. As such, the later part of the PCs responses were previously linked with the rhythmic whisking-related motor commands relayed from MFs originating in the brainstem (Kleinfeld et al., 2014; Takatoh et al., 2013), and temporally separated from the initial ~50 milliseconds of the response likely incoming directly from the trigeminal nucleus (S. T. Brown & Raman, 2018).

In fact, when stimulating the whiskers of anaesthetised mice in which the motor response is removed, the latency of response does not differ much between MLIs and between outer- and inner- cells (Chu et al., 2012). Meanwhile, our findings in awake mice suggest that during short stimulation protocols, the FWHM of a small proportion of cells can last for over a second with a higher prevalence in the inner layer, reinforcing a stronger motor related component in the later response (**Figure III1**). Nevertheless, increasing stimulus duration induced long lasting activation over a few seconds in over half of the MLIs recorded, that outlasted whisking (**Figure III8**). This effect was seen across the depth of the molecular layer, reflecting a strong sensory drive of a sustained whisker stimulation that could perhaps overwrite the laminar differences of the MLIs response latencies seen during short stimulation protocols. This long lasting activation might be related to the strong convergence of the cortico-pontine MF pathways relaying information from the primary and secondary sensory cortices (Leergaard et al., 2004) that favour sensory processing in the cerebellum (Bosman et al., 2011). At the input level to MLIs, GCs integrate different sensory modalities to various extents, possibly creating a somatosensory gradient in their temporal dynamics, that is further relayed to MLIs (Ishikawa et al., 2015). Furthermore, the response of GCs has been divided into a short-latency initial component and a second longer latency component, following facial stimulation (Morissette & Bower, 1996). As seen for PCs (S. T. Brown & Raman, 2018), the first component was shown to be generated by the direct trigemino-cerebellar pathway. Meanwhile, input from the primary sensory cortex is primarily responsible for this long latency secondary component, suggesting that the diversity in MLIs temporal dynamics might be explained by the integration of temporally divided MFs pathways.

In another cerebellar region, a similar widespread activity of MLIs has been observed in response to motor tasks such as licking (Astorga et al., 2017; Gaffield & Christie, 2017), while responses to spontaneous whisking in MLIs have also been reported (Chen et al., 2017). Our data supports that about 60% of MLIs can encode both sensory-evoked and self-initiated whisking (**Figure III9**). However, without the sensory drive, responsiveness to the same group of MLIs during self-initiated whisking is reduced to half, while the peak amplitude of

spontaneous are smaller for the same cells. Given that the angle of protractions are significantly smaller during exploratory whisking compared to sensory-evoked, the spiking frequency of MLIs in response to self-initiated whisking might in fact be adjusted to the sensory drive or whisker protraction angle. Indeed, unlike in sensory-evoked whisking, during spontaneous whisking there is a significant correlation between the average population peak amplitude of Ca^{2+} responses and the mean maximal protraction between both whisker sides (**Figure III9**). This further highlights that at a population level, MLIs encodes both ipsilateral and contralateral movement related changes. Consequently, this diversity of MLI responses might contribute to disambiguating the information processing of sensory and motor variables from GCs to PCs with high temporal precision of neuronal activity, important for well-timed cerebellar behaviours (Cayco-Gajic & Silver, 2019; Jelitai et al., 2016; Mittmann et al., 2005).

7. Implications of laminar MLI sensorimotor representations for cerebellar processing

The stimulation protocol used was previously shown to recruit PCs in a temporally precise manner and also engage DCN neurons at the output of the cerebellar communication (Brown & Raman, 2018). Our study was able to show that the onset delays of MLI responses to whisker stimulation are shorter in the inner MLIs as opposed to outer ones (**Figure III1,2**), similar to the sensory-evoked MLI patterns of excitatory postsynaptic currents (Chu et al., 2012). Importantly, our findings link MLIs activity *in vivo* to the previously observed stronger and faster inhibition of PCs with increasing depth (Arlt & Häusser, 2020).

Our work also suggests that MLIs acquire this laminar effect from GCs (**Figure III5**), integrating their collective input and responding within milliseconds after the stimulus, with faster onsets in the deeper molecular layer. This increasingly faster FFI inhibition by inner MLIs is important to narrow the time window of integration of PF input to PCs (Mittmann et al., 2005), and promote their synchronous firing by fast ephaptic coupling (Han et al., 2018; Wise et al., 2010). It is therefore possible that the laminar effect observed in our work acts to sculpt the temporal patterns of PCs needed generate the appropriate behaviour (Arlt & Häusser, 2020; De Solages et al., 2008; Lindeman et al., 2021; Person & Raman, 2012). Therefore, the laminar gradients in temporal delays and inhibition strength of MLIs could shape in a similar fashion the PCs synchrony in pauses and temporal integration of PF relayed sensorimotor variables. By doing so, MLIs might have a key role in modulating the output of the cerebellar cortex.

8. Limitations of methodology

The mechanisms interrogated in the current work have temporal features on scales of under or a few milliseconds (Arlt & Häusser, 2020; S. T. Brown & Raman, 2018; Chen et al., 2017; Chu et al., 2012) and measure population wide activity (Astorga et al., 2017; Gaffield & Christie, 2017). To balance the trade-off between spatial and temporal resolution, we used the fast calcium indicator probe GCaMP8f (Y. Zhang et al., 2023) and fast resonant scanning imaging at 100 Hz of FOVs comprising tens of MLIs at once. Nevertheless, interpretations must be made with caution especially with respect to early features of the response. Even the fast kinetics of GCaMP8f with rise times of only about 3 milliseconds are an indirect and slow measure of single action potentials. For example, under a similar stimulation protocol, BCs provide perisomatic inhibition to PCs within 1 millisecond *in vivo* (Chu et al., 2012), while the transient inhibition of PCs lasts only ∼15 milliseconds (Zempolich et al., 2021). With respect to temporal precision, the limiting factor in our experiments is however the image acquisition time of 10 milliseconds for each time point. Our onset of response as measured by a 10% rise time of Ca^{2+} transients exponential fits, temporally matches peak response rates of our electrophysiological measures (**Suppl Figure III2.1**) and are comparable with the sensory induced peak spike responses in MLIs at an average of ∼20 milliseconds (Chu et al., 2012). This suggests that our approach was at the limit of detecting such subtle temporal differences.

Sometimes Ca^{2+} activity measurements using imaging techniques can introduce noise that may overshadow small transients and induce spurious correlations (Diana et al., 2019). Detecting small Ca^{2+} transients accurately is particularly important for neurons with high Ca^{2+} buffering such as MLIs (Collin et al., 2005). We prioritised response confidence by excluding low signal-to-noise activity to minimize faulty estimates. Unfortunately, it is possible that our interpretation of MLIs responsiveness is an underestimation, especially with regards to spontaneous activity which induced smaller transients. With increasingly improving tools of spike inference from Ca^{2+} activity tailored to the specificity of the probe used, a further analysis of extracted spiking patterns could provide additional insight into the temporal responses of neurons (Diana et al., 2019; Li et al., 2021; Rupprecht et al., 2021). Nevertheless, our study provides a temporal advantage to previous imaging studies of MLIs at slower rates of 30 Hz (Astorga et al., 2017; Gaffield & Christie, 2017) that enabled us to determine differences in fast onsets of response profiles (**Suppl. Figure III1.1**). Further investigation using direct electrophysiological recordings with Neuropixels probes coupled with optotagging techniques, could provide a powerful and well-suited tool to interrogate fast synchrony of MLIs and effects

on PCs activity (Jun et al., 2017; J. Kim et al., 2014) thus increasing the richness of information carried by cells responding on very short time scales.

Supplementary figures

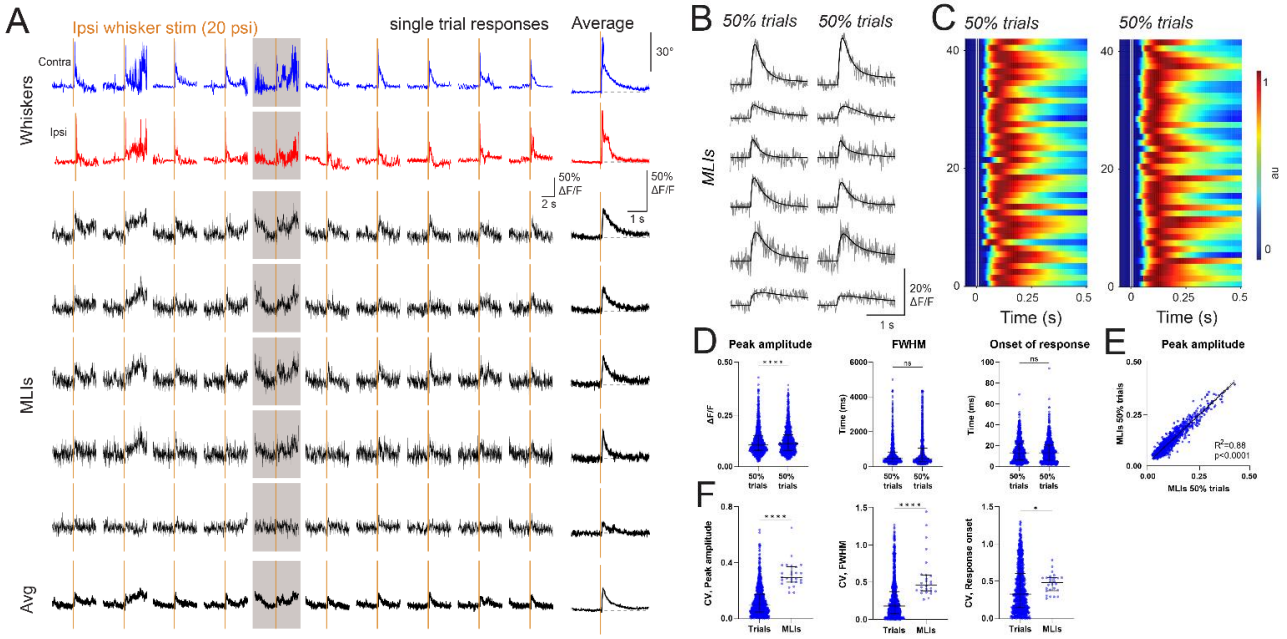

Supplementary Fig.III1.1. Ca^{2+} activity response variability across trials

(A) Example single-trial responses of whisker deflection (upwards indicates protraction, *blue* – contralateral, *red* - ipsilateral) and of GCaMP8f Ca^{2+} traces of five MLIs imaged at 100Hz (*black*). Bottom traces represent cell-averaged responses. Right traces represent the trial-average responses. Orange dashed line represents the stimulus timing. Grey shading marks excluded trial for whisking at stimulation onset (see section II Methods).
(B) Average Ca^{2+} traces of six example MLIs across odd (*left*) and even (*right*) trials.
(C) Odd (*left*) and even (*right*) exponential fits of trial-averaged Ca^{2+} activity measurements of all responsive MLIs in the FOV presented in (A) normalized to the peak amplitude ordered by response onset, following air puff stimulation at time 0 (white line).
(D) Summary plot for peak amplitude, FWHM and response onset of puff-evoked Ca^{2+} activity of MLIs (each dot represents the trial-averaged MLI response across odd and even trials respectively, n = 890 cells), showing a similar distribution of responses (peak amplitude medians: 0.10 vs 0.11 ΔF/F, ****p < 0.0001; FWHM medians: 453 vs 442 ms, ns p = 0.09; response onset medians: 13 vs 13 ms, ns p = 0.24; Wilcoxon matched-pairs signed rank test for each group). Error bars are median with IQR.
(E) Average Ca^{2+} activity peak amplitude of individual MLIs across odd vs even trials cross-correlation with linear fit shown in dashed black line (r = 0.89, Spearman's rank correlation).
(F) Summary plots comparing the coefficient of variation (CV) of MLI responses across trials and cells in the same FOVs, for the parameters in (D), showing higher CVs (n = 890 cells, 26 FOVs; peak amplitude medians: 0.10 vs 0.29, ****p < 0.0001; FWHM medians: 0.18 vs 0.46, ****p < 0.0001; response onset medians: 33 vs 48 ms, *p = 0.02; Mann Whitney test for each group). Error bars are median with IQR.

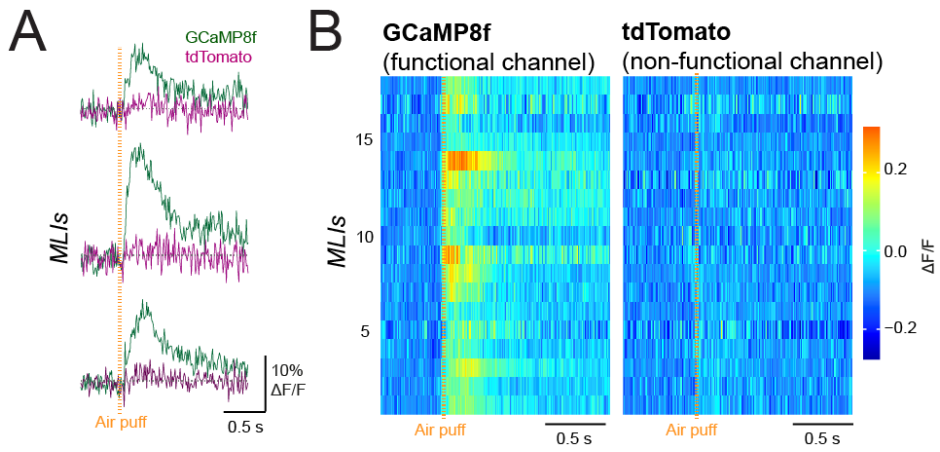

Supplementary Fig.III1.2. Movement control using Penk-Cre dependent tdTomato expression

(A) Superimposed trial-averaged GCaMP8f Ca^{2+} traces (*green*) and tdTomato traces (*magenta*) of the same cell, for three example MLIs co-expressing the functional dye GCaMP8f and non-functional dye tdTomato (*Penk1* cre-dependent expression, further addressed in section III3-4). Orange dashed line represents the stimulus timing.
(B) Trial-averaged GCaMP8f Ca^{2+} activity measurements (*left*) and of tdTomato (*right*) all MLIs co-expressing GCaMP8f and tdTomato (Penk-expressing MLIs) in the FOV. Orange dashed line represents the stimulus timing.

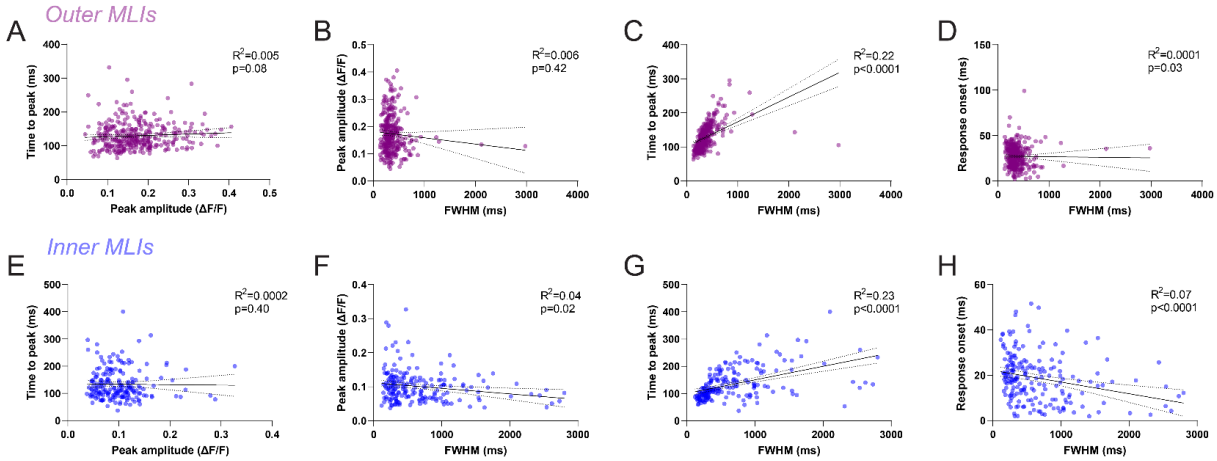

Supplementary Fig.III1.3. Correlations in Ca^{2+} activity temporal patterns

(A) Average Ca^{2+} activity of outer MLIs (each dot represents the trial-averaged MLI response; n = 315 cells, 8 FOVs, 5 mice) peak amplitude vs time-to-peak cross-correlation showing same-cell correlated responses with linear fit shown in dashed black line (r = 0.10, Spearman's rank correlation).
(B) Cross-correlation of the FWHM vs peak amplitude of same cells as in (A) with linear fit (95% CIs) shown in dashed black line (r = -0.05, Spearman's rank correlation).
(C) Cross-correlation of the FWHM vs time-to-peak of same cells as in (A) with linear fit (95% CIs) shown in dashed black line (r = 0.70, Spearman's rank correlation).
(D) Cross-correlation of the FWHM vs response onset of same cells as in (A) with linear fit (95% CIs) shown in dashed black line (r = -0.13, Spearman's rank correlation).
(E – H) Cross-correlations of the same parameters measured (A – D) for the Ca^{2+} activity of inner MLIs (n = 192 cells, 7 FOVs, 5 mice), **(E)** peak amplitude vs time-to-peak (r = -0.06), **(F)** FWHM vs peak amplitude (r = -0.17), **(G)** FWHM vs time-to-peak (r = 0.58), **(H)** FWHM vs response onset (r = -0.32). Spearman's rank correlation with linear fit (95% CIs) shown in dashed black line.

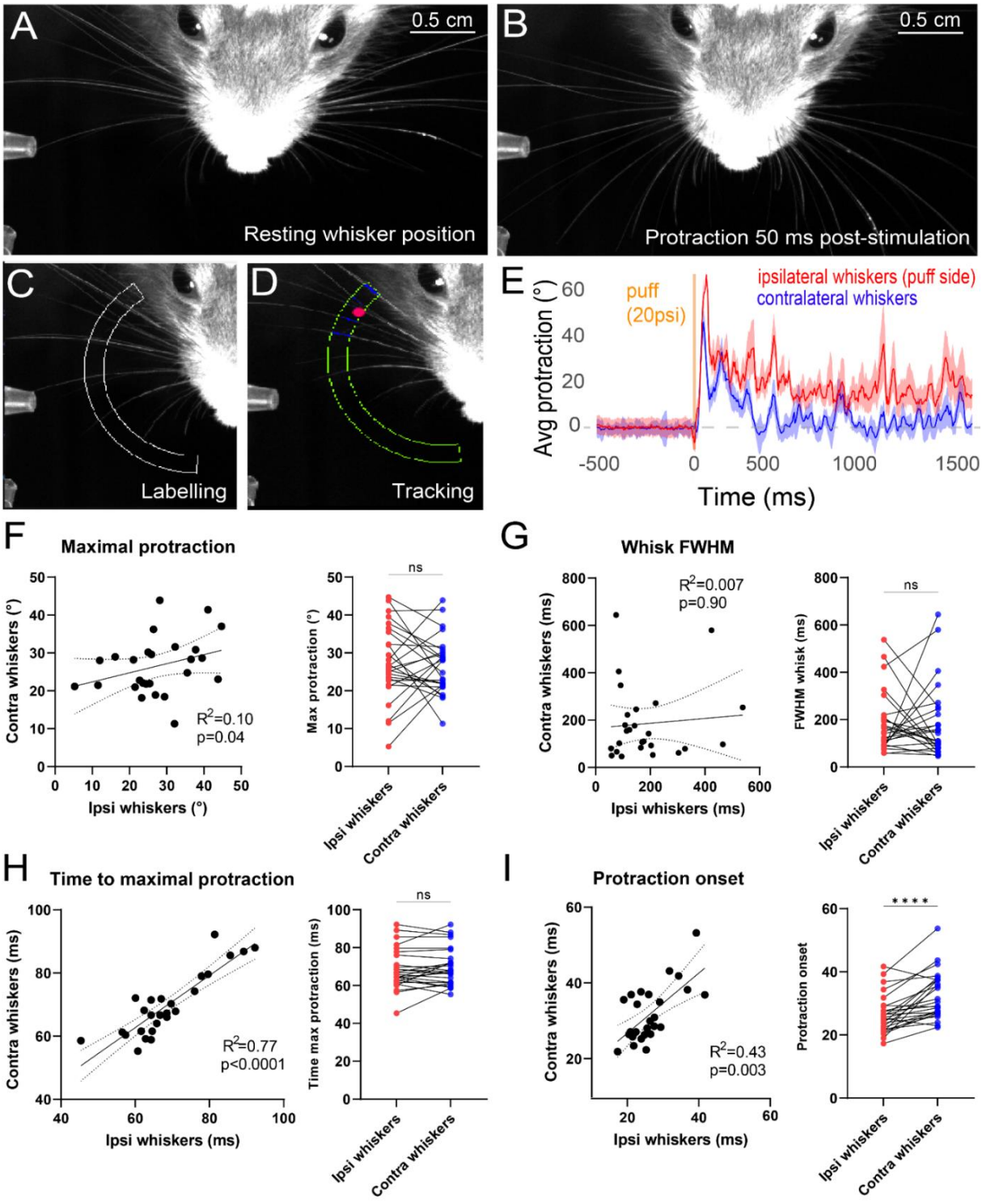

Supplementary Fig.III1.4. Lateralization of whisker movement kinematics

(A) Example videography frame of a resting and awake head-restrained mouse during imaging recordings, immediately before air-puff stimulation to the ipsilateral whisker pad. **(B)** Same as in (A), following 50 ms post-stimulation of the air-puff (10 ms, 20 psi) to the ipsilateral whisker pad to the imaging brain hemisphere. Note bilateral protraction of whiskers.
(C) Labelling the area of radial whisker movement (*white*) for the recording show in (A) (ipsilateral whiskers shown).

(D) Whisker detection (*blue*) and extraction the mean angle of deflection (*pink dot*) in relationship to the center of the whisker pad for the labelled area (*green*) in (C).
(E) Example of trial-averaged traces (n = 10 trials) normalized to the baseline resting angle of ipsilateral (*red*) and contralateral (*blue*) whiskers. Orange line represents the stimulus timing. Shading represents SEM.
(F) Comparison of maximal protraction angle of the exponential fits of trial-average ipsilateral (ipsi) vs contralateral (contra) session-matched whiskers (n = 26 sessions, up to 30 trials per session). *Left*: cross-correlation with linear fit (95% CIs) shown in dashed black line (r = 0.41, Spearman's rank correlation). *Right*: Summary plot with session-matched connecting line for corresponding ipsilateral (*red*) and contralateral (*blue*) whisker sides (ns p = 0.63; Wilcoxon matched-pairs signed rank test).
(G) Comparison of the FWHM of the same traces as for (F). *Left*: cross-correlation (r = 0.03, Spearman's rank correlation). *Right*: Summary plot (ns p = 0.88; Wilcoxon matched-pairs signed rank test).
(H) Comparison of the time to maximal protraction of the same traces as for (F). *Left*: cross-correlation (r = 0.80, Spearman's rank correlation). *Right*: Summary plot (ns p = 0.47; Wilcoxon matched-pairs signed rank test).
(I) Comparison of the protraction onset of the same traces as for (F). *Left*: cross-correlation (r = 0.57, Spearman's rank correlation). *Right*: Summary plot (****p < 0.0001; Wilcoxon matched-pairs signed rank test).

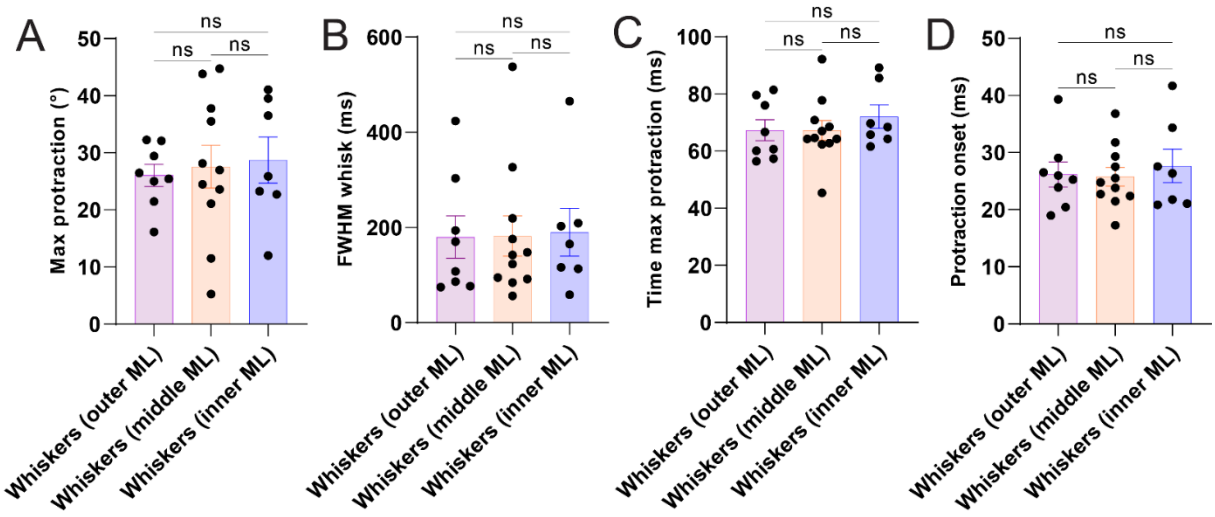

Supplementary Fig.III1.5 Distribution of whisker dynamics across sessions

(A-D) Summary plot of **(A)** maximal protraction angle, **(B)** FWHM, **(C)** time to maximal protraction and **(D)** protraction onset of the exponential fits of trial-average ipsilateral whiskers corresponding to the depth of the 2p-imaging FOVs in the outer (n = 8 sessions), middle (n = 11 sessions) and inner (n = 7 sessions) ML (ns $p > 0.05$; Kruskal-Wallis with Dunn's multiple comparisons test). Error bars are median with IQR.

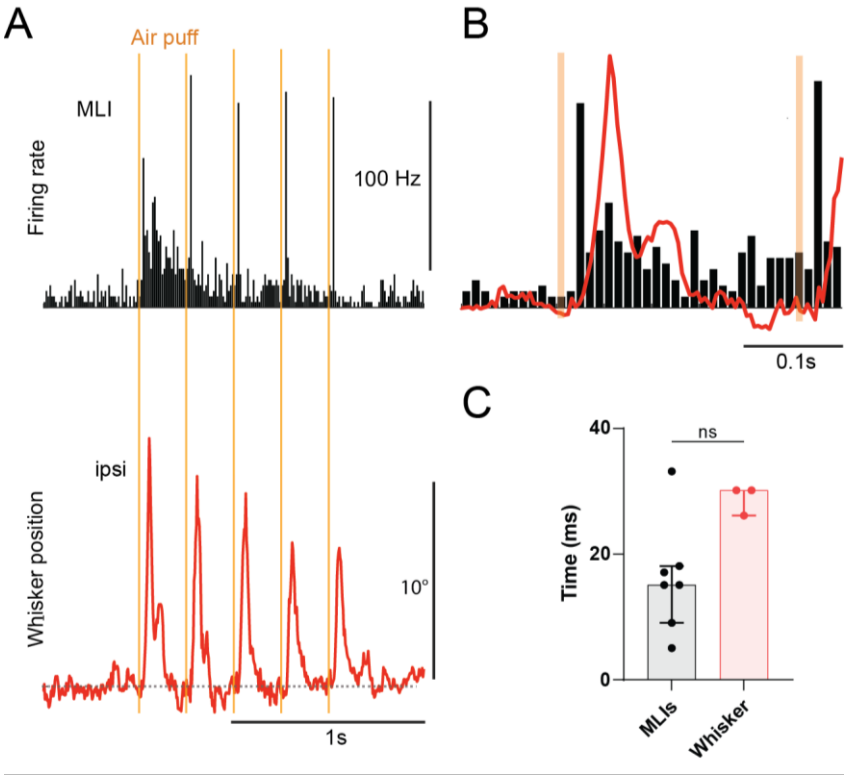

Supplementary Fig.III2.1 Firing rate of putative MLIs peaks before whisker onset

(A) *Top:* Neuropixels extracellular recording of the trial-average firing rate histogram (1 ms bins) of a putative MLI (*top*) and whisker protraction angle (*bottom*) during five consecutive air-puffs to the whisker (*orange*, 10 ms, 20 psi; 4 Hz, n = 30 trials). MLIs are identified based on vicinity to Complex Spikes (located in the Molecular Layer) and firing frequency.
(B) Zoomed view of the first puff-evoked superimposed response of MLIs (*black*) and whiskers (*red*) presented in (A) showing high-frequency response preceding whisker onset.
(C) Summary plot comparing the time of maximal firing rate of MLIs (median = 15 ms, n = 7 MLIs, 3 mice) and whisk onset (median = 30 ms, n = 3 recordings, 3 mice) immediately following air-puff stimulation (ns p = 0.10, Mann-Whitney test). Error bars are median with IQR.

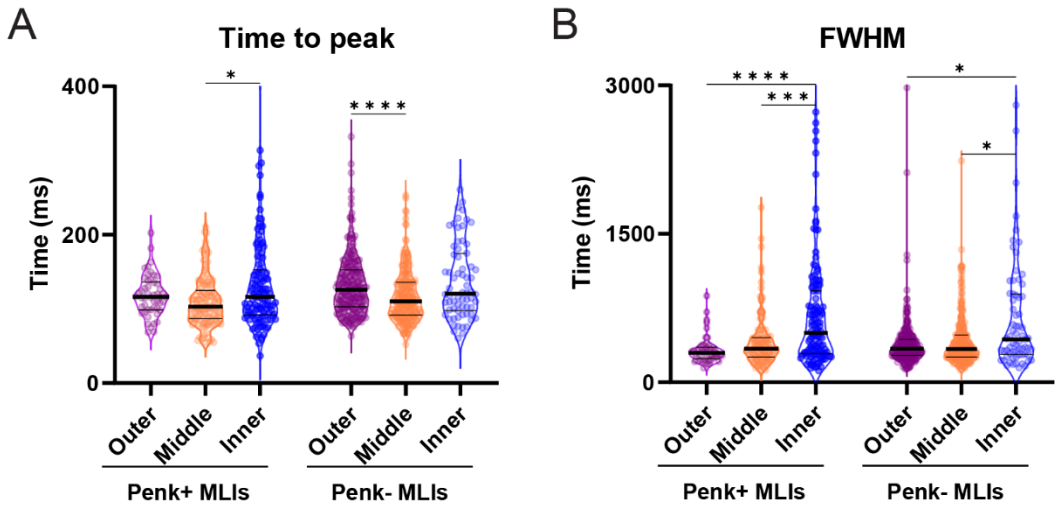

Supplementary Fig.III4.1 Ca^{2+} response time-to-peak and FWHM are similar between layer-matched Penk+ and Penk- MLIs

(A) Summary plot for time-to-peak of puff-evoked Ca^{2+} activity of MLIs imaged at different depths (each dot represents the trial-averaged MLI response), segregated based on Penk expression, showing no differences between Penk+ and Penk- MLIs (layer-matched non-significant differences not shown $p > 0.05$, *$p < 0.05$, ****$p < 0.0001$; Kruskal-Wallis with Dunn's multiple comparisons test). Error bars are median with IQR.
(B) Summary plot of FWHM of the same Ca^{2+} traces as in (A) showing a conserved decrease with depth independent of *Penk* expression (layer-matched non-significant differences not shown $p > 0.05$, *$p < 0.05$, ***$p < 0.001$, ****$p < 0.0001$; Kruskal-Wallis with Dunn's multiple comparisons test). Error bars are median with IQR.

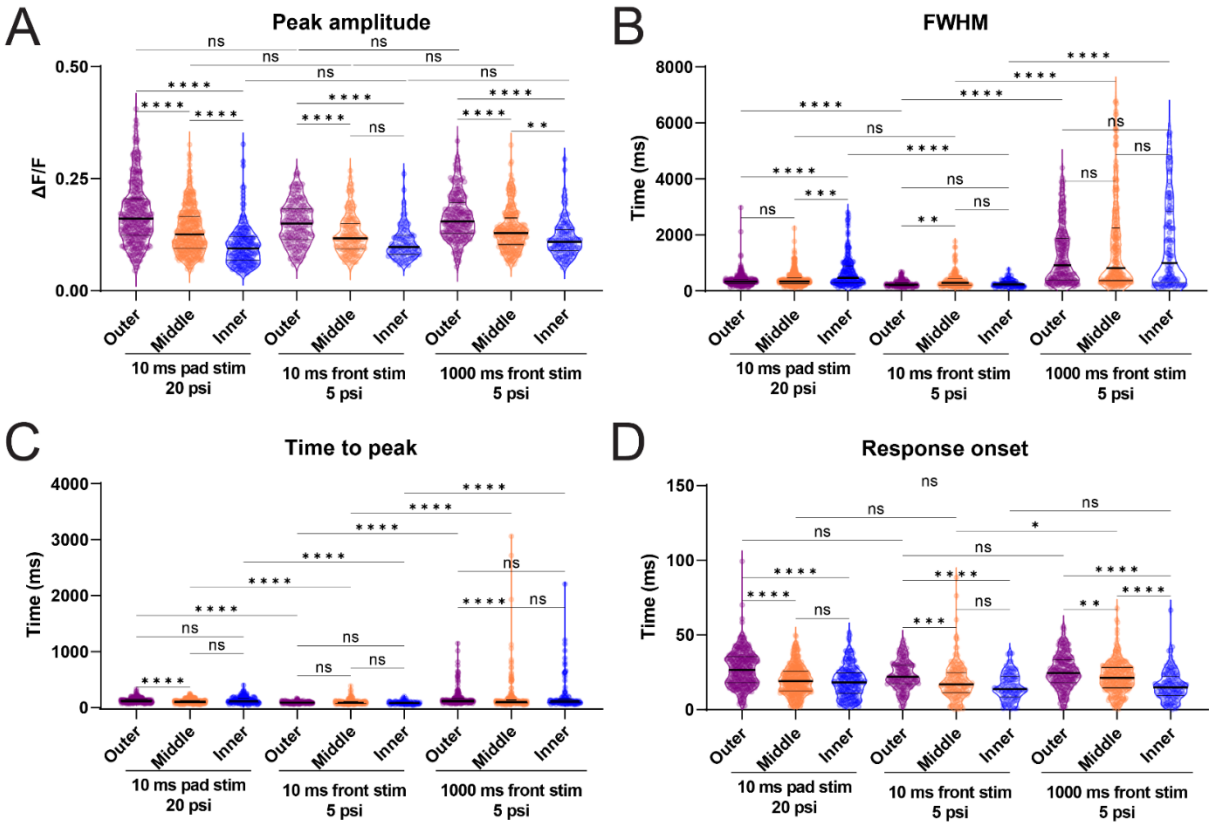

Supplementary Fig.III8.1 Distribution of MLI Ca^{2+} activity temporal patterns between stimulation type and layer depth

(A-D) Summary plot for peak amplitude **(A)**, FWHM **(B)**, time-to-peak **(C)** and response onset **(D)** of Ca^{2+} activity of MLIs evoked using different stimulation protocol and imaged at different depths (each dot represents the trial-averaged MLI response), in the outer (*magenta*), middle (*orange*) and inner (*blue*) ML, respectively. Same cells presented in (Figure III8 B,D) divided by layer in ML (ns $p > 0.05$, *$p < 0.05$, **$p < 0.01$, ***$p < 0.001$, ***$p < 0.0001$; Kruskal-Wallis with Dunn's multiple comparisons test). Error bars are median with IQR.

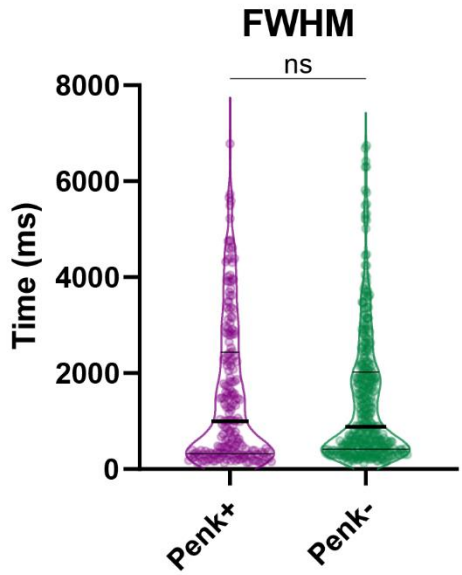

Supplementary Fig.III8.2 Distribution of Ca^{2+} response FWHM to long stimulation between Penk+ and Penk- MLIs

Summary plot for FWHM of Ca^{2+} activity Penk+ (n = 205 cells, *magenta*) and Penk - (n = 369 cells, *green*) MLIs, evoked by long front stimulation (1000 ms, 5 psi). Same cells presented in (Figure III8 B) divided by expression of *Penk1* gene. (ns p = 0.66; Mann-Whitney test). Error bars are median with IQR.

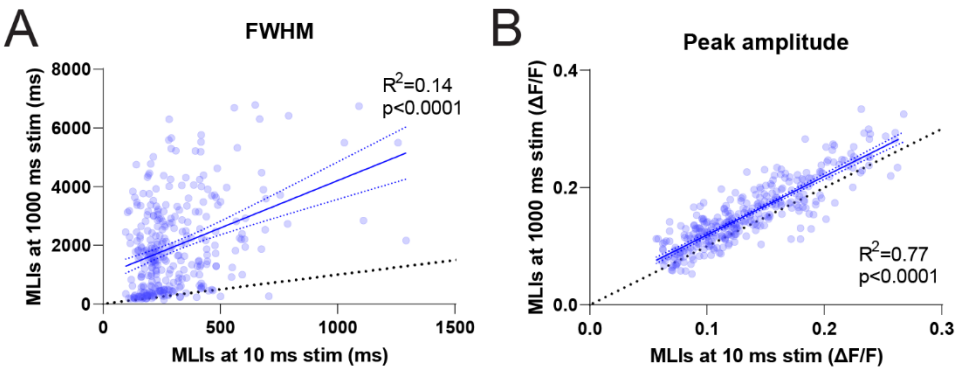

Supplementary Fig.III8.3 Cell-matched Ca^{2+} response FWHM and peak amplitude change between short and long whisker stimulation

(A) Average Ca^{2+} activity FWHM of individual MLIs responding to 10 ms vs 1000 ms cross-correlation with linear fit shown in dashed blue lines (r = 0.31, Spearman's rank correlation). Dashed black line represents line of identity.
(B) Same as in (A), but for peak amplitude (r = 0.86, Spearman's rank correlation).

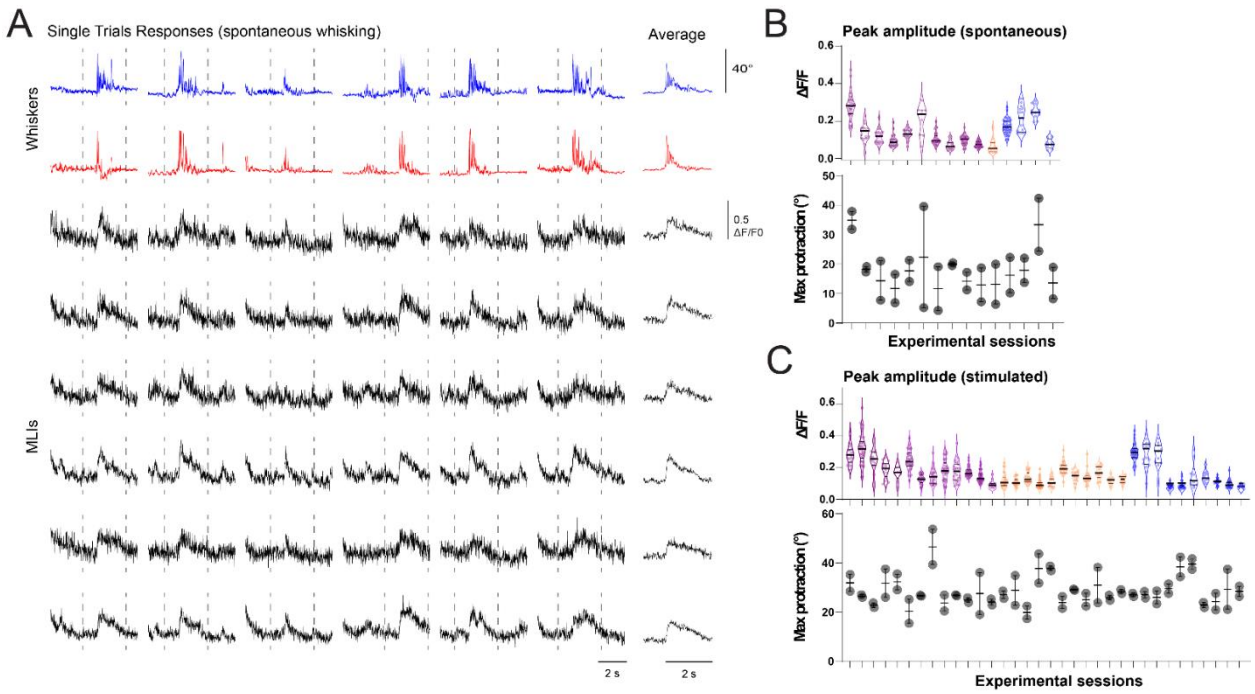

Supplementary Fig.III9.1 Distribution of Ca^{2+} activity peak amplitude and whisker protraction across sessions of spontaneous and stimulated responses

(A) Example single-trial spontaneous whisk epochs (upwards indicates protraction, *blue* – contralateral, *red* - ipsilateral) and of GCaMP8f Ca^{2+} traces of five MLIs imaged at 100Hz (*black*). Bottom traces represent cell-averaged responses. Right traces represent the trial-average responses, aligned to the 10-degree angle of whisker deflection.
(B – C) Summary plot of the peak amplitude of the trial-averaged Ca^{2+} traces in each FOV in outer (*magenta*) middle (*orange*) and inner (*blue*) layers (*top*) and whiskers maximal protraction angle (*bottom*) for spontaneous **(B)** and puff-evoked **(C)** whisking. Same FOVs used for cross-correlation (Figure III9 F and G, respectively). Error bars are median with IQR.

IV. Conclusion and future directions

Previously, the gap junction antagonist mefloquine was used *in vitro* to block propagation of synchronous firing (J. Kim et al., 2014). *In vivo,* one approach could take advantage of the cerebellar cortex gap junction configuration which is primarily made of the protein connexin-36 subunits arranged in a hexamer and has to be expressed in both connected interneurons (Alcami & Marty, 2013). Indeed, a conditional knockout transgenic mouse line of connexion-36 (Cx36-floxed mice) exists (Wellershaus et al., 2008). Nevertheless GoCs also form connexin-36 dependent gap junctions (Gurnani & Silver, 2021; Kozareva et al., 2021; Vervaeke et al., 2010). Therefore, to directly and selectively abolish electrical coupling in MLIs and further avoid perturbation of GoCs, an MLI specific marker would be ideally suited to distinguish between interneuron types and avoid overlapping expression with other brain regions. Novel transcriptomic analysis might indicate such a marker (Kozareva et al., 2021) and by doing so, enable us to further manipulate those subpopulations independently and asses *in vivo* the role of gap junctions on MLI function and its influence on behaviour.

Another aspect to consider is that the synchronized recruitment of MLIs provided by gap junctions is preferentially oriented on the parasagittal plane (J. Kim et al., 2014; Rieubland et al., 2014). Evidence *in vivo* suggests that in response to licking, the activity of MLIs across layers is correlated on the PF input axis and only decreases on the transversal plane in SCs with distances over 100 microns, while maintained in BCs (Astorga et al., 2017). As our imaging experiments prioritised temporal resolution at the expense of a reduced FOV, it is not clear from our data if similar effects would be induced by whisker stimulation. Also, it is possible that the sensory drive produced by the powerful stimulus might strongly activate PF pathways to the extent that subtle spatial orientation effects could be overwritten by the stimulus, while possibly maintained during exploratory, self-initiated whisking.

The importance of the cerebellum in monitoring and adjusting the acquisition of the majority of the sensory data was highlighted early on (Bower, 1997). Supporting a strong sensory drive, but also motor related components, our data reflects a diverse interplay between sensory and motor variables during stimulated and self-initiated whisking. It is possible that a further analysis exploring the manifolds of the MLI response trajectories could reveal the different dimensions of sensorimotor variables during whisking that are not distinguishable by analysis of discrete features only (Jazayeri & Ostojic, 2021). For example, using a general linear model, a recent study was able to show that MLIs encode information related to the learned valence of odours (Ma et al., 2020). Similarly, this type of analysis might be able to separate

sensory from motor components in the MLI responses in a trial-by-trial analysis. Furthermore, pharmacological approaches that inhibit the sensory feedback such as applying lidocaine to the facial nerve (S. T. Brown & Raman, 2018) and concomitant recordings of MLI activity might help isolate motor components in awake animals and provide insight into the integration mechanisms of different sensorimotor information.

Evidence from *in vivo* recordings of both MLIs and PCs suggest that air puffs to the whiskers trigger sensory responses in MLIs that induce inhibition of PCs within a millisecond precision (Chu et al., 2011, 2012). Meanwhile, the transient inhibition in PCs simple spikes may undergo CF-mediated selective adaptation with repeated stimulation (Zempolich et al., 2021). During self-initiated activity MLIs and PCs encode whisker kinematics in a similar fashion (Chen et al., 2016, 2017). Their activity sometimes precedes whisking, probably encoding an efference copy of the motor command. Rather than the sensory related initiation of response, during spontaneous whisking the MLI activity might play a role in cancelling sensory signals produced by self-generated motion, as previously described for head rotation in the vestibulocerebellum (Cullen, 2012). It is therefore possible that MLIs act to disambiguate the sensory and motor information processing with high temporal resolution, during evoked and self-initiated behaviour. Indeed, studies on whisker-stimulated PCs activity report an initial transient suppression of simple-spikes, that enables a well-timed DCN disinhibition and the subsequent whisker protraction (S. T. Brown & Raman, 2018). Failing to provide this temporally accurate PC output may result in social, cognitive and motor impairments (De Zeeuw et al., 2011; Stoodley et al., 2017; Tsai et al., 2012), which might partially be linked to a faulty MLI inhibition (Badura et al., 2018; Bonnan et al., 2023; Gaffield et al., 2018). It would therefore be interesting to interrogate the causal effect of MLI inhibition on PCs activity and whisker movement kinematics. A selective perturbation of functional subsets of MLIs by using a Cx36 conditional knockout transgenic mouse line (Wellershaus et al., 2008) coupled with transcriptional classes (Kozareva et al., 2021) and optogenetic techniques, would enable us to target the desired MLI type and area while avoiding compensatory adaptations of the network. Within this configuration we could monitor the activity of PCs. Given the role of inner MLIs in modulating the responses of PCs during sensorimotor processing (Arlt & Häusser, 2020; Han et al., 2018; Mittmann et al., 2005), we would expect a less synchronized response and possibly a disruption of deflection angles (S. T. Brown & Raman, 2018; Romano et al., 2018). Moreover, MLIs are known to play a key role in associative learning tasks such as eyeblink conditioning (Heiney, Kim, et al., 2014), VOR adaptation (Bonnan et al., 2023; Rowan et al., 2018) and even valence discrimination (Ma et al., 2020). The effect of MLI perturbation could further extend

to learned adaptation during repeated whisker stimulation (Romano et al., 2018; Zempolich et al., 2021). A selective targeting of specific functional classes of MLIs and concomitant monitoring of PCs activity during such tasks, could provide us with further insight into learning induced dynamic changes in their activity and disambiguate the differential roles of MLIs.

With regards to behaviour, the area of Crus I imaged here has been repeatedly reported to accurately encode whisker kinematics (S. T. Brown & Raman, 2018; Chen et al., 2016, 2017; Proville et al., 2014) and to a large extent sensory responses in the absence of any movement (Arlt & Häusser, 2020; Bosman et al., 2010; Chu et al., 2011, 2012). Also, the stimulation protocol used provides a simple method to repeatedly and reliably induce whisking (S. T. Brown & Raman, 2018), while avoiding complex and variable activity patterns present in tasks that generate signals induced by dexterous movements or reward (Becker & Person, 2019; Kostadinov & Häusser, 2022). It is not however excluded that affective states or small movements sometimes associated with the whisking, contribute to the MLI responses observed. Despite habituation measures aimed to familiarize the animal with the setup and reduce distress, it is possible that affective states influence the responses and contribute to individual differences between mice's behaviour (Ito, 2008; Sugihara, 2018). Furthermore, stimulus-induced amplitudes whisker protractions as well as reaction delay and whisking length can differ between trials and animals, suggesting some diversity in their sensitivity to the stimulation. Meanwhile, the spontaneous whisking can vary greatly in dynamics and amplitude. Therefore, differences in responses of same-cell between sensory-evoked and self-initiated whisking differs to various extent both in terms of sensory load and movement. We addressed this issue by consistently measuring different layers in a randomised order within each experimental session, but further analysis using a linear mixed model could better account for random effects produced by repeated measures within a session or for different animals. Also, indirect behavioural measures of arousal and emotional states such as readings of heart rate, pupil dilation and facial expression could be used in the future to complement sensorimotor features of neural activity (Dolensek et al., 2020).

Furthermore, while a simple behavioural response induced by whisker stimulation can be suitable to interrogate the cerebellar information flow (S. T. Brown & Raman, 2018), learning induced behavioural adaptations are limited in the absence motor errors carried by CF activity, to which MLIs are an essential mediating component (Bonnan et al., 2023; Gaffield et al., 2018; Ma et al., 2020; Rowan et al., 2018). Thus, it would be important in future studies to address if morphological and molecularly defined subclasses of MLIs are differentially engaged in complex tasks.

In summary, using fast Ca^{2+} imaging of MLIs in awake mice during sensory-evoked and spontaneous whisking, we were able to identify that this neural population is engaged by different sensorimotor variables during behaviour and acquires a layer-specific processing, most likely inherited from GCs input (**Figure IV1**). The depth-dependent heterogeneity in representations of GCs could be due to a modality-specific distribution or a selectivity in frequency tuning (Ihikawa et al., 2015; Markwalter et al., 2019; Straub et al.,2020; Shuster et al. 2021). This can translate into the laminar distribution of the neural signatures of MLI responses, which may further underlie differential roles in sculpting the temporal accuracy of PCs information processing (Arlt & Häusser, 2020). It remains to be investigated if different molecularly defined classes of MLIs have diverse functions in complex cerebellar dependent tasks, such as associative motor learning.

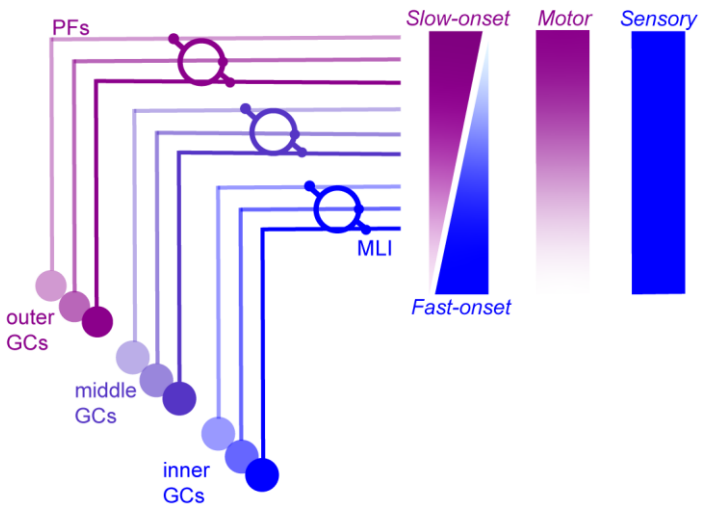

Figure IV1. Summary illustration of the GC mediated depth-dependence of MLI response onsets and possible mechanisms

Outer PFs and MLIs have a higher proportion of stimulus-evoked slow-onset cells (*magenta*) that better represent whisker kinematics, while inner PFs and MLIs show preponderantly faster onsets (*blue*) that precede whisking. Longer whisker stimulation induced prolonged MLI responses with a similar laminar distribution. Our data therefore suggests a bias towards proprioceptive and motor encoding of whisking dynamics in the outer MLIs, but a robust somatosensory representation throughout the depth of the molecular layer.

Bibliography

Abadía, I., Naveros, F., Ros, E., Carrillo, R. R., & Luque, N. R. (2021). A cerebellar-based solution to the nondeterministic time delay problem in robotic control. *Science Robotics*, *6*(58), eabf2756. https://doi.org/10.1126/scirobotics.abf2756

Abeles, M. (1982). *Local Cortical Circuits: An Electrophysiological Study*. Springer-Verlag. https://doi.org/10.1007/978-3-642-81708-3

Abrahamsson, T., Cathala, L., Matsui, K., Shigemoto, R., & DiGregorio, D. A. (2012). Thin Dendrites of Cerebellar Interneurons Confer Sublinear Synaptic Integration and a Gradient of Short-Term Plasticity. *Neuron*, *73*(6), 1159–1172. https://doi.org/10.1016/j.neuron.2012.01.027

Ahn, A. H., Dziennis, S., Hawkes, R., & Herrup, K. (1994). The cloning of zebrin II reveals its identity with aldolase C. *Development*, *120*(8), 2081–2090. https://doi.org/10.1242/dev.120.8.2081

Albergaria, C., Silva, N. T., Pritchett, D. L., & Carey, M. R. (2018). Locomotor activity modulates associative learning in mouse cerebellum. *Nature Neuroscience*, *21*(5), 725–735. https://doi.org/10.1038/s41593-018-0129-x

Albus, J. S. (1971). A theory of cerebellar function. *Mathematical Biosciences*, *10*(1–2), 25–61. https://doi.org/10.1016/0025-5564(71)90051-4

Alcami, P. (2018). Electrical Synapses Enhance and Accelerate Interneuron Recruitment in Response to Coincident and Sequential Excitation. *Frontiers in Cellular Neuroscience*, *12*, 156. https://doi.org/10.3389/fncel.2018.00156

Alcami, P., & Marty, A. (2013). Estimating functional connectivity in an electrically coupled interneuron network. *Proceedings of the National Academy of Sciences*, *110*(49). https://doi.org/10.1073/pnas.1310983110

Allen Institute for Brain Science. (2004). *Allen Institute for Brain Science. Allen Mouse Brain Atlas [74827108]*. mouse.brain-map.org

Aller, M. I., Jones, A., Merlo, D., Paterlini, M., Meyer, A. H., Amtmann, U., Brickley, S., Jolin, H. E., McKenzie, A. N. J., Monyer, H., Farrant, M., & Wisden, W. (2003). Cerebellar granule cell Cre recombinase expression. *Genesis*, *36*(2), 97–103. https://doi.org/10.1002/gene.10204

Altman, J. (1972a). Postnatal development of the cerebellar cortex in the rat. I. The external germinal layer and the transitional molecular layer. *The Journal of Comparative Neurology*, *145*(3), 353–397. https://doi.org/10.1002/cne.901450305

Altman, J. (1972b). Postnatal development of the cerebellar cortex in the rat. II. Phases in the maturation of Purkinje cells and of the molecular layer. *The Journal of Comparative Neurology*, *145*(4), 399–463. https://doi.org/10.1002/cne.901450402

Altman, J. (1972c). Postnatal development of the cerebellar cortex in the rat. III. Maturation of the components of the granular layer. *The Journal of Comparative Neurology*, *145*(4), 465–513. https://doi.org/10.1002/cne.901450403

Altman, J., & Bayer, S. A. (1980a). Development of the brain stem in the rat. I. Thymidine-radiographic study of the time of origin of neurons of the lower medulla. *The Journal of Comparative Neurology*, *194*(1), 1–35. https://doi.org/10.1002/cne.901940102

Altman, J., & Bayer, S. A. (1980b). Development of the brain Stem in the rat. II. Thymidine-radiographic study of the time of origin of neurons of the upper medulla, excluding the vestibular and auditory nuclei. *The Journal of Comparative Neurology*, *194*(1), 37–56. https://doi.org/10.1002/cne.901940103

Altman, J., & Bayer, S. A. (1980c). Development of the brain stem in the rat. III. Thymidine-radiographic study of the time of origin of neurons of the vestibular and auditory nuclei of the upper medulla. *The Journal of Comparative Neurology*, *194*(4), 877–904. https://doi.org/10.1002/cne.901940410

Altman, J., & Bayer, S. A. (1980d). Development of the brain stem in the rat. IV. Thymidine-radiographic study of the time of orgin of neurons in the pontine region. *The Journal of Comparative Neurology*, *194*(4), 905–929. https://doi.org/10.1002/cne.901940411

Altman, J., & Bayer, S. A. (1981). Development of the brain stem in the rat. V. Thymidine-radiographic study of the time of origin of neurons in the midbrain tegmentum. *The Journal of Comparative Neurology*, *198*(4), 677–716. https://doi.org/10.1002/cne.901980409

Amino, Y., Kyuhou, S., Matsuzaki, R., & Gemba, H. (2001). Cerebello–thalamo–cortical projections to the posterior parietal cortex in the macaque monkey. *Neuroscience Letters*, *309*(1), 29–32. https://doi.org/10.1016/S0304-3940(01)02018-3

Apps, R., & Garwicz, M. (2005). Anatomical and physiological foundations of cerebellar information processing. *Nature Reviews Neuroscience*, *6*(4), 297–311. https://doi.org/10.1038/nrn1646

Apps, R., & Hawkes, R. (2009). Cerebellar cortical organization: A one-map hypothesis. *Nature Reviews Neuroscience*, *10*(9), 670–681. https://doi.org/10.1038/nrn2698

Apps, R., Hawkes, R., Aoki, S., Bengtsson, F., Brown, A. M., Chen, G., Ebner, T. J., Isope, P., Jörntell, H., Lackey, E. P., Lawrenson, C., Lumb, B., Schonewille, M., Sillitoe, R. V., Spaeth, L., Sugihara, I., Valera, A., Voogd, J., Wylie, D. R., & Ruigrok, T. J. H. (2018). Cerebellar Modules and Their Role as Operational Cerebellar Processing Units. *The Cerebellum*, *17*(5), 654–682. https://doi.org/10.1007/s12311-018-0952-3

Arlt, C., & Häusser, M. (2020). Microcircuit Rules Governing Impact of Single Interneurons on Purkinje Cell Output In Vivo. *Cell Reports*, *30*(9), 3020-3035.e3. https://doi.org/10.1016/j.celrep.2020.02.009

Astorga, G., Li, D., Therreau, L., Kassa, M., Marty, A., & Llano, I. (2017). Concerted Interneuron Activity in the Cerebellar Molecular Layer During Rhythmic Oromotor Behaviors. *The Journal of Neuroscience*, *37*(47), 11455–11468. https://doi.org/10.1523/JNEUROSCI.1091-17.2017

Badura, A., Verpeut, J. L., Metzger, J. W., Pereira, T. D., Pisano, T. J., Deverett, B., Bakshinskaya, D. E., & Wang, S. S.-H. (2018). Normal cognitive and social development require posterior cerebellar activity. *ELife*, *7*, e36401. https://doi.org/10.7554/eLife.36401

Bakhurin, K. I., Goudar, V., Shobe, J. L., Claar, L. D., Buonomano, D. V., & Masmanidis, S. C. (2017). Differential Encoding of Time by Prefrontal and Striatal Network Dynamics. *Journal of Neuroscience*, *37*(4), 854–870. https://doi.org/10.1523/JNEUROSCI.1789-16.2016

Balcı, F., & Simen, P. (2016). A decision model of timing. *Current Opinion in Behavioral Sciences*, *8*, 94–101. https://doi.org/10.1016/j.cobeha.2016.02.002

Balsters, J. H., Cussans, E., Diedrichsen, J., Phillips, K. A., Preuss, T. M., Rilling, J. K., & Ramnani, N. (2010). Evolution of the cerebellar cortex: The selective expansion of prefrontal-projecting cerebellar lobules. *NeuroImage*, *49*(3), 2045–2052. https://doi.org/10.1016/j.neuroimage.2009.10.045

Bao, J., Reim, K., & Sakaba, T. (2010). Target-Dependent Feedforward Inhibition Mediated by Short-Term Synaptic Plasticity in the Cerebellum. *Journal of Neuroscience*, *30*(24), 8171–8179. https://doi.org/10.1523/JNEUROSCI.0276-10.2010

Barbour, B. (1993). Synaptic currents evoked in purkinje cells by stimulating individual granule cells. *Neuron*, *11*(4), 759–769. https://doi.org/10.1016/0896-6273(93)90085-6

Barri, A., Wiechert, M. T., Jazayeri, M., & DiGregorio, D. A. (2022). Synaptic basis of a sub-second representation of time in a neural circuit model. *Nature Communications*, *13*(1), 7902. https://doi.org/10.1038/s41467-022-35395-y

Becker, M. I., & Person, A. L. (2019). Cerebellar Control of Reach Kinematics for Endpoint Precision. *Neuron*, *103*(2), 335-348.e5. https://doi.org/10.1016/j.neuron.2019.05.007

Berkley, K. J., & Worden, I. G. (1978). Projections to the inferior olive of the cat I. Comparisons of input from the dorsal column nuclei, the lateral cervical nucleus, the spino-olivary pathways, the cerebral cortex and the cerebellum. *The Journal of Comparative Neurology*, *180*(2), 237–251. https://doi.org/10.1002/cne.901800204

Billings, G., Piasini, E., Lőrincz, A., Nusser, Z., & Silver, R. A. (2014). Network Structure within the Cerebellar Input Layer Enables Lossless Sparse Encoding. *Neuron*, *83*(4), 960–974. https://doi.org/10.1016/j.neuron.2014.07.020

Blakemore, S.-J., Wolpert, D. M., & Frith, C. D. (1998). Central cancellation of self-produced tickle sensation. *Nature Neuroscience*, *1*(7), 635–640. https://doi.org/10.1038/2870

Blatt, G. J., & Eisenman, L. M. (1988). Topographic and zonal organization of the olivocerebellar projection in the reeler mutant mouse. *The Journal of Comparative Neurology*, *267*(4), 603–615. https://doi.org/10.1002/cne.902670412

Blot, A., & Barbour, B. (2014). Ultra-rapid axon-axon ephaptic inhibition of cerebellar Purkinje cells by the pinceau. *Nature Neuroscience*, *17*(2), 289–295. https://doi.org/10.1038/nn.3624

Blot, A., De Solages, C., Ostojic, S., Szapiro, G., Hakim, V., & Léna, C. (2016). Time-invariant feed-forward inhibition of Purkinje cells in the cerebellar cortex *in vivo*: Interneurons *in vivo*. *The Journal of Physiology*, *594*(10), 2729–2749. https://doi.org/10.1113/JP271518

Bodnar, R. J. (2022). Endogenous opiates and behavior: 2020. *Peptides*, *151*, 170752. https://doi.org/10.1016/j.peptides.2022.170752

Boegman, R. J., Parent, A., & Hawkes, R. (1988). Zonation in the rat cerebellar cortex: Patches of high acetylcholinesterase activity in the granular layer are congruent with Purkinje cell compartments. *Brain Research*, *448*(2), 237–251. https://doi.org/10.1016/0006-8993(88)91261-9

Boele, H.-J., Peter, S., Ten Brinke, M. M., Verdonschot, L., IJpelaar, A. C. H., Rizopoulos, D., Gao, Z., Koekkoek, S. K. E., & De Zeeuw, C. I. (2018). Impact of parallel fibre to Purkinje cell long-term depression is unmasked in absence of inhibitory input. *Science Advances*, *4*(10), eaas9426. https://doi.org/10.1126/sciadv.aas9426

Bonnan, A., Zhang, K., Gaffield, M. A., & Christie, J. M. (2023). Expression of a Form of Cerebellar Motor Memory Requires Learned Alterations to the Activity of Inhibitory Molecular Layer Interneurons. *The Journal of Neuroscience*, *43*(4), 601–612. https://doi.org/10.1523/JNEUROSCI.0731-22.2022

Bosman, L. W. J., Houweling, A. R., Owens, C. B., Tanke, N., Shevchouk, O. T., Rahmati, N., Teunissen, W. H. T., Ju, C., Gong, W., Koekkoek, S. K. E., & De Zeeuw, C. I. (2011). Anatomical Pathways Involved in Generating and Sensing Rhythmic Whisker Movements. *Frontiers in Integrative Neuroscience*, *5*. https://doi.org/10.3389/fnint.2011.00053

Bosman, L. W. J., Koekkoek, S. K. E., Shapiro, J., Rijken, B. F. M., Zandstra, F., Van Der Ende, B., Owens, C. B., Potters, J.-W., De Gruijl, J. R., Ruigrok, T. J. H., & De Zeeuw, C. I. (2010). Encoding of whisker input by cerebellar Purkinje cells: Whisker encoding by Purkinje cells. *The Journal of Physiology*, *588*(19), 3757–3783. https://doi.org/10.1113/jphysiol.2010.195180

Bostan, A. C., Dum, R. P., & Strick, P. L. (2013). Cerebellar networks with the cerebral cortex and basal ganglia. *Trends in Cognitive Sciences*, *17*(5), 241–254. https://doi.org/10.1016/j.tics.2013.03.003

Bourrat, F., & Sotelo, C. (1991). Relationships between neuronal birthdates and cytoarchitecture in the rat inferior olivary complex. *The Journal of Comparative Neurology*, *313*(3), 509–521. https://doi.org/10.1002/cne.903130311

Bower, J. M. (1997). Chapter 27 Is the cerebellum sensory for motor's sake, or motor for sensory's sake: The view from the whiskers of a rat? In *Progress in Brain Research* (Vol. 114, pp. 463–496). Elsevier. https://doi.org/10.1016/S0079-6123(08)63381-6

Bower, J. M. (2011). Functional implications of tactile projection patterns to the lateral hemispheres of the cerebellum of the albino rat: The legacy of Wally Welker: Tactile projections to rat cerebellum. *Annals of the New York Academy of Sciences*, *1225*(1), 130–141. https://doi.org/10.1111/j.1749-6632.2011.06020.x

Boyden, E. S., Katoh, A., & Raymond, J. L. (2004). CEREBELLUM-DEPENDENT LEARNING: The Role of Multiple Plasticity Mechanisms. *Annual Review of Neuroscience*, *27*(1), 581–609. https://doi.org/10.1146/annurev.neuro.27.070203.144238

Boyle, K. A., Gutierrez-Mecinas, M., Polgár, E., Mooney, N., O'Connor, E., Furuta, T., Watanabe, M., & Todd, A. J. (2017). A quantitative study of neurochemically defined populations of inhibitory interneurons in the superficial dorsal horn of the mouse spinal cord. *Neuroscience*, *363*, 120–133. https://doi.org/10.1016/j.neuroscience.2017.08.044

Braitenberg, V. (1967). Is the Cerebellar Cortex a Biological Clock in the Millisecond Range? In C. A. Fox & R. S. Snider (Eds.), *Progress in Brain Research* (Vol. 25, pp. 334–346). Elsevier. https://doi.org/10.1016/S0079-6123(08)60971-1

Brooks, J. X., Carriot, J., & Cullen, K. E. (2015). Learning to expect the unexpected: Rapid updating in primate cerebellum during voluntary self-motion. *Nature Neuroscience*, *18*(9), 1310–1317. https://doi.org/10.1038/nn.4077

Brooks, J. X., & Cullen, K. E. (2013). The Primate Cerebellum Selectively Encodes Unexpected Self-Motion. *Current Biology*, *23*(11), 947–955. https://doi.org/10.1016/j.cub.2013.04.029

Brown, A. M., Arancillo, M., Lin, T., Catt, D. R., Zhou, J., Lackey, E. P., Stay, T. L., Zuo, Z., White, J. J., & Sillitoe, R. V. (2019). Molecular layer interneurons shape the spike activity of cerebellar Purkinje cells. *Scientific Reports*, *9*(1), 1742. https://doi.org/10.1038/s41598-018-38264-1

Brown, I. E., & Bower, J. M. (2001). Congruence of mossy fibre and climbing fibre tactile projections in the lateral hemispheres of the rat cerebellum. *The Journal of Comparative Neurology*, *429*(1), 59–70. https://doi.org/10.1002/1096-9861(20000101)429:1<59::AID-CNE5>3.0.CO;2-3

Brown, S. T., & Raman, I. M. (2018). Sensorimotor Integration and Amplification of Reflexive Whisking by Well-Timed Spiking in the Cerebellar Corticonuclear Circuit. *Neuron*, *99*(3), 564-575.e2. https://doi.org/10.1016/j.neuron.2018.06.028

Buonomano, D. V., & Mauk, M. (1994). Neural network model of the cerebellum: Temporal discrimination and the timing of motor responses. *Neural Computation*, *6*(1), 38–55. https://doi.org/10.1162/neco.1994.6.1.38

Buonomano, D. V., & Merzenich, M. M. (1995). Temporal information transformed into a spatial code by a neural network with realistic properties. *Science*, *267*(5200), 1028–1030. https://doi.org/10.1126/science.7863330

Buzsáki, G., & Llinás, R. (2017). Space and time in the brain. *Science*, *358*(6362), 482–485. https://doi.org/10.1126/science.aan8869

Carlson, B. A. (2009). Temporal-Pattern Recognition by Single Neurons in a Sensory Pathway Devoted to Social Communication Behavior. *Journal of Neuroscience*, *29*(30), 9417–9428. https://doi.org/10.1523/JNEUROSCI.1980-09.2009

Carpenter, M. B. (1991). *Core text of Neuroanatomy* (4th ed.). Williams & Wilkins.

Carta, I., Chen, C. H., Schott, A. L., Dorizan, S., & Khodakhah, K. (2019). Cerebellar modulation of the reward circuitry and social behavior. *Science*, *363*(6424), eaav0581. https://doi.org/10.1126/science.aav0581

Cayco-Gajic, N. A., Clopath, C., & Silver, R. A. (2017). Sparse synaptic connectivity is required for decorrelation and pattern separation in feedforward networks. *Nature Communications*, *8*(1), 1116. https://doi.org/10.1038/s41467-017-01109-y

Cayco-Gajic, N. A., & Silver, R. A. (2019). Re-evaluating Circuit Mechanisms Underlying Pattern Separation. *Neuron*, *101*(4), 584–602. https://doi.org/10.1016/j.neuron.2019.01.044

Cerminara, N. L., Lang, E. J., Sillitoe, R. V., & Apps, R. (2015). Redefining the cerebellar cortex as an assembly of non-uniform Purkinje cell microcircuits. *Nature Reviews Neuroscience*, *16*(2), 79–93. https://doi.org/10.1038/nrn3886

Chabrol, F. P., Arenz, A., Wiechert, M. T., Margrie, T. W., & DiGregorio, D. A. (2015). Synaptic diversity enables temporal coding of coincident multisensory inputs in single neurons. *Nature Neuroscience*, *18*(5), 718–727. https://doi.org/10.1038/nn.3974

Chabrol, F. P., Blot, A., & Mrsic-Flogel, T. D. (2019). Cerebellar Contribution to Preparatory Activity in Motor Neocortex. *Neuron*, *103*(3), 506-519.e4. https://doi.org/10.1016/j.neuron.2019.05.022

Chadderton, P., Margrie, T. W., & Häusser, M. (2004). Integration of quanta in cerebellar granule cells during sensory processing. *Nature*, *428*(6985), 856–860. https://doi.org/10.1038/nature02442

Chalk, M., Marre, O., & Tkačik, G. (2018). Toward a unified theory of efficient, predictive, and sparse coding. *Proceedings of the National Academy of Sciences*, *115*(1), 186–191. https://doi.org/10.1073/pnas.1711114115

Chedotal, A., & Sotelo, C. (1993). The 'creeper stage' in cerebellar climbing fibre synaptogenesis precedes the 'pericellular nest'—Ultrastructural evidence with parvalbumin immunocytochemistry. *Developmental Brain Research*, *76*(2), 207–220. https://doi.org/10.1016/0165-3806(93)90209-S

Chen, S., Augustine, G. J., & Chadderton, P. (2016). The cerebellum linearly encodes whisker position during voluntary movement. *ELife*, *5*, e10509. https://doi.org/10.7554/eLife.10509

Chen, S., Augustine, G. J., & Chadderton, P. (2017). Serial processing of kinematic signals by cerebellar circuitry during voluntary whisking. *Nature Communications*, *8*(1), 232. https://doi.org/10.1038/s41467-017-00312-1

Chu, C.-P., Bing, Y.-H., Liu, H., & Qiu, D.-L. (2012). Roles of Molecular Layer Interneurons in Sensory Information Processing in Mouse Cerebellar Cortex Crus II In Vivo. *PLoS ONE*, *7*(5), e37031. https://doi.org/10.1371/journal.pone.0037031

Chu, C.-P., Bing, Y.-H., & Qiu, D.-L. (2011). Sensory stimulus evokes inhibition rather than excitation in cerebellar Purkinje cells in vivo in mice. *Neuroscience Letters*, *487*(2), 182–186. https://doi.org/10.1016/j.neulet.2010.10.018

Chung, S.-H., Sillitoe, R. V., Croci, L., Badaloni, A., Consalez, G., & Hawkes, R. (2009). Purkinje cell phenotype restricts the distribution of unipolar brush cells. *Neuroscience*, *164*(4), 1496–1508. https://doi.org/10.1016/j.neuroscience.2009.09.080

Coddington, L. T., Rudolph, S., Vande Lune, P., Overstreet-Wadiche, L., & Wadiche, J. I. (2013). Spillover-Mediated Feedforward Inhibition Functionally Segregates Interneuron Activity. *Neuron*, *78*(6), 1050–1062. https://doi.org/10.1016/j.neuron.2013.04.019

Collin, T., Chat, M., Lucas, M. G., Moreno, H., Racay, P., Schwaller, B., Marty, A., & Llano, I. (2005). Developmental Changes in Parvalbumin Regulate Presynaptic Ca^{2+} Signaling. *The Journal of Neuroscience*, *25*(1), 96–107. https://doi.org/10.1523/JNEUROSCI.3748-04.2005

Consalez, G. G., Goldowitz, D., Casoni, F., & Hawkes, R. (2021). Origins, Development, and Compartmentation of the Granule Cells of the Cerebellum. *Frontiers in Neural Circuits*, *14*, 611841. https://doi.org/10.3389/fncir.2020.611841

Consalez, G. G., & Hawkes, R. (2013). The compartmental restriction of cerebellar interneurons. *Frontiers in Neural Circuits*, *6*. https://doi.org/10.3389/fncir.2012.00123

Craig, B. T., Morrill, A., Anderson, B., Danckert, J., & Striemer, C. L. (2019). *Cerebellar lesions disrupt spatial and temporal visual attention* [Preprint]. Neuroscience. https://doi.org/10.1101/822635

Crowley, J. J., Fioravante, D., & Regehr, W. G. (2009). Dynamics of Fast and Slow Inhibition from Cerebellar Golgi Cells Allow Flexible Control of Synaptic Integration. *Neuron*, *63*(6), 843–853. https://doi.org/10.1016/j.neuron.2009.09.004

Cullen, K. E. (2012). The vestibular system: Multimodal integration and encoding of self-motion for motor control. *Trends in Neurosciences*, *35*(3), 185–196. https://doi.org/10.1016/j.tins.2011.12.001

D'Angelo, E., & Casali, S. (2013). Seeking a unified framework for cerebellar function and dysfunction: From circuit operations to cognition. *Frontiers in Neural Circuits*, *6*. https://doi.org/10.3389/fncir.2012.00116

Darmohray, D. M., Jacobs, J. R., Marques, H. G., & Carey, M. R. (2019). Spatial and Temporal Locomotor Learning in Mouse Cerebellum. *Neuron*, *102*(1), 217-231.e4. https://doi.org/10.1016/j.neuron.2019.01.038

De Solages, C., Szapiro, G., Brunel, N., Hakim, V., Isope, P., Buisseret, P., Rousseau, C., Barbour, B., & Léna, C. (2008). High-Frequency Organization and Synchrony of Activity in the Purkinje Cell Layer of the Cerebellum. *Neuron*, *58*(5), 775–788. https://doi.org/10.1016/j.neuron.2008.05.008

De Zeeuw, C. I. (2021). Bidirectional learning in upbound and downbound microzones of the cerebellum. *Nature Reviews Neuroscience*, *22*(2), 92–110. https://doi.org/10.1038/s41583-020-00392-x

De Zeeuw, C. I., Hoebeek, F. E., Bosman, L. W. J., Schonewille, M., Witter, L., & Koekkoek, S. K. (2011). Spatiotemporal firing patterns in the cerebellum. *Nature Reviews Neuroscience*, *12*(6), 327–344. https://doi.org/10.1038/nrn3011

De Zeeuw, C. I., & Romano, V. (2022). Time and tide of cerebellar synchrony. *Proceedings of the National Academy of Sciences*, *119*(17), e2204155119. https://doi.org/10.1073/pnas.2204155119

De Zeeuw, C. I., Wylie, D. R., Digiorgi, P. L., & Simpson, J. I. (1994). Projections of individual purkinje cells of identified zones in the flocculus to the vestibular and cerebellar nuclei in the

rabbit. *The Journal of Comparative Neurology*, *349*(3), 428–447. https://doi.org/10.1002/cne.903490308

Deisseroth, K. (2011). Optogenetics. *Nature Methods*, *8*(1), 26–29. https://doi.org/10.1038/nmeth.f.324

Diana, G., Sainsbury, T. T. J., & Meyer, M. P. (2019). Bayesian inference of neuronal assemblies. *PLOS Computational Biology*, *15*(10), e1007481. https://doi.org/10.1371/journal.pcbi.1007481

Dolensek, N., Gehrlach, D. A., Klein, A. S., & Gogolla, N. (2020). Facial expressions of emotion states and their neuronal correlates in mice. *Science*, *368*(6486), 89–94. https://doi.org/10.1126/science.aaz9468

Dorgans, K., Demais, V., Bailly, Y., Poulain, B., Isope, P., & Doussau, F. (2019). Short-term plasticity at cerebellar granule cell to molecular layer interneuron synapses expands information processing. *ELife*, *8*, e41586. https://doi.org/10.7554/eLife.41586

Duguid, I., Branco, T., London, M., Chadderton, P., & Häusser, M. (2012). Tonic Inhibition Enhances Fidelity of Sensory Information Transmission in the Cerebellar Cortex. *The Journal of Neuroscience*, *32*(32), 11132–11143. https://doi.org/10.1523/JNEUROSCI.0460-12.2012

Eccles, J. C., Ito, M., & Szentágothai, J. (1967). *The Cerebellum as a Neuronal Machine*. Springer Berlin Heidelberg. https://doi.org/10.1007/978-3-662-13147-3

Ekerot, C.-F., & Jörntell, H. (2001). Parallel fibre receptive fields of Purkinje cells and interneurons are climbing fibre-specific: Receptive fields of purkinje cells and interneurons. *European Journal of Neuroscience*, *13*(7), 1303–1310. https://doi.org/10.1046/j.0953-816x.2001.01499.x

Ekerot, C.-F., & Jörntell, H. (2003). Parallel fibre receptive fields: A key to understanding cerebellar operation and learning. *The Cerebellum*, *2*(2), 101–109. https://doi.org/10.1080/14734220309411

Espinosa, J. S., & Luo, L. (2008). Timing Neurogenesis and Differentiation: Insights from Quantitative Clonal Analyses of Cerebellar Granule Cells. *The Journal of Neuroscience*, *28*(10), 2301–2312. https://doi.org/10.1523/JNEUROSCI.5157-07.2008

Fore, T. R., Taylor, B. N., Brunel, N., & Hull, C. (2020). Acetylcholine Modulates Cerebellar Granule Cell Spiking by Regulating the Balance of Synaptic Excitation and Inhibition. *The Journal of Neuroscience*, *40*(14), 2882–2894. https://doi.org/10.1523/JNEUROSCI.2148-19.2020

Fritschy, J.-M. (2008). E/I balance and GABAA receptor plasticity. *Frontiers in Molecular Neuroscience*, *1*. https://doi.org/10.3389/neuro.02.005.2008

Fujita, H., Aoki, H., Ajioka, I., Yamazaki, M., Abe, M., Oh-Nishi, A., Sakimura, K., & Sugihara, I. (2014). Detailed Expression Pattern of Aldolase C (Aldoc) in the Cerebellum, Retina and Other Areas of the CNS Studied in Aldoc-Venus Knock-In Mice. *PLoS ONE*, *9*(1), e86679. https://doi.org/10.1371/journal.pone.0086679

Fujita, H., Kodama, T., & Du Lac, S. (2020). Modular output circuits of the fastigial nucleus for diverse motor and nonmotor functions of the cerebellar vermis. *ELife*, *9*, e58613. https://doi.org/10.7554/eLife.58613

Gaffield, M. A., Bonnan, A., & Christie, J. M. (2019). Conversion of Graded Presynaptic Climbing Fibre Activity into Graded Postsynaptic Ca2+ Signals by Purkinje Cell Dendrites. *Neuron*, *102*(4), 762-769.e4. https://doi.org/10.1016/j.neuron.2019.03.010

Gaffield, M. A., & Christie, J. M. (2017). Movement Rate Is Encoded and Influenced by Widespread, Coherent Activity of Cerebellar Molecular Layer Interneurons. *The Journal of Neuroscience*, *37*(18), 4751–4765. https://doi.org/10.1523/JNEUROSCI.0534-17.2017

Gaffield, M. A., Rowan, M. J. M., Amat, S. B., Hirai, H., & Christie, J. M. (2018). Inhibition gates supralinear Ca2+ signaling in Purkinje cell dendrites during practiced movements. *ELife*, *7*, e36246. https://doi.org/10.7554/eLife.36246

Galliano, E., Gao, Z., Schonewille, M., Todorov, B., Simons, E., Pop, A. S., D'Angelo, E., van den Maagdenberg, A. M. J. M., Hoebeek, F. E., & De Zeeuw, C. I. (2013). Silencing the Majority of Cerebellar Granule Cells Uncovers Their Essential Role in Motor Learning and Consolidation. *Cell Reports*, *3*(4), 1239–1251. https://doi.org/10.1016/j.celrep.2013.03.023

Gao, W., Chen, G., Reinert, K. C., & Ebner, T. J. (2006). Cerebellar Cortical Molecular Layer Inhibition Is Organized in Parasagittal Zones. *The Journal of Neuroscience*, *26*(32), 8377–8387. https://doi.org/10.1523/JNEUROSCI.2434-06.2006

Gao, Z., Proietti-Onori, M., Lin, Z., ten Brinke, M. M., Boele, H.-J., Potters, J.-W., Ruigrok, T. J. H., Hoebeek, F. E., & De Zeeuw, C. I. (2016). Excitatory Cerebellar Nucleocortical Circuit Provides Internal Amplification during Associative Conditioning. *Neuron*, *89*(3), 645–657. https://doi.org/10.1016/j.neuron.2016.01.008

Gao, Z., Van Beugen, B. J., & De Zeeuw, C. I. (2012). Distributed synergistic plasticity and cerebellar learning. *Nature Reviews Neuroscience*, *13*(9), 619–635. https://doi.org/10.1038/nrn3312

Garwicz, M., Ekerot, C.-F., & Jörntell, H. (1998). Organizational Principles of Cerebellar Neuronal Circuitry. *Physiology*, *13*(1), 26–32. https://doi.org/10.1152/physiologyonline.1998.13.1.26

Gebre, S. A., Reeber, S. L., & Sillitoe, R. V. (2012). Parasagittal compartmentation of cerebellar mossy fibres as revealed by the patterned expression of vesicular glutamate transporters VGLUT1 and VGLUT2. *Brain Structure and Function*, *217*(2), 165–180. https://doi.org/10.1007/s00429-011-0339-4

Gibbon, J. (1977). Scalar expectancy theory and Weber's law in animal timing. *Psychological Review*, *84*(3), 279–325. https://doi.org/10.1037/0033-295X.84.3.279

Giovannucci, A., Badura, A., Deverett, B., Najafi, F., Pereira, T. D., Gao, Z., Ozden, I., Kloth, A. D., Pnevmatikakis, E., Paninski, L., De Zeeuw, C. I., Medina, J. F., & Wang, S. S.-H. (2017). Cerebellar granule cells acquire a widespread predictive feedback signal during motor learning. *Nature Neuroscience*, *20*(5), 727–734. https://doi.org/10.1038/nn.4531

Glickstein, M., Strata, P., & Voogd, J. (2009). Cerebellum: History. *Neuroscience*, *162*(3), 549–559. https://doi.org/10.1016/j.neuroscience.2009.02.054

Gravel, C., Leclerc, N., Rafrafi, J., Sasseville, R., Thivierge, L., & Hawkes, R. (1987). Monoclonal antibodies reveal the global organization of the cerebellar cortex. *Journal of Neuroscience Methods*, *21*(2–4), 145–157. https://doi.org/10.1016/0165-0270(87)90112-9

Guo, C., Rudolph, S., Neuwirth, M. E., & Regehr, W. G. (2021). Purkinje cell outputs selectively inhibit a subset of unipolar brush cells in the input layer of the cerebellar cortex. *ELife*, *10*, e68802. https://doi.org/10.7554/eLife.68802

Guo, C., Witter, L., Rudolph, S., Elliott, H. L., Ennis, K. A., & Regehr, W. G. (2016). Purkinje Cells Directly Inhibit Granule Cells in Specialized Regions of the Cerebellar Cortex. *Neuron*, *91*(6), 1330–1341. https://doi.org/10.1016/j.neuron.2016.08.011

Guo, J.-Z., Sauerbrei, B. A., Cohen, J. D., Mischiati, M., Graves, A. R., Pisanello, F., Branson, K. M., & Hantman, A. W. (2021). Disrupting cortico-cerebellar communication impairs dexterity. *ELife*, *10*, e65906. https://doi.org/10.7554/eLife.65906

Gurnani, H., & Silver, R. A. (2021). Multidimensional population activity in an electrically coupled inhibitory circuit in the cerebellar cortex. *Neuron*, *109*(10), 1739-1753.e8. https://doi.org/10.1016/j.neuron.2021.03.027

Halverson, H. E., Kim, J., Khilkevich, A., Mauk, M. D., & Augustine, G. J. (2022). Feedback inhibition underlies new computational functions of cerebellar interneurons. *ELife*, *11*, e77603. https://doi.org/10.7554/eLife.77603

Han, K.-S., Guo, C., Chen, C. H., Witter, L., Osorno, T., & Regehr, W. G. (2018). Ephaptic Coupling Promotes Synchronous Firing of Cerebellar Purkinje Cells. *Neuron*, *100*(3), 564-578.e3. https://doi.org/10.1016/j.neuron.2018.09.018

Hardy, N. F., & Buonomano, D. V. (2016). Neurocomputational models of interval and pattern timing. *Current Opinion in Behavioral Sciences*, *8*, 250–257. https://doi.org/10.1016/j.cobeha.2016.01.012

Harvey, R. J., & Napper, R. M. A. (1988). Quantitative study of granule and Purkinje cells in the cerebellar cortex of the rat. *The Journal of Comparative Neurology*, *274*(2), 151–157. https://doi.org/10.1002/cne.902740202

Harvey, R. J., & Napper, R. M. A. (1991). Quantitatives studies on the mammalian cerebellum. *Progress in Neurobiology*, *36*(6), 437–463. https://doi.org/10.1016/0301-0082(91)90012-P

Hashimoto, M., & Mikoshiba, K. (2003). Mediolateral Compartmentalization of the Cerebellum Is Determined on the "Birth Date" of Purkinje Cells. *The Journal of Neuroscience*, *23*(36), 11342–11351. https://doi.org/10.1523/JNEUROSCI.23-36-11342.2003

Häusser, M., & Clark, B. A. (1997). Tonic Synaptic Inhibition Modulates Neuronal Output Pattern and Spatiotemporal Synaptic Integration. *Neuron*, *19*(3), 665–678. https://doi.org/10.1016/S0896-6273(00)80379-7

Hawkes, R., Colonnier, M., & Leclerc, N. (1985). Monoclonal antibodies reveal sagittal banding in the rodent cerebellar cortex. *Brain Research*, *333*(2), 359–365. https://doi.org/10.1016/0006-8993(85)91593-8

Heiney, S. A., Kim, J., Augustine, G. J., & Medina, J. F. (2014). Precise Control of Movement Kinematics by Optogenetic Inhibition of Purkinje Cell Activity. *The Journal of Neuroscience*, *34*(6), 2321–2330. https://doi.org/10.1523/JNEUROSCI.4547-13.2014

Heiney, S. A., Wohl, M. P., Chettih, S. N., Ruffolo, L. I., & Medina, J. F. (2014). Cerebellar-Dependent Expression of Motor Learning during Eyeblink Conditioning in Head-Fixed Mice. *The Journal of Neuroscience*, *34*(45), 14845–14853. https://doi.org/10.1523/JNEUROSCI.2820-14.2014

Herculano-Houzel. (2010). Coordinated scaling of cortical and cerebellar numbers of neurons. *Frontiers in Neuroanatomy*. https://doi.org/10.3389/fnana.2010.00012

Hesslow, G. (1994). Correspondence between climbing fibre input and motor output in eyeblink-related areas in cat cerebellar cortex. *The Journal of Physiology*, *476*(2), 229–244. https://doi.org/10.1113/jphysiol.1994.sp020126

Hirono, M., Saitow, F., Kudo, M., Suzuki, H., Yanagawa, Y., Yamada, M., Nagao, S., Konishi, S., & Obata, K. (2012). Cerebellar Globular Cells Receive Monoaminergic Excitation and Monosynaptic Inhibition from Purkinje Cells. *PLoS ONE*, *7*(1), e29663. https://doi.org/10.1371/journal.pone.0029663

Ho, S., Lajaunie, R., Lerat, M., Le, M., Crépel, V., Loulier, K., Livet, J., Kessler, J.-P., & Marcaggi, P. (2021). A stable proportion of Purkinje cell inputs from parallel fibres are silent during cerebellar maturation. *Proceedings of the National Academy of Sciences*, *118*(45), e2024890118. https://doi.org/10.1073/pnas.2024890118

Hoehne, A., McFadden, M. H., & DiGregorio, D. A. (2020). Feed-forward recruitment of electrical synapses enhances synchronous spiking in the mouse cerebellar cortex. *ELife*, *9*, e57344. https://doi.org/10.7554/eLife.57344

Holmes, G. (1917). THE SYMPTOMS OF ACUTE CEREBELLAR INJURIES DUE TO GUNSHOT INJURIES. *Brain*, *40*(4), 461–535. https://doi.org/10.1093/brain/40.4.461

Houck, B. D., & Person, A. L. (2014). Cerebellar Loops: A Review of the Nucleocortical Pathway. *The Cerebellum*, *13*(3), 378–385. https://doi.org/10.1007/s12311-013-0543-2

Huang, C., Wang, L., & Huang, R. H. (2006). Cerebellar granule cell: Ascending axon and parallel fibre: Cerebellar granule cell axons. *European Journal of Neuroscience*, *23*(7), 1731–1737. https://doi.org/10.1111/j.1460-9568.2006.04690.x

Huang, C.-C., Sugino, K., Shima, Y., Guo, C., Bai, S., Mensh, B. D., Nelson, S. B., & Hantman, A. W. (2013). Convergence of pontine and proprioceptive streams onto multimodal cerebellar granule cells. *ELife*, *2*, e00400. https://doi.org/10.7554/eLife.00400

Hull, C., & Regehr, W. G. (2012). Identification of an Inhibitory Circuit that Regulates Cerebellar Golgi Cell Activity. *Neuron*, *73*(1), 149–158. https://doi.org/10.1016/j.neuron.2011.10.030

Hull, C., & Regehr, W. G. (2022). The Cerebellar Cortex. *The Annual Review of Neuroscience*, *45*, 151–175. https://doi.org/10.1146/annurev-neuro-091421125115

Ikeda, M., & Matsushita, M. (1992). Trigeminocerebellar projections to the posterior lobe in the cat, as studied by anterograde transport of wheat germ agglutinin-horseradish peroxidase. *The Journal of Comparative Neurology*, *316*(2), 221–237. https://doi.org/10.1002/cne.903160207

Isaacson, J. S., & Scanziani, M. (2011). How Inhibition Shapes Cortical Activity. *Neuron*, *72*(2), 231–243. https://doi.org/10.1016/j.neuron.2011.09.027

Ishikawa, T., Shimuta, M., & Häusser, M. (2015). Multimodal sensory integration in single cerebellar granule cells in vivo. *ELife*, *4*, e12916. https://doi.org/10.7554/eLife.12916

Isope, P., & Barbour, B. (2002). Properties of Unitary Granule Cell→Purkinje Cell Synapses in Adult Rat Cerebellar Slices. *The Journal of Neuroscience*, *22*(22), 9668–9678. https://doi.org/10.1523/JNEUROSCI.22-22-09668.2002

Ito, M. (1970). Neurophysiological aspects of the cerebellar motor control system. *International Journal of Neurology*, *7*(2), 162–176.

Ito, M. (1982). Cerebellar Control of the Vestibulo-Ocular Reflex—Around the Flocculus Hypothesis. *Annual Review of Neuroscience*, *5*(1), 275–297. https://doi.org/10.1146/annurev.ne.05.030182.001423

Ito, M. (2001). Cerebellar Long-Term Depression: Characterization, Signal Transduction, and Functional Roles. *Physiological Reviews*, *81*(3), 1143–1195. https://doi.org/10.1152/physrev.2001.81.3.1143

Ito, M. (2008). Control of mental activities by internal models in the cerebellum. *Nature Reviews Neuroscience*, *9*(4), 304–313. https://doi.org/10.1038/nrn2332

Ito, M., & Kano, M. (1982). Long-lasting depression of parallel fibre-Purkinje cell transmission induced by conjunctive stimulation of parallel fibres and climbing fibres in the cerebellar cortex. *Neuroscience Letters*, *33*(3), 253–258. https://doi.org/10.1016/0304-3940(82)90380-9

Jazayeri, M., & Ostojic, S. (2021). Interpreting neural computations by examining intrinsic and embedding dimensionality of neural activity. *Current Opinion in Neurobiology*, *70*, 113–120. https://doi.org/10.1016/j.conb.2021.08.002

Jeffress, L. A. (1948). A place theory of sound localization. *Journal of Comparative and Physiological Psychology*, *41*(1), 35–39. https://doi.org/10.1037/h0061495

Jelitai, M., Puggioni, P., Ishikawa, T., Rinaldi, A., & Duguid, I. (2016). Dendritic excitation–inhibition balance shapes cerebellar output during motor behaviour. *Nature Communications*, *7*(1), 13722. https://doi.org/10.1038/ncomms13722

Jirenhed, D.-A., Bengtsson, F., & Jörntell, H. (2013). Parallel fibre and climbing fibre responses in rat cerebellar cortical neurons in vivo. *Frontiers in Systems Neuroscience*, *7*. https://doi.org/10.3389/fnsys.2013.00016

Jörntell, H., & Ekerot, C.-F. (2006). Properties of Somatosensory Synaptic Integration in Cerebellar Granule Cells *In Vivo*. *The Journal of Neuroscience*, *26*(45), 11786–11797. https://doi.org/10.1523/JNEUROSCI.2939-06.2006

Jun, J. J., Steinmetz, N. A., Siegle, J. H., Denman, D. J., Bauza, M., Barbarits, B., Lee, A. K., Anastassiou, C. A., Andrei, A., Aydın, Ç., Barbic, M., Blanche, T. J., Bonin, V., Couto, J., Dutta, B., Gratiy, S. L., Gutnisky, D. A., Häusser, M., Karsh, B., … Harris, T. D. (2017). Fully integrated silicon probes for high-density recording of neural activity. *Nature*, *551*(7679), 232–236. https://doi.org/10.1038/nature24636

Kakegawa, W., Katoh, A., Narumi, S., Miura, E., Motohashi, J., Takahashi, A., Kohda, K., Fukazawa, Y., Yuzaki, M., & Matsuda, S. (2018). Optogenetic Control of Synaptic AMPA Receptor Endocytosis Reveals Roles of LTD in Motor Learning. *Neuron*, *99*(5), 985-998.e6. https://doi.org/10.1016/j.neuron.2018.07.034

Kalmbach, B. E., Davis, T., Ohyama, T., Riusech, F., Nores, W. L., & Mauk, M. D. (2010). Cerebellar Cortex Contributions to the Expression and Timing of Conditioned Eyelid Responses. *Journal of Neurophysiology*, *103*(4), 2039–2049. https://doi.org/10.1152/jn.00033.2010

Kanichay, R. T., & Silver, R. A. (2008). Synaptic and Cellular Properties of the Feedforward Inhibitory Circuit within the Input Layer of the Cerebellar Cortex. *The Journal of Neuroscience*, *28*(36), 8955–8967. https://doi.org/10.1523/JNEUROSCI.5469-07.2008

Karnani, M. M., Jackson, J., Ayzenshtat, I., Hamzehei Sichani, A., Manoocheri, K., Kim, S., & Yuste, R. (2016). Opening Holes in the Blanket of Inhibition: Localized Lateral Disinhibition by VIP Interneurons. *The Journal of Neuroscience*, *36*(12), 3471–3480. https://doi.org/10.1523/JNEUROSCI.3646-15.2016

Kebschull, J. M., Richman, E. B., Ringach, N., Friedmann, D., Albarran, E., Kolluru, S. S., Jones, R. C., Allen, W. E., Wang, Y., Cho, S. W., Zhou, H., Ding, J. B., Chang, H. Y., Deisseroth, K., Quake, S. R., & Luo, L. (2020). Cerebellar nuclei evolved by repeatedly duplicating a conserved cell-type set. *Science*, *370*(6523), eabd5059. https://doi.org/10.1126/science.abd5059

Kelly, R. M., & Strick, P. L. (2003). Cerebellar Loops with Motor Cortex and Prefrontal Cortex of a Nonhuman Primate. *The Journal of Neuroscience*, *23*(23), 8432–8444. https://doi.org/10.1523/JNEUROSCI.23-23-08432.2003

Kennedy, A., Wayne, G., Kaifosh, P., Alviña, K., Abbott, L. F., & Sawtell, N. B. (2014). A temporal basis for predicting the sensory consequences of motor commands in an electric fish. *Nature Neuroscience*, *17*(3), 3. https://doi.org/10.1038/nn.3650

Kieffer, B. L. (2009). Opioid Peptides and Receptors. In *Encyclopedia of Neuroscience* (pp. 235–240). Elsevier. https://doi.org/10.1016/B978-008045046-9.01472-8

Kim, J., & Augustine, G. J. (2021). Molecular Layer Interneurons: Key Elements of Cerebellar Network Computation and Behavior. *Neuroscience*, *462*, 22–35. https://doi.org/10.1016/j.neuroscience.2020.10.008

Kim, J., Lee, S., Tsuda, S., Zhang, X., Asrican, B., Gloss, B., Feng, G., & Augustine, G. J. (2014). Optogenetic Mapping of Cerebellar Inhibitory Circuitry Reveals Spatially Biased Coordination of Interneurons via Electrical Synapses. *Cell Reports*, *7*(5), 1601–1613. https://doi.org/10.1016/j.celrep.2014.04.047

Kim, T., Park, H., Tanaka-Yamamoto, K., & Yamamoto, Y. (2023). Developmental timing-dependent organization of synaptic connections between mossy fibres and granule cells in the cerebellum. *Communications Biology*, *6*(1), 446. https://doi.org/10.1038/s42003-023-04825-y

Kleinfeld, D., Moore, J. D., Wang, F., & Deschênes, M. (2014). The Brainstem Oscillator for Whisking and the Case for Breathing as the Master Clock for Orofacial Motor Actions. *Cold Spring Harbor Symposia on Quantitative Biology*, *79*, 29–39. https://doi.org/10.1101/sqb.2014.79.024794

Kloth, A. D., Badura, A., Li, A., Cherskov, A., Connolly, S. G., Giovannucci, A., Bangash, M. A., Grasselli, G., Peñagarikano, O., Piochon, C., Tsai, P. T., Geschwind, D. H., Hansel, C., Sahin, M., Takumi, T., Worley, P. F., & Wang, S. S.-H. (2015). Cerebellar associative sensory learning defects in five mouse autism models. *ELife*, *4*, e06085. https://doi.org/10.7554/eLife.06085

Kondo, S., & Marty, A. (1998a). Differential effects of noradrenaline on evoked, spontaneous and miniature IPSCs in rat cerebellar stellate cells. *The Journal of Physiology*, *509*(1), 233–243. https://doi.org/10.1111/j.1469-7793.1998.233bo.x

Kondo, S., & Marty, A. (1998b). Synaptic currents at individual connections among stellate cells in rat cerebellar slices. *The Journal of Physiology*, *509*(1), 221–232. https://doi.org/10.1111/j.1469-7793.1998.221bo.x

Korbo, L., Andersen, B. B., Ladefoged, O., & Møller, A. (1993). Total numbers of various cell types in rat cerebellar cortex estimated using an unbiased stereological method. *Brain Research*, *609*(1–2), 262–268. https://doi.org/10.1016/0006-8993(93)90881-M

Kostadinov, D., & Häusser, M. (2022). Reward signals in the cerebellum: Origins, targets, and functional implications. *Neuron*, *110*(8), 1290–1303. https://doi.org/10.1016/j.neuron.2022.02.015

Kozareva, V., Martin, C., Osorno, T., Rudolph, S., Guo, C., Vanderburg, C., Nadaf, N., Regev, A., Regehr, W. G., & Macosko, E. (2021). A transcriptomic atlas of mouse cerebellar cortex comprehensively defines cell types. *Nature*, *598*(7879), 214–219. https://doi.org/10.1038/s41586-021-03220-z

Krabbe, S., Paradiso, E., d'Aquin, S., Bitterman, Y., Courtin, J., Xu, C., Yonehara, K., Markovic, M., Müller, C., Eichlisberger, T., Gründemann, J., Ferraguti, F., & Lüthi, A. (2019). Adaptive disinhibitory gating by VIP interneurons permits associative learning. *Nature Neuroscience*, *22*(11), 1834–1843. https://doi.org/10.1038/s41593-019-0508-y

Krieger, C., Shinoda, Y., & Smith, A. M. (1985). Labelling of cerebellar mossy fibre afferents with intra-axonal horseradish peroxidase. *Experimental Brain Research*, *59*(2). https://doi.org/10.1007/BF00230923

Kuhn, B., Ozden, I., Lampi, Y., Hasan, M. T., & Wang, S. S.-H. (2012). An amplified promoter system for targeted expression of calcium indicator proteins in the cerebellar cortex. *Frontiers in Neural Circuits*, *6*. https://doi.org/10.3389/fncir.2012.00049

Lainé, J., & Axelrad, H. (1994). The candelabrum cell: A new interneuron in the cerebellar cortex: CEREBELLAR CORTEX CANDELABRUM INTERNEURON. *Journal of Comparative Neurology*, *339*(2), 159–173. https://doi.org/10.1002/cne.903390202

Lainé, J., & Axelrad, H. (2002). Extending the cerebellar Lugaro cell class. *Neuroscience*, *115*(2), 363–374. https://doi.org/10.1016/S0306-4522(02)00421-9

Leergaard, T. B., Alloway, K. D., Pham, T. A. T., Bolstad, I., Hoffer, Z. S., Pettersen, C., & Bjaalie, J. G. (2004). Three-dimensional topography of corticopontine projections from rat sensorimotor cortex: Comparisons with corticostriatal projections reveal diverse integrative organization. *The Journal of Comparative Neurology*, *478*(3), 306–322. https://doi.org/10.1002/cne.20289

Lein, E. S., Hawrylycz, M. J., Ao, N., Ayres, M., Bensinger, A., Bernard, A., Boe, A. F., Boguski, M. S., Brockway, K. S., Byrnes, E. J., Chen, L., Chen, L., Chen, T.-M., Chin, M. C., Chong, J., Crook, B. E., Czaplinska, A., Dang, C. N., Datta, S., … Jones, A. R. (2007). *Genome-wide atlas of gene expression in the adult mouse brain*. *445*.

Lemkey-Johnston, N., & Larramendi, L. M. H. (1968a). Morphological characteristics of mouse stellate and basket cells and their neuroglial envelope: An electron microscopic study. *The Journal of Comparative Neurology*, *134*(1), 39–71. https://doi.org/10.1002/cne.901340105

Lemkey-Johnston, N., & Larramendi, L. M. H. (1968b). Types and distribution of synapses upon basket and stellate cells of the mouse cerebellum: An electron microscopic study. *The Journal of Comparative Neurology*, *134*(1), 73–111. https://doi.org/10.1002/cne.901340106

Leto, K., Arancillo, M., Becker, E. B. E., Buffo, A., Chiang, C., Ding, B., Dobyns, W. B., Dusart, I., Haldipur, P., Hatten, M. E., Hoshino, M., Joyner, A. L., Kano, M., Kilpatrick, D. L., Koibuchi, N., Marino, S., Martinez, S., Millen, K. J., Millner, T. O., … Hawkes, R. (2016). Consensus Paper: Cerebellar Development. *The Cerebellum*, *15*(6), 789–828. https://doi.org/10.1007/s12311-015-0724-2

Li, X., Zhang, G., Wu, J., Zhang, Y., Zhao, Z., Lin, X., Qiao, H., Xie, H., Wang, H., Fang, L., & Dai, Q. (2021). Reinforcing neuron extraction and spike inference in calcium imaging using deep self-supervised denoising. *Nature Methods*, *18*(11), 1395–1400. https://doi.org/10.1038/s41592-021-01225-0

Lim, L., Mi, D., Llorca, A., & Marín, O. (2018). Development and Functional Diversification of Cortical Interneurons. *Neuron*, *100*(2), 294–313. https://doi.org/10.1016/j.neuron.2018.10.009

Lindeman, S., Hong, S., Kros, L., Mejias, J. F., Romano, V., Oostenveld, R., Negrello, M., Bosman, L. W. J., & De Zeeuw, C. I. (2021). Cerebellar Purkinje cells can differentially modulate coherence between sensory and motor cortex depending on region and behavior. *Proceedings*

of the National Academy of Sciences, *118*(2), e2015292118. https://doi.org/10.1073/pnas.2015292118

Lisberger, S. G., Pavelko, T. A., Bronte-Stewart, H. M., & Stone, L. S. (1994). Neural basis for motor learning in the vestibuloocular reflex of primates. II. Changes in the responses of horizontal gaze velocity Purkinje cells in the cerebellar flocculus and ventral paraflocculus. *Journal of Neurophysiology*, *72*(2), 954–973. https://doi.org/10.1152/jn.1994.72.2.954

Liu, Y., Formisano, L., Savtchouk, I., Takayasu, Y., Szabó, G., Zukin, R. S., & Liu, S. J. (2010). A single fear-inducing stimulus induces a transcription-dependent switch in synaptic AMPAR phenotype. *Nature Neuroscience*, *13*(2), 223–231. https://doi.org/10.1038/nn.2474

Liu, Z., Lu, X., Villette, V., Gou, Y., Colbert, K. L., Lai, S., Guan, S., Land, M. A., Lee, J., Assefa, T., Zollinger, D. R., Korympidou, M. M., Vlasits, A. L., Pang, M. M., Su, S., Cai, C., Froudarakis, E., Zhou, N., Patel, S. S., … St-Pierre, F. (2022). Sustained deep-tissue voltage recording using a fast indicator evolved for two-photon microscopy. *Cell*, *185*(18), 3408-3425.e29. https://doi.org/10.1016/j.cell.2022.07.013

Llinas, R., & Sasaki, K. (1989). The Functional Organization of the Olivo-Cerebellar System as Examined by Multiple Purkinje Cell Recordings. *European Journal of Neuroscience*, *1*(6), 587–602. https://doi.org/10.1111/j.1460-9568.1989.tb00365.x

Long, M. A., Jin, D. Z., & Fee, M. S. (2010). Support for a synaptic chain model of neuronal sequence generation. *Nature*, *468*(7322), 7322. https://doi.org/10.1038/nature09514

Ma, M., Futia, G. L., De Souza, F. M. S., Ozbay, B. N., Llano, I., Gibson, E. A., & Restrepo, D. (2020). Molecular layer interneurons in the cerebellum encode for valence in associative learning. *Nature Communications*, *11*(1), 4217. https://doi.org/10.1038/s41467-020-18034-2

Mahn, M., Gibor, L., Patil, P., Cohen-Kashi Malina, K., Oring, S., Printz, Y., Levy, R., Lampl, I., & Yizhar, O. (2018). High-efficiency optogenetic silencing with soma-targeted anion-conducting channelrhodopsins. *Nature Communications*, *9*(1), 4125. https://doi.org/10.1038/s41467-018-06511-8

Markwalter, K. H., Yang, Y., Holy, T. E., & Bonni, A. (2019). Sensorimotor Coding of Vermal Granule Neurons in the Developing Mammalian Cerebellum. *The Journal of Neuroscience*, *39*(34), 6626–6643. https://doi.org/10.1523/JNEUROSCI.0086-19.2019

Marr, D. (1969). A THEORY OF CEREBELLAR CORTEX. *J Physiol (Lond)*, *202*, 437–470. https://doi.org/10.1113/jphysiol.1969.sp008820.

Marshall-Phelps, K. L. H., Riedel, G., Wulff, P., & Woloszynowska-Fraser, M. (2020). Cerebellar molecular layer interneurons are dispensable for cued and contextual fear conditioning. *Scientific Reports*, *10*(1), 20000. https://doi.org/10.1038/s41598-020-76729-4

Matsushita, M., & Hosoya, Y. (1979). Cells of origin of the spinocerebellar tract in the rat, studied with the method of retrograde transport of horseradish peroxidase. *Brain Research*, *173*(2), 185–200. https://doi.org/10.1016/0006-8993(79)90620-6

Mauk, M. D., & Donegan, N. H. (1997). A model of Pavlovian eyelid conditioning based on the synaptic organization of the cerebellum. *Learning & Memory (Cold Spring Harbor, N.Y.)*, *4*(1), 130–158. https://doi.org/10.1101/lm.4.1.130

McCormick, D. A., & Thompson, R. F. (1984). Cerebellum: Essential Involvement in the Classically Conditioned Eyelid Response. *Science*, *223*(4633), 296–299. https://doi.org/10.1126/science.6701513

Medina, J. F. (2011). The multiple roles of Purkinje cells in sensori-motor calibration: To predict, teach and command. *Current Opinion in Neurobiology*, *21*(4), 616–622. https://doi.org/10.1016/j.conb.2011.05.025

Medina, J. F., Nores, W. L., Ohyama, T., & Mauk, M. D. (2000). Mechanisms of cerebellar learning suggested by eyelid conditioning. *Current Opinion in Neurobiology*, *10*(6), 717–724. https://doi.org/10.1016/S0959-4388(00)00154-9

Meng, H., Blázquez, P. M., Dickman, J. D., & Angelaki, D. E. (2014). Diversity of vestibular nuclei neurons targeted by cerebellar nodulus inhibition: Vestibular neurons targeted by nodulus inhibition. *The Journal of Physiology*, *592*(1), 171–188. https://doi.org/10.1113/jphysiol.2013.259614

Miles, F. A., & Lisberger, S. G. (1981). Plasticity in the Vestibulo-Ocular Reflex: A New Hypothesis. *Annual Review of Neuroscience*, *4*(1), 273–299. https://doi.org/10.1146/annurev.ne.04.030181.001421

Mittmann, W., Koch, U., & Häusser, M. (2005). Feed-forward inhibition shapes the spike output of cerebellar Purkinje cells: Feed-forward inhibition in the cerebellar cortex. *The Journal of Physiology*, *563*(2), 369–378. https://doi.org/10.1113/jphysiol.2004.075028

Miyazaki, T., Yamasaki, M., Tanaka, K. F., & Watanabe, M. (2021). Compartmentalized Input–Output Organization of Lugaro Cells in the Cerebellar Cortex. *Neuroscience*, *462*, 89–105. https://doi.org/10.1016/j.neuroscience.2020.05.026

Moberget, T., & Ivry, R. B. (2016). Cerebellar contributions to motor control and language comprehension: Searching for common computational principles: Cerebellar contributions to motor control and language. *Annals of the New York Academy of Sciences*, *1369*(1), 154–171. https://doi.org/10.1111/nyas.13094

Monteiro, T., Rodrigues, F. S., Pexirra, M., Cruz, B. F., Gonçalves, A. I., Rueda-Orozco, P. E., & Paton, J. J. (2023). Using temperature to analyze the neural basis of a time-based decision. *Nature Neuroscience*, *26*(8), 1407–1416. https://doi.org/10.1038/s41593-023-01378-5

Morissette, J., & Bower, JamesM. (1996). Contribution of somatosensory cortex to responses in the rat cerebellar granule cell layer following peripheral tactile stimulation. *Experimental Brain Research*, *109*(2). https://doi.org/10.1007/BF00231784

Mugnaini, E., Sekerková, G., & Martina, M. (2011). The unipolar brush cell: A remarkable neuron finally receiving deserved attention. *Brain Research Reviews*, *66*(1–2), 220–245. https://doi.org/10.1016/j.brainresrev.2010.10.001

Muñoz-Manchado, A. B., Bengtsson Gonzales, C., Zeisel, A., Munguba, H., Bekkouche, B., Skene, N. G., Lönnerberg, P., Ryge, J., Harris, K. D., Linnarsson, S., & Hjerling-Leffler, J. (2018). Diversity of Interneurons in the Dorsal Striatum Revealed by Single-Cell RNA Sequencing and PatchSeq. *Cell Reports*, *24*(8), 2179-2190.e7. https://doi.org/10.1016/j.celrep.2018.07.053

Nagao, S. (2004). Pontine nuclei-mediated cerebello-cerebral interactions and its functional role. *The Cerebellum*, *3*(1), 11–15. https://doi.org/10.1080/14734220310012181

Najac, M., & Raman, I. M. (2017). Synaptic excitation by climbing fibre collaterals in the cerebellar nuclei of juvenile and adult mice: Climbing fibre collateral EPSCs in the CbN. *The Journal of Physiology*, *595*(21), 6703–6718. https://doi.org/10.1113/JP274598

Nedelescu, H., Abdelhack, M., & Pritchard, A. T. (2018). Regional differences in Purkinje cell morphology in the cerebellar vermis of male mice. *Journal of Neuroscience Research*, *96*(9), 1476–1489. https://doi.org/10.1002/jnr.24206

Nietz, A. K., Vaden, J. H., Coddington, L. T., Overstreet-Wadiche, L., & Wadiche, J. I. (2017). Non-synaptic signaling from cerebellar climbing fibres modulates Golgi cell activity. *ELife*, *6*, e29215. https://doi.org/10.7554/eLife.29215

Ohyama, T., Nores, W. L., Murphy, M., & Mauk, M. D. (2003). What the cerebellum computes. *Trends in Neurosciences*, *26*(4), 222–227. https://doi.org/10.1016/S0166-2236(03)00054-7

Ono, S., Kushiro, K., Zakir, M., Meng, H., Sato, H., & Uchino, Y. (2000). Properties of utricular and saccular nerve-activated vestibulocerebellar neurons in cats. *Experimental Brain Research*, *134*(1), 1–8. https://doi.org/10.1007/s002210000424

Orduz, D., & Llano, I. (2007). Recurrent axon collaterals underlie facilitating synapses between cerebellar Purkinje cells. *Proceedings of the National Academy of Sciences*, *104*(45), 17831–17836. https://doi.org/10.1073/pnas.0707489104

Oscarsson, O. (1979). Functional units of the cerebellum—Sagittal zones and microzones. *Trends in Neurosciences*, *2*, 143–145. https://doi.org/10.1016/0166-2236(79)90057-2

Osorno, T., Rudolph, S., Nguyen, T., Kozareva, V., Nadaf, N., Macosko, E. Z., Lee, W.-C. A., & Regehr, W. G. (2021). *Candelabrum cells are molecularly distinct, ubiquitous interneurons of the cerebellar cortex with specialized circuit properties* [Preprint]. Neuroscience. https://doi.org/10.1101/2021.04.09.439172

Pachitariu, M., Stringer, C., Dipoppa, M., Schröder, S., Rossi, L. F., Dalgleish, H., Carandini, M., & Harris, K. D. (2016). *Suite2p: Beyond 10,000 neurons with standard two-photon microscopy* [Preprint]. Neuroscience. https://doi.org/10.1101/061507

Palay, S. L., & Chan-Palay, V. (1974). *Cerebellar Cortex*. Springer Berlin Heidelberg. https://doi.org/10.1007/978-3-642-65581-4

Paton, J. J., & Buonomano, D. V. (2018). The Neural Basis of Timing: Distributed Mechanisms for Diverse Functions. *Neuron*, *98*(4), 687–705. https://doi.org/10.1016/j.neuron.2018.03.045

Paukert, M., Huang, Y. H., Tanaka, K., Rothstein, J. D., & Bergles, D. E. (2010). Zones of Enhanced Glutamate Release from Climbing Fibres in the Mammalian Cerebellum. *The Journal of Neuroscience*, *30*(21), 7290–7299. https://doi.org/10.1523/JNEUROSCI.5118-09.2010

Perrett, S. P., Ruiz, B. P., & Mauk, M. D. (1993). Cerebellar cortex lesions disrupt learning-dependent timing of conditioned eyelid responses. *Journal of Neuroscience*, *13*(4), 1708–1718. https://doi.org/10.1523/JNEUROSCI.13-04-01708.1993

Person, A. L., & Raman, I. M. (2012). Purkinje neuron synchrony elicits time-locked spiking in the cerebellar nuclei. *Nature*, *481*(7382), 502–505. https://doi.org/10.1038/nature10732

Pichitpornchai, C., Rawson, J. A., & Rees, S. (1994). Morphology of parallel fibres in the cerebellar cortex of the rat: An experimental light and electron microscopic study with biocytin. *The Journal of Comparative Neurology*, *342*(2), 206–220. https://doi.org/10.1002/cne.903420205

Picot, A., Dominguez, S., Liu, C., Chen, I.-W., Tanese, D., Ronzitti, E., Berto, P., Papagiakoumou, E., Oron, D., Tessier, G., Forget, B. C., & Emiliani, V. (2018). Temperature Rise under Two-Photon Optogenetic Brain Stimulation. *Cell Reports*, *24*(5), 1243-1253.e5. https://doi.org/10.1016/j.celrep.2018.06.119

Pouille, F., & Scanziani, M. (2001). Enforcement of Temporal Fidelity in Pyramidal Cells by Somatic Feed-Forward Inhibition. *Science*, *293*(5532), 1159–1163. https://doi.org/10.1126/science.1060342

Pouzat, C., & Marty, A. (1998). Autaptic inhibitory currents recorded from interneurones in rat cerebellar slices. *The Journal of Physiology*, *509*(3), 777–783. https://doi.org/10.1111/j.1469-7793.1998.777bm.x

Powell, K., Mathy, A., Duguid, I., & Häusser, M. (2015). Synaptic representation of locomotion in single cerebellar granule cells. *ELife*, *4*, e07290. https://doi.org/10.7554/eLife.07290

Proville, R. D., Spolidoro, M., Guyon, N., Dugué, G. P., Selimi, F., Isope, P., Popa, D., & Léna, C. (2014). Cerebellum involvement in cortical sensorimotor circuits for the control of voluntary movements. *Nature Neuroscience*, *17*(9), 1233–1239. https://doi.org/10.1038/nn.3773

Quy, P. N., Fujita, H., Sakamoto, Y., Na, J., & Sugihara, I. (2011). Projection patterns of single mossy fibre axons originating from the dorsal column nuclei mapped on the aldolase C compartments in the rat cerebellar cortex. *The Journal of Comparative Neurology*, *519*(5), 874–899. https://doi.org/10.1002/cne.22555

Rahimi-Balaei, M., Bergen, H., Kong, J., & Marzban, H. (2018). Neuronal Migration During Development of the Cerebellum. *Frontiers in Cellular Neuroscience*, *12*, 484. https://doi.org/10.3389/fncel.2018.00484

Rancz, E. A., Ishikawa, T., Duguid, I., Chadderton, P., Mahon, S., & Häusser, M. (2007). High-fidelity transmission of sensory information by single cerebellar mossy fibre boutons. *Nature*, *450*(7173), 1245–1248. https://doi.org/10.1038/nature05995

Raymond, J. L., Lisberger, S. G., & Mauk, M. D. (1996). The Cerebellum: A Neuronal Learning Machine? *Science*, *272*(5265), 1126–1131. https://doi.org/10.1126/science.272.5265.1126

Raymond, J. L., & Medina, J. F. (2018). Computational Principles of Supervised Learning in the Cerebellum. *Annual Review of Neuroscience*, *41*(1), 233–253. https://doi.org/10.1146/annurev-neuro-080317-061948

Reeber, S. L., Loeschel, C. A., Franklin, A., & Sillitoe, R. V. (2013). Establishment of topographic circuit zones in the cerebellum of scrambler mutant mice. *Frontiers in Neural Circuits*, *7*. https://doi.org/10.3389/fncir.2013.00122

Rieubland, S., Roth, A., & Häusser, M. (2014). Structured Connectivity in Cerebellar Inhibitory Networks. *Neuron*, *81*(4), 913–929. https://doi.org/10.1016/j.neuron.2013.12.029

Rodriques, S. G., Stickels, R. R., Goeva, A., Martin, C. A., Murray, E., Vanderburg, C. R., Welch, J., Chen, L. M., Chen, F., & Macosko, E. Z. (2020). *Slide-seq: A Scalable Technology for Measuring Genome-Wide Expression at High Spatial Resolution*.

Romano, V., De Propris, L., Bosman, L. W., Warnaar, P., Ten Brinke, M. M., Lindeman, S., Ju, C., Velauthapillai, A., Spanke, J. K., Middendorp Guerra, E., Hoogland, T. M., Negrello, M., D'Angelo, E., & De Zeeuw, C. I. (2018). Potentiation of cerebellar Purkinje cells facilitates whisker reflex adaptation through increased simple spike activity. *ELife*, *7*, e38852. https://doi.org/10.7554/eLife.38852

Rondi-Reig, L., Paradis, A.-L., Lefort, J. M., Babayan, B. M., & Tobin, C. (2014). How the cerebellum may monitor sensory information for spatial representation. *Frontiers in Systems Neuroscience*, *8*. https://doi.org/10.3389/fnsys.2014.00205

Rössert, C., Dean, P., & Porrill, J. (2015). At the Edge of Chaos: How Cerebellar Granular Layer Network Dynamics Can Provide the Basis for Temporal Filters. *PLOS Computational Biology*, *11*(10), e1004515. https://doi.org/10.1371/journal.pcbi.1004515

Rowan, M. J. M., Bonnan, A., Zhang, K., Amat, S. B., Kikuchi, C., Taniguchi, H., Augustine, G. J., & Christie, J. M. (2018). Graded Control of Climbing-Fibre-Mediated Plasticity and Learning by Inhibition in the Cerebellum. *Neuron*, *99*(5), 999-1015.e6. https://doi.org/10.1016/j.neuron.2018.07.024

Ruigrok, T. J. H., Hensbroek, R. A., & Simpson, J. I. (2011). Spontaneous Activity Signatures of Morphologically Identified Interneurons in the Vestibulocerebellum. *The Journal of Neuroscience*, *31*(2), 712–724. https://doi.org/10.1523/JNEUROSCI.1959-10.2011

Rupprecht, P., Carta, S., Hoffmann, A., Echizen, M., Blot, A., Kwan, A. C., Dan, Y., Hofer, S. B., Kitamura, K., Helmchen, F., & Friedrich, R. W. (2021). A database and deep learning toolbox for noise-optimized, generalized spike inference from calcium imaging. *Nature Neuroscience*, *24*(9), 1324–1337. https://doi.org/10.1038/s41593-021-00895-5

Salomé, R., Kremer, Y., Dieudonné, S., Léger, J.-F., Krichevsky, O., Wyart, C., Chatenay, D., & Bourdieu, L. (2006). Ultrafast random-access scanning in two-photon microscopy using acousto-optic deflectors. *Journal of Neuroscience Methods*, *154*(1–2), 161–174. https://doi.org/10.1016/j.jneumeth.2005.12.010

Sawtell, N. B. (2017). Neural Mechanisms for Predicting the Sensory Consequences of Behavior: Insights from Electrosensory Systems. *Annual Review of Physiology*, *79*(1), 381–399. https://doi.org/10.1146/annurev-physiol-021115-105003

Schilling, K. (2022). Specification and Development of GABAergic Interneurons. In M. U. Manto, D. L. Gruol, J. D. Schmahmann, N. Koibuchi, & R. V. Sillitoe (Eds.), *Handbook of the Cerebellum and Cerebellar Disorders* (pp. 235–264). Springer International Publishing. https://doi.org/10.1007/978-3-030-23810-0_11

Schindelin, J., Arganda-Carreras, I., Frise, E., Kaynig, V., Longair, M., Pietzsch, T., Preibisch, S., Rueden, C., Saalfeld, S., Schmid, B., Tinevez, J.-Y., White, D. J., Hartenstein, V., Eliceiri, K., Tomancak, P., & Cardona, A. (2012). Fiji: An open-source platform for biological-image analysis. *FOCUS ON BIOIMAGE INFORMATICS*.

Schmahmann, J. D. (2019). The cerebellum and cognition. *Neuroscience Letters*, *688*, 62–75. https://doi.org/10.1016/j.neulet.2018.07.005

Schmidt, E., & Oheim, M. (2020). Infrared Excitation Induces Heating and Calcium Microdomain Hyperactivity in Cortical Astrocytes. *Biophysical Journal*, *119*(11), 2153–2165. https://doi.org/10.1016/j.bpj.2020.10.027

Schonewille, M., Gao, Z., Boele, H.-J., Vinueza Veloz, M. F., Amerika, W. E., Šimek, A. A. M., De Jeu, M. T., Steinberg, J. P., Takamiya, K., Hoebeek, F. E., Linden, D. J., Huganir, R. L., & De Zeeuw, C. I. (2011). Reevaluating the Role of LTD in Cerebellar Motor Learning. *Neuron*, *70*(1), 43–50. https://doi.org/10.1016/j.neuron.2011.02.044

Schulz, J. M., Knoflach, F., Hernandez, M.-C., & Bischofberger, J. (2018). Dendrite-targeting interneurons control synaptic NMDA-receptor activation via nonlinear α5-GABAA receptors. *Nature Communications*, *9*(1), 3576. https://doi.org/10.1038/s41467-018-06004-8

Scott, T. G. (1965). THE SPECIFICITY OF 5'-NUCLEOTIDASE IN THE BRAIN OF THE MOUSE. *Journal of Histochemistry & Cytochemistry*, *13*(8), 657–667. https://doi.org/10.1177/13.8.657

Serapide, M. F., Pant, M. R., Parenti, R., Zappal, A., & Cicirata, F. (2001). Multiple zonal projections of the basilar pontine nuclei to the cerebellar cortex of the rat. *The Journal of Comparative Neurology*, *430*(4), 471–484. https://doi.org/10.1002/1096-9861(20010219)430:4<471::AID-CNE1044>3.0.CO;2-G

Sereno, M. I., Diedrichsen, J., Tachrount, M., Testa-Silva, G., d'Arceuil, H., & De Zeeuw, C. (2020). The human cerebellum has almost 80% of the surface area of the neocortex. *Proceedings of the National Academy of Sciences*, *117*(32), 19538–19543. https://doi.org/10.1073/pnas.2002896117

Shambes, G. M., Gibson, J. M., & Welker, W. (1978). Fractured Somatotopy in Granule Cell Tactile Areas of Rat Cerebellar Hemispheres Revealed by Micromapping; pp. 94–105. *Brain Behavior and Evolution*, *15*(2), 94–105. https://doi.org/10.1159/000123774

Shinoda, Y., Sugihara, I., Wu, H.-S., & Sugiuchi, Y. (2000). The entire trajectory of single climbing and mossy fibres in the cerebellar nuclei and cortex. In *Progress in Brain Research* (Vol. 124, pp. 173–186). Elsevier. https://doi.org/10.1016/S0079-6123(00)24015-6

Shuster, S. A., Wagner, M. J., Pan-Doh, N., Ren, J., Grutzner, S. M., Beier, K. T., Kim, T. H., Schnitzer, M. J., & Luo, L. (2021). The relationship between birth timing, circuit wiring, and physiological response properties of cerebellar granule cells. *Proceedings of the National Academy of Sciences*, *118*(23), e2101826118. https://doi.org/10.1073/pnas.2101826118

Sotelo, C. (2003). Viewing the brain through the master hand of Ramon y Cajal. *Nature Reviews Neuroscience*, *4*(1), 71–77. https://doi.org/10.1038/nrn1010

Sotelo, C. (2004). Cellular and genetic regulation of the development of the cerebellar system. *Progress in Neurobiology*, *72*(5), 295–339. https://doi.org/10.1016/j.pneurobio.2004.03.004

Sotelo, C., Bourrat, F., & Triller, A. (1984). Postnatal development of the inferior olivary complex in the rat. II. Topographic organization of the immature olivocerebellar projection. *The Journal of Comparative Neurology*, *222*(2), 177–199. https://doi.org/10.1002/cne.902220204

Spanne, A., & Jörntell, H. (2015). Questioning the role of sparse coding in the brain. *Trends in Neurosciences*, *38*(7), 417–427. https://doi.org/10.1016/j.tins.2015.05.005

Steinmetz, J. E., Lavond, D. G., & Thompson, R. F. (1989). Classical conditioning in rabbits using pontine nucleus stimulation as a conditioned stimulus and inferior olive stimulation as an unconditioned stimulus. *Synapse*, *3*(3), 225–233. https://doi.org/10.1002/syn.890030308

Stoodley, C. J., D'Mello, A. M., Ellegood, J., Jakkamsetti, V., Liu, P., Nebel, M. B., Gibson, J. M., Kelly, E., Meng, F., Cano, C. A., Pascual, J. M., Mostofsky, S. H., Lerch, J. P., & Tsai, P. T. (2017). Altered cerebellar connectivity in autism and cerebellar-mediated rescue of autism-related behaviors in mice. *Nature Neuroscience*, *20*(12), 1744–1751. https://doi.org/10.1038/s41593-017-0004-1

Straub, I., Witter, L., Eshra, A., Hoidis, M., Byczkowicz, N., Maas, S., Delvendahl, I., Dorgans, K., Savier, E., Bechmann, I., Krueger, M., Isope, P., & Hallermann, S. (2020). Gradients in the mammalian cerebellar cortex enable Fourier-like transformation and improve storing capacity. *ELife*, *9*, e51771. https://doi.org/10.7554/eLife.51771

Sugihara, I. (2018). Crus I in the Rodent Cerebellum: Its Homology to Crus I and II in the Primate Cerebellum and Its Anatomical Uniqueness Among Neighboring Lobules. *The Cerebellum*, *17*(1), 49–55. https://doi.org/10.1007/s12311-017-0911-4

Sugihara, I., & Shinoda, Y. (2004). Molecular, Topographic, and Functional Organization of the Cerebellar Cortex: A Study with Combined Aldolase C and Olivocerebellar Labeling. *The Journal of Neuroscience*, *24*(40), 8771–8785. https://doi.org/10.1523/JNEUROSCI.1961-04.2004

Sultan, F., & Bower, J. M. (1998). Quantitative Golgi study of the rat cerebellar molecular layer interneurons using principal component analysis. *The Journal of Comparative Neurology*, *393*(3), 353–373. https://doi.org/10.1002/(SICI)1096-9861(19980413)393:3<353::AID-CNE7>3.0.CO;2-0

Sun, S., & Schaffer, D. V. (2018). Engineered viral vectors for functional interrogation, deconvolution, and manipulation of neural circuits. *Current Opinion in Neurobiology*, *50*, 163–170. https://doi.org/10.1016/j.conb.2017.12.011

Szapiro, G., & Barbour, B. (2007). Multiple climbing fibres signal to molecular layer interneurons exclusively via glutamate spillover. *Nature Neuroscience*, *10*(6), 735–742. https://doi.org/10.1038/nn1907

Takatoh, J., Nelson, A., Zhou, X., Bolton, M. M., Ehlers, M. D., Arenkiel, B. R., Mooney, R., & Wang, F. (2013). New Modules Are Added to Vibrissal Premotor Circuitry with the Emergence of Exploratory Whisking. *Neuron*, *77*(2), 346–360. https://doi.org/10.1016/j.neuron.2012.11.010

Tam, W. Y., Wang, X., Cheng, A. S. K., & Cheung, K.-K. (2021). In Search of Molecular Markers for Cerebellar Neurons. *Int. J. Mol. Sci.*

ten Brinke, M. M., Boele, H.-J., Spanke, J. K., Potters, J.-W., Kornysheva, K., Wulff, P., IJpelaar, A. C. H. G., Koekkoek, S. K. E., & De Zeeuw, C. I. (2015). Evolving Models of Pavlovian Conditioning: Cerebellar Cortical Dynamics in Awake Behaving Mice. *Cell Reports*, *13*(9), 1977–1988. https://doi.org/10.1016/j.celrep.2015.10.057

Tiganj, Z., Jung, M. W., Kim, J., & Howard, M. W. (2017). Sequential Firing Codes for Time in Rodent Medial Prefrontal Cortex. *Cerebral Cortex (New York, NY)*, *27*(12), 5663–5671. https://doi.org/10.1093/cercor/bhw336

Tremblay, R., Lee, S., & Rudy, B. (2016). GABAergic Interneurons in the Neocortex: From Cellular Properties to Circuits. *Neuron*, *91*(2), 260–292. https://doi.org/10.1016/j.neuron.2016.06.033

Tsai, P. T., Hull, C., Chu, Y., Greene-Colozzi, E., Sadowski, A. R., Leech, J. M., Steinberg, J., Crawley, J. N., Regehr, W. G., & Sahin, M. (2012). Autistic-like behaviour and cerebellar dysfunction in Purkinje cell Tsc1 mutant mice. *Nature*, *488*(7413), 647–651. https://doi.org/10.1038/nature11310

Tsutsumi, S., Chadney, O., Yiu, T.-L., Bäumler, E., Faraggiana, L., Beau, M., & Häusser, M. (2020). Purkinje Cell Activity Determines the Timing of Sensory-Evoked Motor Initiation. *Cell Reports*, *33*(12), 108537. https://doi.org/10.1016/j.celrep.2020.108537

Turi, G. F., Li, W.-K., Chavlis, S., Pandi, I., O'Hare, J., Priestley, J. B., Grosmark, A. D., Liao, Z., Ladow, M., Zhang, J. F., Zemelman, B. V., Poirazi, P., & Losonczy, A. (2019). Vasoactive Intestinal Polypeptide-Expressing Interneurons in the Hippocampus Support Goal-Oriented Spatial Learning. *Neuron*, *101*(6), 1150-1165.e8. https://doi.org/10.1016/j.neuron.2019.01.009

Valera, A. M., Binda, F., Pawlowski, S. A., Dupont, J.-L., Casella, J.-F., Rothstein, J. D., Poulain, B., & Isope, P. (2016). Stereotyped spatial patterns of functional synaptic connectivity in the cerebellar cortex. *ELife*, *5*, e09862. https://doi.org/10.7554/eLife.09862

Van Beugen, B. J., Gao, Z., Boele, H.-J., Hoebeek, F., & De Zeeuw, C. I. (2013). High Frequency Burst Firing of Granule Cells Ensures Transmission at the Parallel Fibre to Purkinje Cell Synapse at the Cost of Temporal Coding. *Frontiers in Neural Circuits*, *7*. https://doi.org/10.3389/fncir.2013.00095

Van Essen, D. C., Donahue, C. J., & Glasser, M. F. (2018). Development and Evolution of Cerebral and Cerebellar Cortex. *Brain, Behavior and Evolution*, *91*(3), 158–169. https://doi.org/10.1159/000489943

van Welie, I., Roth, A., Ho, S. S. N., Komai, S., & Häusser, M. (2016). Conditional Spike Transmission Mediated by Electrical Coupling Ensures Millisecond Precision-Correlated Activity among Interneurons In Vivo. *Neuron*, *90*(4), 810–823. https://doi.org/10.1016/j.neuron.2016.04.013

Vervaeke, K., Lőrincz, A., Gleeson, P., Farinella, M., Nusser, Z., & Silver, R. A. (2010). Rapid Desynchronization of an Electrically Coupled Interneuron Network with Sparse Excitatory Synaptic Input. *Neuron*, *67*(3), 435–451. https://doi.org/10.1016/j.neuron.2010.06.028

Vervaeke, K., Lőrincz, A., Nusser, Z., & Silver, R. A. (2012). Gap Junctions Compensate for Sublinear Dendritic Integration in an Inhibitory Network. *Science*, *335*(6076), 1624–1628. https://doi.org/10.1126/science.1215101

Viet, N.-M., Wang, T., Tran-Anh, K., & Sugihara, I. (2022). Heterogeneity of intrinsic plasticity in cerebellar Purkinje cells linked with cortical molecular zones. *IScience*, *25*(1), 103705. https://doi.org/10.1016/j.isci.2021.103705

Voogd, J. (2011). Cerebellar Zones: A Personal History. *The Cerebellum*, *10*(3), 334–350. https://doi.org/10.1007/s12311-010-0221-6

Voogd, J., Gerrits, N. M., & Ruigrok, T. J. H. (1996). Organization of the Vestibulocerebellum. *Annals of the New York Academy of Sciences*, *781*(1 Lipids and Sy), 553–579. https://doi.org/10.1111/j.1749-6632.1996.tb15728.x

Voogd, J., & Ruigrok, T. J. H. (2004). The organization of the corticonuclear and olivocerebellar climbing fibre projections to the rat cerebellar vermis: The congruence of projection zones and the zebrin pattern. *Journal of Neurocytology*, *33*(1), 5–21. https://doi.org/10.1023/B:NEUR.0000029645.72074.2b

Wadiche, J. I., & Jahr, C. E. (2005). Patterned expression of Purkinje cell glutamate transporters controls synaptic plasticity. *Nature Neuroscience*, *8*(10), 1329–1334. https://doi.org/10.1038/nn1539

Wagner, M. J., Kim, T. H., Kadmon, J., Nguyen, N. D., Ganguli, S., Schnitzer, M. J., & Luo, L. (2019). Shared Cortex-Cerebellum Dynamics in the Execution and Learning of a Motor Task. *Cell*, *177*(3), 669-682.e24. https://doi.org/10.1016/j.cell.2019.02.019

Walter And, J. T., & Khodakhah, K. (2009). The advantages of linear information processing for cerebellar computation. *Proceedings of the National Academy of Sciences*, *106*(11), 4471–4476. https://doi.org/10.1073/pnas.0812348106

Wang, S. S.-H., Ambrosini, A. E., & Wittenberg, G. M. (2016). Evolution and scaling of dendrites. In G. Stuart, N. Spruston, & M. Häusser (Eds.), *Dendrites* (p. 0). Oxford University Press. https://doi.org/10.1093/acprof:oso/9780198745273.003.0002

Wang, W. X., & Lefebvre, J. L. (2022). Morphological pseudotime ordering and fate mapping reveal diversification of cerebellar inhibitory interneurons. *Nature Communications*, *13*(1), 3433. https://doi.org/10.1038/s41467-022-30977-2

Watt, A. J., Cuntz, H., Mori, M., Nusser, Z., Sjöström, P. J., & Häusser, M. (2009). Traveling waves in developing cerebellar cortex mediated by asymmetrical Purkinje cell connectivity. *Nature Neuroscience*, *12*(4), 463–473. https://doi.org/10.1038/nn.2285

Wellershaus, K., Degen, J., Deuchars, J., Theis, M., Charollais, A., Caille, D., Gauthier, B., Janssen-Bienhold, U., Sonntag, S., Herrera, P., Meda, P., & Willecke, K. (2008). A new conditional mouse mutant reveals specific expression and functions of connexin36 in neurons and pancreatic beta-cells. *Experimental Cell Research*, *314*(5), 997–1012. https://doi.org/10.1016/j.yexcr.2007.12.024

Wilms, C. D., & Häusser, M. (2015). Reading out a spatiotemporal population code by imaging neighbouring parallel fibre axons in vivo. *Nature Communications*, *6*(1), 6464. https://doi.org/10.1038/ncomms7464

Wilson, M. A., & McDonald, A. J. (2020). The amygdalar opioid system. In *Handbook of Behavioral Neuroscience* (Vol. 26, pp. 161–212). Elsevier. https://doi.org/10.1016/B978-0-12-815134-1.00008-8

Wise, A. K., Cerminara, N. L., Marple-Horvat, D. E., & Apps, R. (2010). Mechanisms of synchronous activity in cerebellar Purkinje cells: Synchrony in the cerebellum. *The Journal of Physiology*, *588*(13), 2373–2390. https://doi.org/10.1113/jphysiol.2010.189704

Witter, L., Rudolph, S., Pressler, R. T., Lahlaf, S. I., & Regehr, W. G. (2016). Purkinje Cell Collaterals Enable Output Signals from the Cerebellar Cortex to Feed Back to Purkinje Cells and Interneurons. *Neuron*, *91*(2), 312–319. https://doi.org/10.1016/j.neuron.2016.05.037

Wolpert, D. M., Miall, R. C., & Kawato, M. (1998). Internal models in the cerebellum. *Trends in Cognitive Sciences*, *2*(9), 338–347. https://doi.org/10.1016/S1364-6613(98)01221-2

Woolston, D. C., Kassel, J., & Gibson, J. M. (1981). Trigeminocerebellar mossy fibre branching to granule cell layer patches in the rat cerebellum. *Brain Research*, *209*(2), 255–269. https://doi.org/10.1016/0006-8993(81)90152-9

Wu, B., Blot, F. G., Wong, A. B., Osório, C., Adolfs, Y., Pasterkamp, R. J., Hartmann, J., Becker, E. B., Boele, H.-J., De Zeeuw, C. I., & Schonewille, M. (2019). TRPC3 is a major contributor to functional heterogeneity of cerebellar Purkinje cells. *ELife*, *8*, e45590. https://doi.org/10.7554/eLife.45590

Xiao, J., Cerminara, N. L., Kotsurovskyy, Y., Aoki, H., Burroughs, A., Wise, A. K., Luo, Y., Marshall, S. P., Sugihara, I., Apps, R., & Lang, E. J. (2014). Systematic Regional Variations in Purkinje Cell Spiking Patterns. *PLoS ONE*, *9*(8), e105633. https://doi.org/10.1371/journal.pone.0105633

Xu, S., Yang, H., Menon, V., Lemire, A. L., Wang, L., Henry, F. E., Turaga, S. C., & Sternson, S. M. (2020). Behavioral state coding by molecularly defined paraventricular hypothalamic cell type ensembles. *Science*, *370*(6514), eabb2494. https://doi.org/10.1126/science.abb2494

Yaginuma, H., & Matsushita, M. (1989). Spinocerebellar projections from the upper lumbar segments in the cat, as studied by anterograde transport of wheat germ agglutinin-horseradish peroxidase. *The Journal of Comparative Neurology*, *281*(2), 298–319. https://doi.org/10.1002/cne.902810211

Yang, W., & Yuste, R. (2017). In vivo imaging of neural activity. *Nature Methods*, *14*(4), 349–359. https://doi.org/10.1038/nmeth.4230

Zang, Y., & De Schutter, E. (2021). The Cellular Electrophysiological Properties Underlying Multiplexed Coding in Purkinje Cells. *The Journal of Neuroscience*, *41*(9), 1850–1863. https://doi.org/10.1523/JNEUROSCI.1719-20.2020

Zeeuw, C. I., & Berrebi, A. S. (1995). Postsynaptic Targets of Purkinje Cell Terminals in the Cerebellar and Vestibular Nuclei of the Rat. *European Journal of Neuroscience*, *7*(11), 2322–2333. https://doi.org/10.1111/j.1460-9568.1995.tb00653.x

Zempolich, G. W., Brown, S. T., Holla, M., & Raman, I. M. (2021). Simple and complex spike responses of mouse cerebellar Purkinje neurons to regular trains and omissions of somatosensory stimuli. *Journal of Neurophysiology*, *126*(3), 763–776. https://doi.org/10.1152/jn.00170.2021

Zhang, J., Tran-Anh, K., Hirata, T., & Sugihara, I. (2021). Striped Distribution Pattern of Purkinje Cells of Different Birthdates in the Mouse Cerebellar Cortex Studied with the Neurog2-CreER Transgenic Line. *Neuroscience*, *462*, 122–140. https://doi.org/10.1016/j.neuroscience.2020.07.028

Zhang, W., & Linden, D. J. (2012). Calcium Influx Measured at Single Presynaptic Boutons of Cerebellar Granule Cell Ascending Axons and Parallel Fibres. *The Cerebellum*, *11*(1), 121–131. https://doi.org/10.1007/s12311-009-0151-3

Zhang, Y., Rózsa, M., Liang, Y., Bushey, D., Wei, Z., Zheng, J., Reep, D., Broussard, G. J., Tsang, A., Tsegaye, G., Narayan, S., Obara, C. J., Lim, J.-X., Patel, R., Zhang, R., Ahrens, M. B., Turner, G. C., Wang, S. S.-H., Korff, W. L., … Looger, L. L. (2023). Fast and sensitive GCaMP calcium indicators for imaging neural populations. *Nature*, *615*(7954), 884–891. https://doi.org/10.1038/s41586-023-05828-9

Zhou, H., Lin, Z., Voges, K., Ju, C., Gao, Z., Bosman, L. W., Ruigrok, T. J., Hoebeek, F. E., De Zeeuw, C. I., & Schonewille, M. (2014). Cerebellar modules operate at different frequencies. *ELife*, *3*, e02536. https://doi.org/10.7554/eLife.02536

Zong, H., Espinosa, J. S., Su, H. H., Muzumdar, M. D., & Luo, L. (2005). Mosaic Analysis with Double Markers in Mice. *Cell*, *121*(3), 479–492. https://doi.org/10.1016/j.cell.2005.02.012